Novel Detection Schemes for Transmission Electron Microscopy

Vernieuwende detectie methoden in Transmissie Elektronen Microscopie

Proefschrift voorgelegd tot het behalen van de graad van

DOCTOR IN DE WETENSCHAPPEN: FYSICA

aan de Universiteit Antwerpen, te verdedigen door

Daen Jannis

Promotor:

JO VERBEECK

Antwerpen, 2021

Chairman

Prof. Dr. Wim Wenseleer, University of Antwerp, Belgium

Supervisor

Prof. Dr. Jo Verbeeck, University of Antwerp, Belgium

Members

Prof. Dr. Bart Partoens, University of Antwerp, Belgium

Prof. Dr. Nick van Remortel, University of Antwerp, Belgium

Prof. Dr. Knut Müller-Caspary, Ludwig-Maximilians-Universität Munich, Germany

Prof. Dr. Jom Luiten, TU Eindhoven, Netherlands

Dr. Luiz Tizei, Université Paris Sud, France

Contact Information

Daen Jannis

University of Antwerp

Faculty of Science

Department of Physics

Groenenborgerlaan 171

2020 Antwerp

Belgium

daen.jannis@uantwerpen.be

Contents

Preface 1

Samenvatting 5

1. Electron Scattering and Detection 9

1.1. Electron Scattering 9

1.2. Particle Detection 18

2. How to perform electron scattering experiments: The Electron Microscope 31

2.1. 4D STEM 33

2.2. Electron Energy Loss Spectroscopy 44

2.3. Energy Dispersive X-ray Spectroscopy 51

3. 4D STEM-in-SEM 57

3.1. Introduction 58

3.2. Experimental Setup 59

3.3. Materials 61

3.4. Data Analysis 62

3.5. Results 73

3.6. Conclusion 91

4. 4D STEM in Event Driven Mode 93

4.1. Introduction 94

4.2. Experimental Setup 96
4.3. Detector Characterization 98
4.4. Results 104
4.5. Discussion 113
4.6. Conclusion 114

5. Event Driven Coincidence Detection in Transmission Electron Microscopy 115
5.1. Introduction 116
5.2. Experimental Setup 117
5.3. Theoretical Description 124
5.4. Results 128
5.5. Conclusions and Outlook 151

6. General Conclusions and Outlook 153

A. List of Abbreviations 157

B. Output 159
B.1. Publications 159
B.2. Conferences 161

Bibliography 163

List of Figures 187

List of Tables 205

Preface

Electron microscopy is an excellent tool which provides resolution down to the atomic scale with up to pm precision in locating atoms. The characterization of materials in these length scales is of utmost importance to answer questions in biology, chemistry and material science. The successful implementation of aberration-corrected microscopes made atomic resolution imaging relatively easy, this could give the impression that the development of novel electron microscopy techniques would stagnate and only the application of these instruments as giant magnifying tools would continue.

This is of course not true and a multitude of problems still exist in electron microscopy. Three of such issues are discussed below.

1. Transmission electron microscopy (TEM) has the potential to measure individual atoms. However, it has a limited field of view resulting that only one small part of the specimen (a couple of μm^2) can be investigated at a time. Furthermore, the operation of the TEM is quite complicated making it hard to develop an automatic robust characterization method. These disadvantages make this technique not suitable for micro structural analysis of mm-scale fields of view. The micro structure provides information about grain boundaries, defects, *etc.* where the large fields of view are necessary to provide enough statistics on these structures. Moreover, having a fast automated technique can improve the synthesis process of these materials. One example of this is for the 2D materials where the mechanical, chemical and electrical properties depend on its micro structure.

2. One of the biggest problems in electron microscopy is the presence of beam damage

which occurs due the fact that the highly energetic incoming electrons have sufficient kinetic energy to change the structure of the material. The amount of damage induced depends on the dose, hence minimizing this dose during an experiment is beneficial. This minimizing of the total dose comes at the expense of more noise due to the counting nature of the electrons.
For this reason, the implementation of four dimensional scanning transmission electron microscopy (4D STEM) experiments, where at every probe position the entire far field scattering is measured, has reduced the total dose needed per acquisition. However, the current cameras used to measure the diffraction patterns are still two orders of magnitude slower than to the conventional STEM methods. Improving the acquisition speed would make the 4D STEM technique more feasible and is of utmost importance for the beam sensitive materials since less dose is used during the acquisition.

3. In TEM there is not only the possibility to perform imaging experiments but also spectroscopic measurements. There are two frequently used methods: electron energy-loss spectroscopy (EELS) and energy dispersive x-ray spectroscopy (EDX). EELS measures the energy-loss spectrum of the incoming electron which gives information on the available excitations in the material providing elemental sensitivity. In EDX, the characteristic x-rays, arising from the decay of an atom which is initially excited due to the incoming electrons, are detected providing similar elemental analysis. Both methods are able to provide comparable elemental information where in certain circumstances one outperforms the other. However, both methods have a detection limit of approximately 100-1000 ppm which is not sufficient for some materials, especially when one wants to detect trace elements in a matrix.

In this thesis, three novel techniques were developed which can make significant progress for the three problems discussed above.

Chapter 1: Electron Scattering and Detection

The first chapter overviews the relevant scattering processes which occur when a highly energetic electron interacts with a thin specimen. By measuring these different types of scattering, structural information about the specimen can be gathered. Moreover, the detection of the emitted particles present during scattering is discussed. In this work, the focus is on the detection of the outgoing electron and x-rays emitted by the specimen.

Chapter 2: How to perform electron scattering experiments: Electron Microscope
The second chapter introduces the experimental methods used in conventional electron microscopy with the emphasis on 4D STEM, EELS and EDX. The limitations of these methods are discussed, resulting in the motivation for the research in this thesis.

Chapter 3: 4D STEM in SEM
The third chapter describes an excellent characterization technique for 2D materials by using the 4D STEM technique inside a scanning electron microscope (SEM). The novel technique is able to perform fast, reliable, mm-scale structural characterization with μm-resolution.

Chapter 4: 4D STEM in Event Driven Mode
The fourth chapter explores the possibility to use an event driven detector where the point of impact and time of arrival for each individual event is stored making this the ideal type of detector to perform 4D STEM experiments at higher speeds. This opens up the possibility to do fast multi-frame 4D STEM experiments at low dose conditions.

Chapter 5: Event Driven Coincidence Detection in Transmission Electron Microscopy
The fifth chapter combines the time correlation between the inelastic electrons scattering and characteristic x-rays emission in order to increase the selectivity of spectroscopic analysis opening up the possibility to perform trace element analysis in the TEM. Furthermore, the experimental setup is discussed and other advantages such as background-free EELS are discussed.

Chapter 6: General Conclusion and Outlook

The sixth chapter provides a general conclusion about this theses and takes a look into future improvements and applicability's of the developed methodologies.

Samenvatting

Elektronenmicroscopie is een uitstekende techniek met een resolutie tot op atomaire schaal waarvan de atoom posities bepaald kunnen worden met picometer precisie. Het karakteriseren van materialen op deze lengteschalen is zeer belangrijk in de onderzoeksvelden van biologie, chemie en materiaalkunde. Het succesvol implementeren van de aberratie gecorrigeerde elektronenmicroscopen heeft ervoor gezorgd dat het relatief makkelijk is om atomaire resolutie te bekomen. Men zou dus de impressie kunnen krijgen dat de ontwikkeling van betere elektronenmicroscopie technieken zou stagneren en dat dit alleen nog maar wordt toegepast als een gigantisch vergrootglas.

Dit is natuurlijk niet het geval want er bestaan nog een veelheid aan problemen in elektronenmicroscopie waar drie van deze problemen hieronder beschreven worden

1. Transmissie elektronenmicroscopie (TEM) heeft de mogelijkheid om relatief makkelijk indivduele atomen te detecteren. Deze techniek heeft echter een gelimiteerde gezichtsveld dat ervoor zorgt dat enkel een klein oppervlak van het materiaal onderzocht kan worden. Het bedienen van de TEM is bovendien gecompliceerd wat ervoor zorgt dat het moeilijk is om een automatisch robuste karakterisatie methode te ontwikkelen. Deze nadelen zorgen ervoor dat deze techniek niet geschikt is voor de karakterisatie van de micro structuur met millimeter schaal gezichtsveld. De micro structuur bevat informatie over de korrelgrenzen, defecten, etc., waar deze grootte van gezichtsveld noodzakelijk is om genoeg statistieken te vergaren. Voorts, zou deze karaterisatie techniek ook automatisch en snel moeten zijn zodat metingen tijdens het synthesatie proces uitgevoerd kunnen

worden. Een voorbeeld hiervan zijn de 2D materialen waarvan kennis over de micro structure noodzakelijk is om de mechanische, elektrische en chemische eigenschappen van deze materialen te begrijpen.

2. Een van de grootste problemen in elektronenmicroscopie is de aanwezigheid van stralingsschade omwille van de hoog energetische elektronen die genoeg kinetische energie hebben om de structuur van het materiaal te veranderen. De hoeveelheid geïnduceerde schade hangt af van de totale dosis dus het minimaliseren van deze dosis is voordelig. Deze minimalisatie veroorzaakt meer ruis omwille van het telproces van de elektronen. Hierdoor is er een nieuwe ruis robuuste techniek ontstaan die vier dimensionale raster transmissie elektronenmicroscopie (4D STEM) noemt. Hierin wordt op elke straal positie het volledige diffractie patroon gemeten waardoor er minder elektronen nodig zijn om een beeld met voldoende signaal tot ruis verhouding te construeren. De detectoren die hiervoor worden gebruikt zijn op dit moment twee orders in magnitude trager dan de conventionele STEM methodes. Het verbeteren van deze snelheid zou ervoor zorgen dat 4D STEM meer toegankelijker wordt en dat is zeer belangrijk voor het karakteriseren van stralings gevoelige materialen op atomaire schaal waarvan de totale dosis geminimaliseerd moet worden.

3. Naast beeldvorming bestaan er ook spectroscopische technieken in TEM. Twee frequent gebruikte methodes zijn elektronen energie verlies spectroscopie (EELS) en energie dispersieve x-stralen spectroscopie (EDX). EELS meet het energie verlies spectrum van de inkomende elektronen, dit geeft informatie over de beschikbare excitaties in het materiaal wat toegang geeft tot elementaire kennis. In EDX worden karakteristieke x-stralen, gecreëerd door het vervallen van de gëexciteerde atomen die initieel geëxciteerd worden door het inkomend elektron, gemeten waardoor er gelijkaardige elementaire informatie verkregen wordt. Beide methodes zijn in staat om elementaire informatie te verkrijgen waar in sommige omstandigheden het ene meer geschikt is dan het andere. De detectie limiet van beide methodes is 100-1000 ppm wat niet voldoende is om sporenelementen

in een matrix te detecteren.

In deze thesis werden drie vernieuwde technieken ontwikkeld die voor significante voortgang zorgden voor de drie problemen die hierboven beschreven zijn.

Hoofdstuk 1: Elektronen verstrooiing en detectie
Het eerste hoofdstuk geeft een overzicht van de relevante verstrooiings processen die voorkomen als een hoog energetisch elektron interageert met een dun materiaal. Door deze verschillende soorten verstrooiing te meten kan men structurele informatie vergaren over het materiaal. Verder is de detectie van de deeltjes die uitgezonden worden tijdens de interactie beschreven. Deze deeltjes zijn de uitgaande elektronen en x-stralen uitgestuurd door het materiaal.

Hoofdstuk 2: Hoe doen we elektronen verstrooiings experimenten: elektronenmicroscoop
Het tweede hoofdstuk introduceerd de conventionele experimentele elektronenmicroscopie methodes waar de nadruk wordt gelegd op 4D STEM, EELS en EDX. De limitaties van de methodes worden besproken waardoor de motivatie van het onderzoek in deze thesis naar voren komt.

Hoofdstuk 3: 4D STEM in SEM
Het derde hoofdstuk beschrijft een excellente karaterisatie techniek voor 2D materialen door gebruik te maken van de 4D STEM methode in een raster elektronenmicroscoop (SEM). Deze nieuwe techniek kan deze materialen snel, robust en op milimeter schaal structureel karakteriseren met micrometer resolutie.

Hoofdstuk 4: 4D STEM in event modus
Het vierde hoofdstuk onderzoek de mogelijkheid om een event gedreven detector, die het inslagpunt en aankomst tijd for elk event opslaat, te gebruiken voor 4D STEM experimenten. Deze detector zorgt ervoor dat de 4D STEM experimenten op veel hogere snelheden uitgevoerd kan

worden. Dit geeft de mogelijkheid tot snelle experimenten met lage doses.

Hoofdstuk 5: Event gedreven coincidentie detectie in transmissie elektronenmicroscopie
Het vijfde hoofdstuk combineert de tijdscorrelatie tussen het inelastisch electron en de karakteristieke x-stralen waardoor de selectiviteit van de spectroscopische analyse verbeterd wordt. Dit geeft de mogelijkheid om sporenelementen te meten in de TEM. Verder wordt de experimentele opstelling en voordelen van de methodes, zoals achtergrond vrije EELS, besproken.

Hoofdstuk 6: Algemene conclusie en vooruitzichen
Het zesde hoofdstuk voorziet een algemene conclusie over deze thesis en geeft een blik op toekomstige verbeteringen en de toepassingen van de ontwikkelde methodes.

1. Electron Scattering and Detection

1.1. Electron Scattering

The scattering of high energetic free electrons (5-300 keV) with materials is often divided into two categories. The elastic and inelastic scattering where for the elastic interaction, the kinetic energy of the incoming electron is conserved but its direction of propagation is altered. Contrarily for inelastic scattering, the kinetic energy of the incoming electron is modified. This implies that some energy has been exchanged with the specimen. In this section an overview of these types of electron scattering is given as a basis for the original work in the later chapters. In the last subsection, the emission process of x-rays from the interaction between fast electrons and specimen is described.

1.1.1. Elastic Scattering: Electron Diffraction

Diffraction is a wave phenomenon which describes the interference between the incoming wave and an object. The far field interference pattern gives spatial information on the incoming wave and the object. The most well known experiment showing the "effect" of diffraction is the double-slit experiment where a parallel wave propagates through two infinitely small slits which are a certain distance apart from each other. At the far field, a sinusoidal intensity pattern arises where, if the wavelength and geometry of the setup is known, it is possible to retrieve the distance between the two slits. Hence giving information on the structure of an object. Note that the object under investigation is a binary object, transparent or not, where the amplitude is transmitted inside the slits. Usually the material under investigation is far more complicated

since the interaction is determined by the properties of the incoming particle and material itself.

In general, diffraction experiments are possible with all particles which are described with a wave function such as photons, neutrons and electrons. These particles will each interact in a distinctive manner since they exert other forces to matter. For instance, the neutron does not have a electrostatic charge hence, it will not interact with the electrostatic potential of matter but with the nucleus via the nuclear force. Since the neutron has a non-zero magnetic moment, it can also interact with magnetic fields. On the other hand, electrons have a charge hence the interaction with matter is mainly via the electrostatic force. However, since the electrons are travelling at a certain velocity, they are susceptible to the magnetic field due to the Lorentz force.

The specimens which are commonly investigated in an electron microscope are usually more complicated than the two slit setup but in essence the concept stays the same and if the interaction potential is fully known then the scattered wave can be relatively easily modelled. The interaction potential between specimen and an incoming electron is mainly determined by the electric and magnetic potentials of the specimen. The phase shift ($\Delta\phi$) imparted on the electron wave with wavelength λ and energy E is given by [1]:

$$\Delta\phi(x, y) = \frac{\pi}{\lambda E} \int_{-\infty}^{\infty} V(x, y, z) dz - \frac{e}{\hbar} \int_{-\infty}^{\infty} A_z(x, y, z) dz \tag{1.1}$$

where $\hbar$ is the reduced Planck constant, e is the electron charge, V is the electrostatic potential and A_z is the z component of the magnetic vector potential. Hence if the entire atomic configuration of the material is known, the phase shift can be accurately determined. In a practical electron microscopy experiment we are faced with the inverse problem of finding the potential from the results of the scattering process which is far less obvious. The knowledge of the potential (very often the magnetic potential is assumed zero but in some cases this is exactly the information we are after) reveals information about the (projected) atomic structure of the material.

Next to the material, the preparation of the incoming electron wave function (ψ_{in}) is important in the description of the electron scattering. In the electron microscope, the incoming wave

($\psi_{in}(\vec{r})$) is commonly described as following[1]:

$$\psi_{in}(\vec{r}) = \mathcal{F}^{-1}\left\{A(\vec{k}) \cdot e^{i\chi(\vec{k})}\right\}(\vec{r}) \tag{1.2}$$

where $\vec{r} = (x, y)$, $A(\vec{k})$ is the aperture function and $\chi(\vec{k})$ is the aberration function. The aperture function defines the angular distribution of the probing beam. For instance $A(\vec{k}) = \delta(\vec{k})$ describes a parallel electron beam. In general, when using a condensed probe, the aperture function is defined as following:

$$A(\vec{k}) = \begin{cases} 1 & \text{where} \quad |\vec{k}| \leq k_{max} \\ 0 & \text{where} \quad |\vec{k}| > k_{max} \end{cases} \tag{1.3}$$

where k_{max} is maximum angle used in the aperture.

The aberration function describes the deviation of the optical elements compared to the ideal lens. Modern electron microscopes are equipped with aberration corrector lenses which are used to minimize the aberrations of the system. As seen from Eq. 1.2, the aberration function χ adds a phase modulation to the aperture function where the smallest probe is obtained when the phase is flat. A simplified model of the aberration function (up to 3th order and only radially symmetric terms) is given as follows:

$$\chi(\vec{k}) = \pi C_1 \lambda |\vec{k}|^2 + \frac{\pi}{2} C_3 \lambda^3 |\vec{k}|^4 \tag{1.4}$$

where C_1 and C_3 are respectively the defocus and spherical aberration constant where C_3 depends on the lenses used in the microscope. From Eq. 1.4 it is seen that C_3 becomes dominant at high angles. Therefore it is not possible to reduce the spatial extent of the electron probe indefinitely by increasing the convergence angle without an aberration corrector. Note that at higher angles even higher order aberrations will start to become dominant.

Now we have the two ingredients, the object and the incoming electron wave, to describe the elastic scattering where the incoming wave function is connected to the outgoing (ψ_{out})

[1]The inverse Fourier transform is defined as $\mathcal{F}^{-1}\{f(\vec{k})\}(\vec{r}) = \iint_{-\infty}^{\infty} f(\vec{k}) e^{2\pi i \vec{k}\cdot\vec{r}} d^2\vec{k}$

due to the interaction with the specimen [2]:

$$\psi_{out}(\vec{r}) = \psi_{in}(\vec{r}) \cdot e^{-i\Delta\phi(\vec{r})} \tag{1.5}$$

From Eq. 1.1 it is seen that the phase shift induced depends on the integrated potential over the z-direction which is the propagation direction of the electrons. Hence this reduces the three dimensional potential into a two dimensional projection which, in reality, is not true since the extent of the third dimension has significant influence on the outgoing wave function. For this reason, Eq. 1.5 is named as the phase object approximation (POA) [3] which holds for thin weakly scattering objects such as graphene.
Inside the electron microscope, ψ_{out} can be measured in imaging mode where an objective lens is used to project the wave in the image plane onto a detector which is what is mainly referred to as transmission electron microscopy (TEM). The other frequently used method measures ψ_{out} in the far field by placing a detector in this region where the measured intensity is known as the diffraction pattern. The outgoing wave in the far field ($\Psi_{out}(\vec{k})$) is described by using the Fourier transform [4][2]:

$$\Psi_{out}(\vec{k}) = \mathcal{F}\left\{\psi_{in}(\vec{r}) \cdot e^{i\Delta\phi(\vec{r})}\right\}(\vec{k}) \tag{1.6}$$

When performing experiments, the wave function is never measured directly but instead its probability density, defined as the square modulus of the wave function, gets detected. Hence, the amplitude is measured whereas the phase of the wave is not detected, which is known as the "phase problem" [5], complicating the information one can obtain from a single measurement. For instance, when measuring ψ_{out} (real space) no contrast is seen since the specimen only adds a phase and no amplitude is changed when there are no aberration introduced via the post-specimen lenses. For this reason, multiple methods have been developed to measure the phase of the outgoing wave such as holography and through focal reconstructions [6–8].

In the previous description, the specimen was approximated using the POA by neglecting the thickness of the specimen. This is not valid for most specimens and therefore the thickness

[2] The Fourier transform is defined as $\mathcal{F}\{f(\vec{r})\}(\vec{k}) = \iint_{-\infty}^{\infty} f(\vec{r})e^{-2\pi i\vec{k}\cdot\vec{r}}d^2\vec{r}$

should be taken into account which is commonly referred to as dynamical scattering. The name arises from the fact that when the electron beam propagates through the specimen, it can interact multiple times with the specimen. One frequently used method to describe this phenomena is the multislice algorithm which slices the three dimensional potential into multiple two dimensional phase objects where in between the modified electron wave is propagated using the Fresnel propagator [9, 10].

1.1.2. Inelastic Electron Scattering

Inelastic scattering occurs when the kinetic energy and momentum of the incoming electron is not conserved after the interaction. There exist multiple inelastic scattering mechanisms which are mainly distinguished by the energy exchange of the interaction.

1. Phonon excitations where the energy losses of the incoming electrons are in the order of 20 meV-1 eV which for photons corresponds to the infrared part of the electromagnetic spectrum. Only recently with the improvement on the monochromation of the electron source, has it been possible to detect these phonon modes in by spectroscopy based on inelastic scattering [11, 12].

2. Plasmons which are collective oscillations of the valence and conduction electrons they are situated in the low-loss regime of a typical EEL spectrum (5-30 eV) [13].

3. Single-electron excitations of the outer-shell electrons which can subdivided into the inter- and intraband transitions. They occur in the energy range from 2-20 eV [14].

4. Inner-shell ionization occurs when the incoming electron ionizes the atom by removing a core electron from an inner shell. The energy losses of the incoming electron is situated in the high energy loss which ranges from 50-3000 eV.

In this work, the type of inelastic scattering of interest is the inner-shell ionization and this will be further discussed in this section.

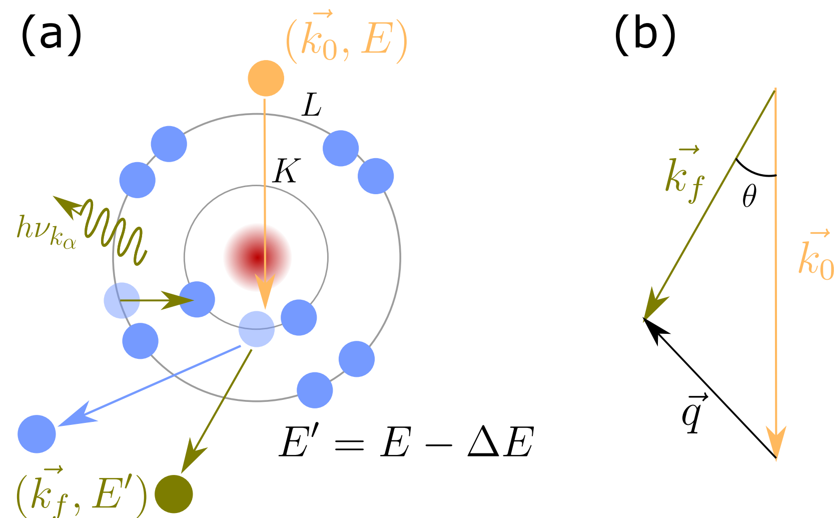

Figure 1.1.: **(a)** A schematic overview of the inner-shell ionization where the incoming electron loses energy due to the ionization of the atom. After the atom is excited, it can decay via the emission of a characteristic x-ray where the emission of the K_α x-ray is indicated. **(b)** The scattering geometry of the inelastic electron scattering where the different vectors are indicated.

Inner-shell Ionization

The ionization of core electrons occurs for bound electrons in the inner atomic shells such as the K, L, M, *etc.* shell. Electrons from these shells are excited to unoccupied energy states above the Fermi level. This defines that the minimal energy transfer for such a scattering to occur is larger than the binding energy of the shell. During the interaction of a single-electron excitation, such as the inner-shell ionization, energy from the incoming electron is transferred to an electron in the atom which is excited from its ground state to an excited state (see Fig. 1.1(a)). Hence before the interaction, the entire wave function is described by the state of the incoming electron and

ground state of the atom ($|\vec{k}_0, 0\rangle$). After the interaction, the wave function is represented by the outgoing electron wave and excited state of the atom ($|\vec{k}_f, n\rangle$) where the selection rules dictate the allowed transitions. For a fast non-relativistic incoming particle, the differential cross section $\frac{d\sigma}{d\Omega}$ is calculated using the lowest order interaction in the potential V described by the first Born approximation [15]:

$$\frac{d\sigma_{0,n}}{d\Omega} = \frac{m^2}{4\pi^2 h^4} \frac{|\vec{k}_f|}{|\vec{k}_0|} |\langle \vec{k}_0, 0|V|\vec{k}_f, n\rangle|^2 \tag{1.7}$$

where m is the reduced mass of the colliding system. The potential V is described by the Coulomb interaction between the atom and the incoming electron which is:

$$V(r) = \frac{Ze^2}{4\pi\epsilon_0|\vec{r}|} - \frac{1}{4\pi\epsilon_0} \sum_{j=1}^{Z} \frac{e^2}{|\vec{r} - \vec{r}_j|} \tag{1.8}$$

The first term corresponds to the potential created by the nucleus with charge Z and the second term is the potential due to the bound electrons. By inserting Eq. 1.8 into Eq 1.7, and rewriting the equation, where it is approximated that the scattering angle is small, the following result is obtained where the differential cross section is given per unit energy loss since we normally measure the energy-loss spectrum [16]:

$$\frac{d\sigma_{0,n}}{d\Omega d\Delta E} = \frac{e^4}{(4\pi\epsilon_0)^2 E\Delta E} \frac{1}{\theta^2 + \theta_E^2} \frac{df_{0,n}(\vec{q}, \Delta E)}{d\Delta E} \tag{1.9}$$

where E is the energy of the incoming electron, ΔE is the energy difference between $|0\rangle$ and $|n\rangle$, θ is the angle between $\vec{k}_0$ and $\vec{k}$, $\vec{q}$ is the momentum transfer vector and $\theta_E = E/(\gamma m_e v^2)$ is the characteristic scattering angle. In Fig. 1.1(b), a schematic overview of the scattering geometry is shown where the defined vectors are indicated. Finally, $df_{0,n}/d\Delta E$ is known as the generalized oscillator strength (GOS) which is related to the optical oscillator strength describing absorption of photons by an atom.

From Eq 1.9 one can observe that,without dynamical scattering, the scattering angles (θ) for inelastic scattering is mainly concentrated around the central beam resulting that an angle

selecting aperture around the central beam would not remove a lot of inelastic scattered electrons. The full derivation to obtain Eq 1.9 can be found in the work of Reimer and Kohl [17]. Note that the formulas describing the cross sections do not take the relativistic effects into account, however at high acceleration voltages (>200 kV) these effects start to become visible hence they should be taken into account in the description which can be found in Reimer and Kohl [17].

To obtain the cross section of the inelastic scattering, the GOS should be calculated beforehand which is a fundamental property of the atom. Multiple methods have been developed which determine the initial and final wave function of the atom by solving the Schrödinger/Dirac equation [16, 18]. These calculations are complicated and approximate the atom as free hence the interaction with other neighbouring atom, which results in modifications of the wave functions, is typically not taken into account. This makes it difficult to do absolute quantification of elements using the inelastic scattering of the electrons.

1.1.3. X-ray Emission

One of the most frequently employed methods for measuring the chemical content with an electron microscope is via the measurement of an x-ray energy spectrum which is generated during the interaction of a fast electron with a specimen. Mainly two types of x-ray radiation are emitted via the interaction of the electron with the specimen.

- Bremsstrahlung radiation
- Characteristic x-rays

One of these processes is Bremsstrahlung radiation which occurs when the incoming electron is decelerated and deflected through the interaction of the electron with the positive nucleus. During this scattering process, the energy lost by the incoming electron is converted into electromagnetic radiation. The energy of the emitted x-ray is a continuous spectrum from which the maximum energy of the x-ray is determined by the energy of the incoming electron.

A simple expression for the energy spectrum (E) of Bremsstrahlung (B_r) is given by [19]:

$$B_r(E) = \frac{KZ(E_0 - E)}{E} \tag{1.10}$$

where Z is the atomic number of the nucleus, E_0 is the kinetic energy of the incoming electron and K is Kramers constant. These Bremsstrahlung x-rays are not isotropically emitted but has its largest intensity in the direction of the incoming beam. This anisotropy in emission angle could be used in the TEM to change the ratio of detected characteristic and Bremsstrahlung x-rays.

The other x-ray emission process arises from characteristic x-rays which occur when the incoming electron scatters inelastically on an atom with an inner-shell interaction. The atom will be in an unstable excited state, hence it will decay to a stable state. In Fig. 1.1(a), a sketch of the characteristic x-ray emission is shown. The various x-ray transitions, when the atom decays via the emission of an x-ray, are named according to the initial vacancy. The other part of the name depends on the shell from which the electron originates. For instance, if a K-shell electron is removed during the interaction and the electron comes from the L-shell, the name of the emitted x-ray is the K_α x-ray. Similar when the electron comes from the M-shell, it is named the K_β x-ray. There are two competing processes which determine the decay, the production of an Auger electron or the emission of an x-ray. The probability to decay with x-ray emission is known as the fluorescence yield (ω) and depends on the atomic number and inner shell involved in the transition. In general, the fluorescence yield of a particular shell increases with atomic number. For instance the fluorescence yield for the C K_α line is 0.14% where for the Ag K_α line this value is 82 %. Furthermore, for one element, the fluorescence yield also increases with binding energy of the inner-shell hence the fluorescence yield for the K shell is larger than for the L shell for the same element. These characteristic x-rays have a very precise and predictable energy for each element making them commonly used for spectroscopic measurements.

1.2. Particle Detection

As seen in *Section 1.1*, after the interaction of the incoming electron with the specimen, two types of particles, electrons and photons, can propagate through free space making them suitable for detection. The measurement of these outgoing particles gives us information on the specimen since the structural, chemical and electronic properties of the specimen influence the scattering with the incoming electron. For the scattered incoming electrons, the main aim is to measure the spatial extent of its wave function which due to optical elements can be projected into different spaces. For instance, the probability density of the outgoing wave function can be measured in real space, due to the use of a lens, or in momentum space which is known as the far field. The far-field measurement is achieved via the propagation of the electron in free space and placing the detector sufficiently far away from the interaction. However in TEM, projector lenses are used to (de)magnify the diffraction pattern which is similar to changing the free space propagation length. Another projection is performed in electron energy-loss spectroscopy (EELS) where a magnetic prism is used to disperse the electron beam giving the ability to spatially measure the energy distribution of the electron. For x-rays, which are created from a secondary process, the energy is commonly measured. For this reason, detectors with optimized energy resolution and collection efficiency have been developed. In this chapter, several methods to detect these types particles are discussed.

1.2.1. Electron Detection

The reason for using an electron microscope is to gather information of a material at the nano scale. This uses the incoming electron to interact with the specimen where the measurement of the outgoing electron gives information about the investigated material due to the interaction between the incoming electron and specimen. Hence if the entire wave function of the outgoing electron would be known, maximal information on the material would be obtained. However the Copenhagen interpretation in quantum mechanics states that the wave function collapses to a single state making it impossible to measure the entire wave function from a single electron.

In order to maximize the knowledge on the outgoing electron wave function, many electrons which interact with the material in the same manner are needed. This is the conventional method in electron microscopy where millions of electrons are used to detect the probability density distribution. However due to instabilities in the microscope, and especially beam damage, this is not always possible. Hence, the need for the best electron detection is necessary to make every electron count.

The ideal detector is able to detect the point of impact with the best accuracy and does not add any noise to the signal. The inaccuracy on the point of impact is described by the point spread function (PSF) which specifies how a point source, for instance an electron, spreads resulting in a less precise point of impact. For example, when the incoming electron interacts with a pixelated detector, there is a finite accuracy to which the electron position can be determined which is the pixel size. Hence, for pixelated detectors there will always be a theoretical best PSF which is determined by the pixel size. Furthermore, many detectors add noise to the signal such as thermal agitations which add unwanted noise to the signal. To take these different imperfections of the detector into account, a measure of quality is used. This is known as the detector quantum efficiency (DQE) which is given by:

$$DQE = \frac{SNR_{out}^2}{SNR_{in}^2} \leq 1 \tag{1.11}$$

where SNR is the signal-to-noise of the output and input signal. The DQE of real detectors is always less than unity and the aim is to develop a detector which best approximates the ideal detector (DQE=1).

Indirect Electron Detection

One commonly used method for the detection of high energy electrons is via the conversion of these electrons to lower energy particles. These are mainly photons which are created via the interaction of the electrons with a scintillator which is what happens for charge-coupled devices (CCD). Another method uses secondary low energy electrons where the high energy

electron generates an electron cloud which gets detected, this principle is used for delay line detectors (DLD).

Charge-Coupled Device Cameras: The CCD camera is a pixelated detector which provides the ability to live capture and process the images [20]. A scintillator is placed on top of the CCD to convert the incoming electron into photons. The conversion from electron to photons is essential since defects are created inside the CCD pixels when illuminated by the electrons directly which would lead to a decrease in sensitivity over time. Moreover, without a scintillator, the number of created electron-hole pairs rapidly exceeds the limit per pixel which corresponds to only 100 e^- per pixel [17], hence the dynamic range of the detector will be poor. The PSF of the detector depends heavily on the scintillator where for thicker layers, the PSF increases but the number of created photons will increase for thicker scintillators hence a proper choice should be made based on the trade-offs outlined [21].

After the conversion to photons, these particles will interact with the silicon pixel via the creation of electron-hole pairs. Additionally, other processes can occur which do not result in the creation of an electron-hole pair, such as reflections, which decreases the performance of the detector. After the free charge carriers are created, they are collected in every pixel during a period of integration making that the readout intensity of the pixel depends on the deposited energy in it. These charges can be transferred in a stepwise fashion to a readout register where the charge get amplified and digitized. This process is performed until all pixels have been read out. Due to the serial readout, it is hard to make these types of detectors very fast while keeping the large number of pixels.

Although the CCD is the main camera used in TEM, it has some disadvantages such as the occurrence of blooming which creates streaks when the saturation level in one pixel is exceeded and it spills to adjacent pixels. Moreover, since the energy of the incoming photons is relatively low, it is hard to distinguish between them and the thermal agitations hence dark noise will be present in these detectors. This noise is typically reduced by cooling the detector however it cannot be totally removed. Also one has to be careful operating these detectors since they

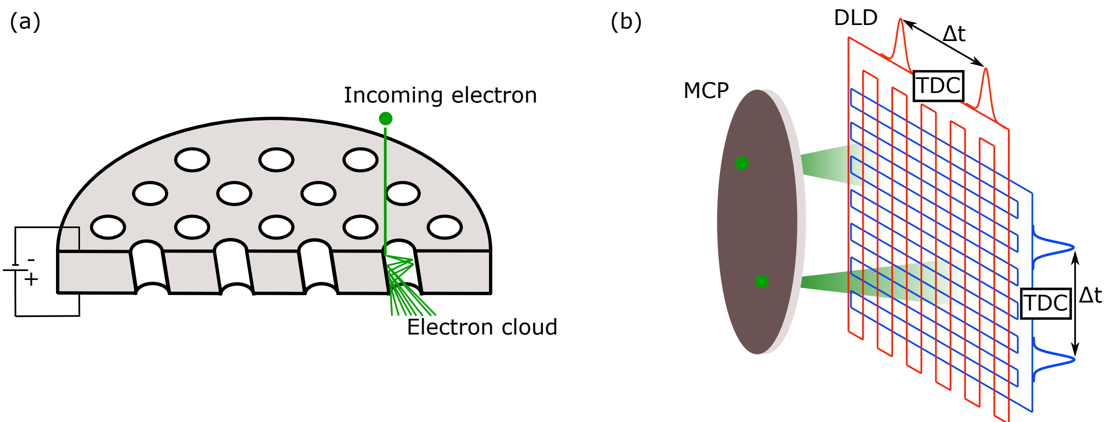

Figure 1.2.: **(a)** Schematic sketch of the MCP where the incoming electron creates an electron cloud via the interaction with the MCP. **(b)** The delay line where due where the incoming electron clouds induces an electrical pulse from which the time difference between the two pulses give information on the point of impact.

are susceptible to radiation damage which is why they typically use a beam stopper to block the central beam in electron diffraction experiments. Finally, due to the serial readout of pixels, the speed of these pixelated detectors is relatively low being around 45 frames per second (fps). This is very slow if one wants to perform experiments at μs timescales which is important for 4D STEM experiments. However for typical TEM experiments, where the exposure time is in the order of seconds, the slow frame rate is no issue.
In the last decade CCD cameras without any scintillator have been developed which is named the pn-CCD [22]. This detector has a limited amount of pixels (264×264), is radiation hard, has a high frame rate and provides a high dynamic range, making this type of detector well suited for 4D STEM experiments [23].

Delay Line Detector: The DLD is a pixel-free detector which measures the position (x, y) and time-of-arrival (TOA) of the incoming electron [24]. This is inherently different than a

pixelated frame-based camera where the signal in each pixel is integrated for a certain amount of time. These types of detector are not very common in TEM but they are frequently used in the field of time-of-flight photoemission electron microscopy [25], atomic probe tomography [26] and coulomb explosion experiments [27].

The DLD consists of two lines and a microchannel plate (MCP) on top. The MCP is a mm thick plate which is made out of an electrically insulating material with small hexagonal holes in the plate [28]. The holes are not perpendicular with the surface but have a small inclination angle. An electrical potential in the order of 1 kV is applied to create an electric field in the direction of the holes. When a particle enters the hole and interacts with the surface, multiple secondary electrons can be created. Due to the electric field, the free secondary electrons are again accelerated and can interact with the surface making the MCP an electron amplifier. So one electron comes into the MCP and at the end, an electron cloud is generated. The schematic sketch of the MCP is shown in Fig. 1.2(a). This cloud is accelerated by a small electric field towards the delay lines which consists out of two serpentine-shaped wire frames. The charge cloud induces an electrical pulse in the wires from which the point of impact can be determined by measuring the time between the pulses which will travel in both directions of the two wires, providing and x and y coordinate [25] (see Fig. 1.2(b)). The arrival times of the four signals is measured by time-to-digital convertors (TDC). The PSF of the DLD is mainly limited by the pore pitch size of the MCP. Besides the point of impact, the TOA of the electron can be determined by taking the average time of the two pulses.

This detector is able to record individual electron events with a temporal precision in the order of picoseconds which opens up possibilities to investigate temporal processes in the ps range. In *Chapter 5*, this detector is used to investigate the temporal correlation between inelastic electrons and characteristic x-rays. The disadvantage of this detector is that the quantum efficiency, defined as the ratio between the detected and incident electrons, is fairly low ($< 50\%$) extending the acquisition time and inducing more damage during the experiment [29]. Furthermore, a gain reference measurement is needed to correct the reconstructed image since the holes are not identical and can have a significantly different electron amplification factor. Finally, the

MCPs are not radiation hard and cannot handle a large electron current (<1 pA) making them less suitable for electron microscopy.

Direct Electron Detector

Contrary to CCDs and DLDs, the direct electron detector does not convert the incoming fast electron into photons or an electron cloud but has the electron deposit its energy directly into the detection layer. This brings a number of advantages for electron detection which will be discussed in this section. There are two different types of direct electron detectors both having a distinct method of operation:

- Monolithic active pixel sensor (MAPS)
- Hybrid pixel detector

MAPS Detector: The MAPS detector uses CMOS technology where each pixel contains an independent amplifier, called the active pixel sensor [30]. Hence the sensor and readout electronics lay in the same single plane. These detectors are usually backthinned (50 μm) to reduce backscattering from the substrate which increases the PSF [31]. Hence the incoming electrons are mainly transmitted through the detector where only a fraction of their energy is deposited. The cross section of the detector can be divided into three regions. The top layer where the electrons enter the pixel which is a passivation layer. The next layer is the lightly doped p^- layer which contains the n-well diodes and the p^- wells. The free charge carriers deposited in this region are collected and make up the signal. The last layer in each pixel consists of heavy doped p^{++} substrate which does not participate much in the signal creation [32]. The MAPS detector has relatively small pixels (5-15 μm) which allows a large number of pixels ($\geq$4096 $\times$ 4096). Due to their high DQE, they are able to detect single electrons. Furthermore, the speeds at which these detectors operate is in the order of 1000 fps which is faster than the typical speeds of a CCD [33]. These detectors were of utmost importance for cryo-EM where the limit on the resolution is due to the beam damage effects and not by the instrument. Therefore,

improving the dose efficiency of the detectors made a huge impact for structural biology as it reveals almost the complete structure of e.g. viruses and proteins [34, 35]. For 4D STEM experiments, these types of detectors are less suited since they are not radiation hard due to the very thin electron sensitive volume.

Hybrid Pixel Detector: The hybrid pixel detector consists out of two parts, the detection layer which is bump-bonded to the second part, an underlying application-specific integrated circuit (ASIC) [21] where in Fig. 1.3 a schematic overview is shown. The detection layer consists out of a relatively thick (~300 μm) sensitive p-n junction semiconductor layer. The two most common materials for the detection layer are Si and CdTe where for electron detection mainly Si is used. A bias voltage is applied perpendicular over the sensor chip to collect the free charge carriers which where created during the interaction of the incoming electron with the detection layer. The ASIC processes the signal which is created in the detection layer when the incoming electron deposits its energy inside this thick layer. These detectors have mainly two operation modes, the integration mode where the deposited energy per frame is recorded or the counting mode which counts the number of pulses coming in giving the capability of single electron counting. In order to distinguish which incoming signals are valid to use in the integration or counting procedure, a threshold should be chosen [36]. The signal is only passed if it exceeds the threshold value which reduces the readout noise to almost zero since the energy of the incoming electron is significantly larger than the thermal noise present. The size of the pixels is generally 55 $\times$ 55 μm hence one incoming electron can deposit energy in multiple pixels increasing its PSF due to sideways scattering. Note, that in order for the electron to be detected in both pixels, the threshold should be exceeded in both the pixels so sub-threshold energy deposition of the electron in one of the two pixels will only excite one pixel. The advantage of these detectors is that they are radiation hard since the electronics are protected by the thick detection layer on top. Furthermore, due to the pulse processing and threshold, no dark noise and readout noise is present. The dynamic range depends on the bit depth of the counter which can go up to 24 bits which is significantly higher than the MAPS or CCD detectors. The fact

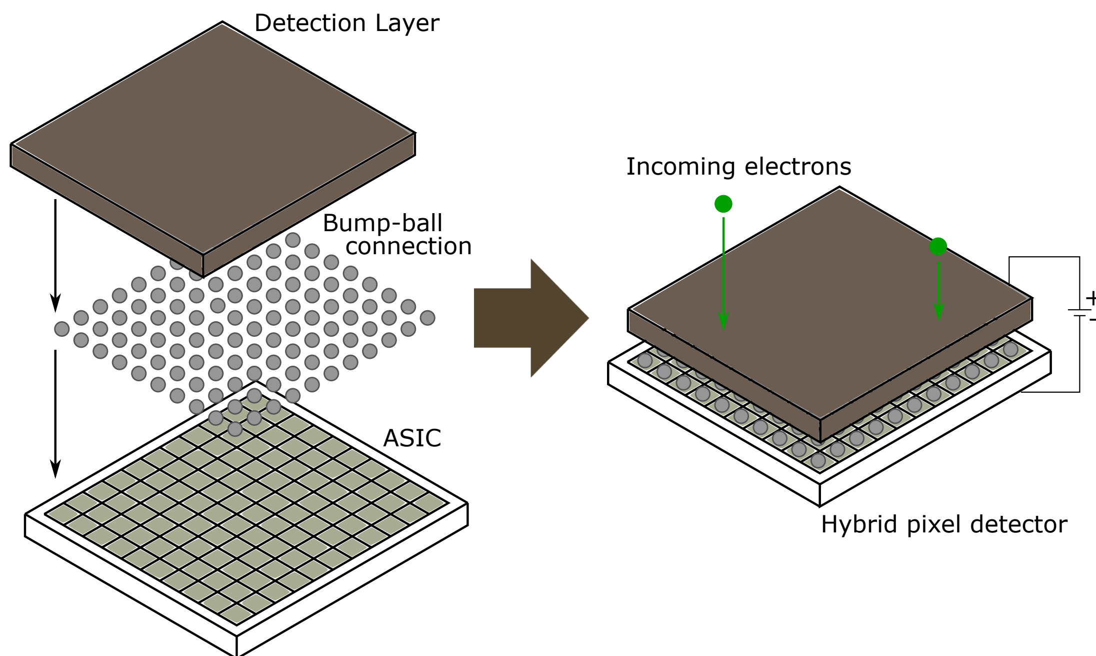

Figure 1.3.: A schematic overview of the hybrid pixelated detector where the three main components, detection layer, bump ball connections and ASIC are indicated.

that each pixel is an electron counter influences the readout speed of the detector where speeds in the order of kHz can be obtained. One disadvantage is the that the number of pixels, on average 256 × 256, available is a lot smaller than for MAPS and CCD cameras making hybrid pixel detectors not very attractive for cryo-EM where a large number of pixels is needed. The main interest of these fast, beam hard detectors is for electron diffraction experiments where images can be recorded of an intense electron beam at maximum 80 kHz making it the optimal detector for 4D STEM experiments. However, the maximum speed is still an order of magnitude slower than the typical speeds used for conventional STEM acquisitions.

Apart from the frame-based hybrid pixel detectors, another type of operation mode has been developed where, instead of integrated signal or counts, the TOA is detected. These are the

Timepix detectors which were developed by the Medipix Collaborations [37]. These types of detectors can be operated in event driven mode where for every incoming event, the point of impact and TOA, with nanosecond resolution, are determined. Since the events are continuously read out, there are no frames or dead time. However every pixel itself has a dead time which is determined by the time it takes to process the incoming signal (~500 ns). This puts a limit on the maximum count rate available on the detector which is ~0.4 Mhits/mm^2/s. This corresponds to an electron current of ~5 pA which is on the low side making them less attractive for the use of conventional STEM where currents of ~50 pA are typically used. In *Chapter 4*, the Timepix3 detector is used to perform very fast 4D STEM experiments and in *Chapter 5* the nanosecond precision TOA gives the ability to measure the temporal correlation between inelastic electrons and x-rays.

1.2.2. X-ray Detection

Contrary to electron detection, where the spatial distribution of the probability density is measured, the energy of the x-ray is of main interest. The x-ray detection scheme to determine its energy consists out of two parts, the x-ray detector and the pulse processor. The x-ray interacts with the detector and deposits its energy via the creation of an electrical signal. The second part, where the pulse processor is used, handles the electrical signal and determines the energy of the x-ray.

Detector

In general, the detector consists out of a p-n junction semiconductor where a reverse bias is applied to extend the depletion zone which is known as the active area. When an incoming x-ray interacts with the detector material, electron-hole pairs are created. The energy needed to create such an electron-hole pair depends on the ionization energy of the semiconductor. For instance, the ionization energy for Si is ~3.6 eV. Hence for an x-ray in the keV range, many electron-hole pairs are created via this interaction. A bias is applied over the active area

of the detector which creates an electric field which guides the electrons towards the anode. This charge is collected on the anode, and converted to a voltage signal using a field-effect transistor (FET) preamplifier. The amplifier converts the current pulse, which is proportional to the x-ray energy via the number of electron-hole pairs, to a voltage signal that is fed into the pulse processor.

The main effect of the broadening on the energy, arising from the detector, is due to the variance in the number of created charge carriers. For this reason, a semiconductor has a better energy resolution compared to gas-filled detectors where ∼30 eV is needed to create charge carriers. To further improve the energy resolution, the detectors are cooled which reduces the thermal fluctuations.

In recent years, the silicon drift detectors (SDD) have been growing in popularity since they outperform the Si(Li) detectors in terms of energy resolution and higher count rates available due to the smaller capacitance of the detector [38]. This low capacitance is possible because the anode can be made smaller since ring electrodes are used to create an electric field gradient to guide the charge carriers towards the anode. Another advantage is that the SSD only uses a Peltier cooler since it can be operated at -20°C compared to Si(Li) detector which needs to be permanently cooled to liquid nitrogen temperatures to reduce the drift of the Li [39]. One disadvantage of the SDD lies in the fact that a small anode is used which makes the travel time of free charge carriers dependent on the position where the x-ray interacts in the active area reducing the accuracy on the TOA determination. In *Section 5.4.7*, the broadening on the TOA from a SDD detector is shown and potential methods to improve the temporal resolution are discussed.

Digital Pulse Processing

The outputted preamplifier signal is used to get the energy of the signal. In the last decade, the digital pulse processors (DPP) are gaining interest since they are able to perform the same type of pulse processing as the older analog method while also adding flexibility due to the

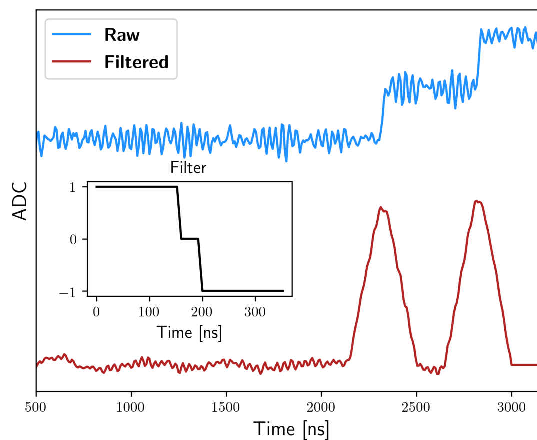

Figure 1.4.: Example waveform from an energy dispersive x-ray detector (blue), note the two steps indicating the presence of two x-rays arriving. The inset figure shows the filter used to create the trapezoidal signal (red) from which the energy of the x-ray can be determined.

software implementation of the required functions [40–42]. In Fig. 1.4, the signal coming into the DPP is shown where two large steps in voltage are seen which indicates the presence of two x-rays in the selected time window. The energy is determined by convolving the signal with a trapezoidal filter where the height of the filtered signal is proportional to the energy [43]. In Fig. 1.4, an example filter is shown in the inset figure. The filtered output is seen in red from which the energy is determined by the peak height. Note that the energy resolution can be improved by increasing the filter length, since the integration will be performed over a larger time span which reduces the influence of the noise. However, if inside the filter time window a new x-ray arrives, there will be no distinction between the two x-rays and they will be counted as one x-ray with an energy equal to the sum of the two x-ray energies. This is commonly known as pulse pile up. Another advantage of the DPP is that they give the ability to recording a list mode where for each x-ray the energy and TOA, with nanosecond resolution, is stored. This generates substantially more data compared to the generation of a single x-ray spectrum.

However this gives the ability to look at dynamical processes which occur in the nanosecond range.

2. How to perform electron scattering experiments: The Electron Microscope

In *Section* 1.1, a subset of electron scattering interactions are described and how these types of scattering can help unravelling the structure of the specimen. In this chapter, multiple experimental methods which rely on different scattering interactions which occur inside the electron microscope are discussed. Before the different electron microscopy methods are described, a general concise overview of the electron microscope is given below.

Let's start by dividing the electron microscope into two segments. The first segment of the microscope prepares the state of the incoming electron whereas the second segment collects the outgoing particles in the right mode.

The first segment prepares the incoming electron wave function to be in a particular mode. There are many parameters which can be varied before the electron interacts with the specimen and here we will describe a subset of all possibilities. One important parameter, in the preparation of the incoming electron, is the acceleration voltage which selects the energy/speed of the electrons. This is important since the cross section (elastic and inelastic) depends on this parameter. For instance, when performing experiments on graphene, the acceleration voltage should be below 80 kV since above this value, a rapid increase of beam damage occurs [44]. Another frequently used parameter is the convergence angle which determines the size and shape of the incoming electron beam. In general, the larger the convergence angle, the smaller the probe. However for large convergence angles, aberrations will become dominant increasing the probe size again. For this reason, probe-corrected aberration electron microscopes have

been developed which can reduce the aberrations up until a certain angle [45–47].

The second part of the microscope after the specimen is used to collect the appropriate signals. In the TEM there are two frequently used acquisition modes, image and diffraction mode where for image mode, an objective lens after the specimen is used to make a magnified image. When using diffraction mode, the back focal plane is imaged on the detector where if needed an energy filter is used to remove the inelastically scattered electrons. On the other hand, when performing measurements on the inelastic scattered electrons, a magnetic prism is used to disperse the electrons and retrieve an electron energy-loss spectrum.

In this work two types of electron microscopes are used, TEM and the scanning electron microscope (SEM). Both microscopes are able to perform electron scattering experiments but they have significant differences between them. In general, the SEM is used to measure the backscattered electrons, without any lenses underneath the specimen, whereas TEM/STEM measures the transmitted electrons. Therefore, the specimens in TEM/STEM need to be thin (max ~200 nm) and higher acceleration voltages (60-300 keV) are used to increase the mean free path such that the specimens are approximately electron transparent. The SEM can also be used to measure the transmitted electrons however, the specimens used should be even thinner where 2D materials (see *Chapter 3*) or nano particles can still be used. Moreover, the spatial resolution available in TEM/STEM is better, making it easier to get atomic resolved images. On the other hand, the field of view (FOV) in the TEM/STEM is limited to a couple of μm^2 whereas in the SEM it is possible to get mm^2 scans. Another large difference lies in the cost of TEM/STEM which is an order of magnitude larger than the SEM and the mode of operation is much easier for SEM which makes automating the experiments more accessible where for TEM/STEM a much steeper learning curve is present.

All in all, both TEM/STEM and SEM are perfectly fine devices to perform a multitude of electron scattering experiments due to its many different parameters which can be varied. A proper choice of microscope and operation mode should be made beforehand to retrieve the best results. In the rest of this chapter, the relevant operation modes for this theses are discussed.

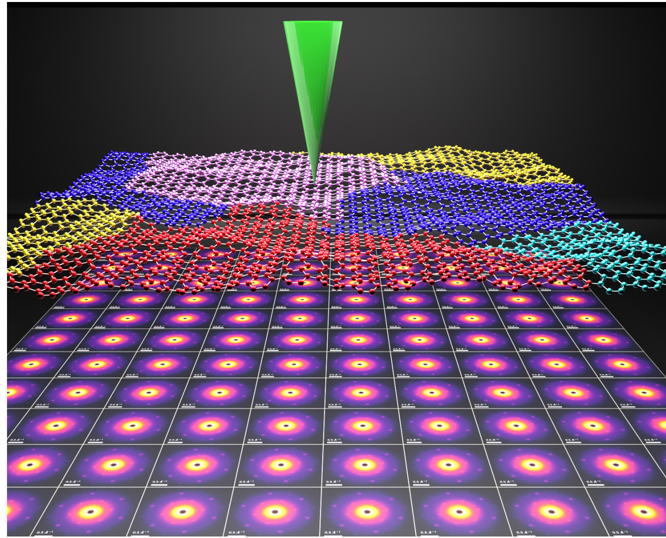

Figure 2.1.: Schematic overview of the 4D STEM technique where a probe is raster scanned over the specimen, in this case graphene, and at every probe position a diffraction pattern is acquired.

2.1. 4D STEM

One mode in the electron microscope uses a condensed electron beam which is scanned over the material and at every probe position, a diffraction pattern in the far-field regime is acquired. This method is named 4D STEM since a two dimensional raster scan is performed where at every position, a two dimensional diffraction pattern is recorded. In Fig. 2.1, a schematic overview of the 4D STEM method is shown. Contrary, to other STEM acquisition modes where an annular detector is used to record one intensity per probe position, with the 4D STEM method 65536 intensities are recorded at one probe position for a 256×256 pixelated detector giving the freedom to construct multiple signals in the post processing. Next to the increased possibilities of image reconstruction, the data size also increases by a factor of 65536 making the data analysis more complex. For this reason many different software have been developed to handle such

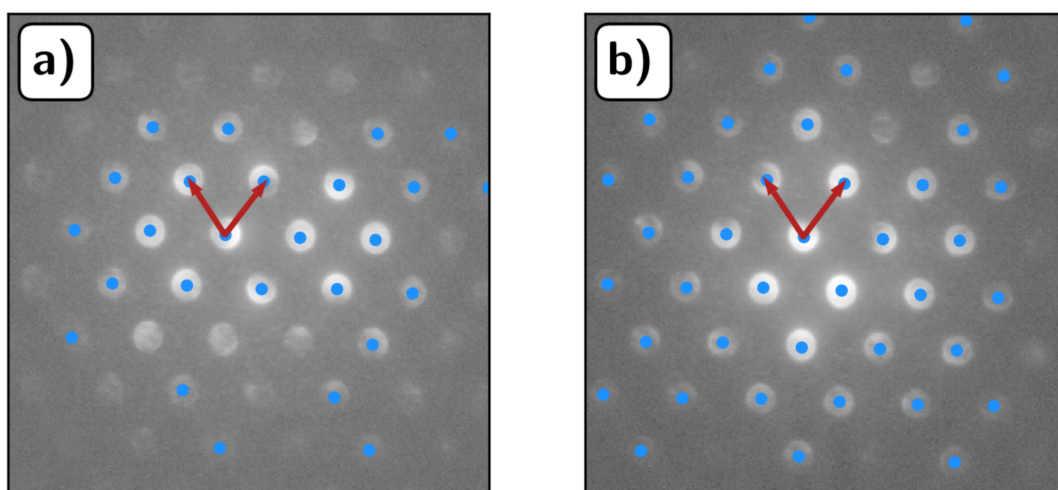

Figure 2.2.: **(a,b)** The diffraction pattern of single crystalline silicon (a) and germanium (b). The peak positions which are found by the algorithm are indicated and the arrows indicate the fitted basis vectors which will be used to determine the strain in the sample

large datasets [48–52].

The 4D STEM method is used to extract multiple types of information going from the nanometre scale down to atomic scale where it is used to map long range magnetic/electric fields [53–55] and atomic electric fields [56, 57]. Furthermore, the 4D STEM method can identify strain in crystalline and amorphous materials [58, 59]. Moreover for amorphous materials, fluctuation electron microscopy is used to characterize some aspects of the structure[60] In the rest of this section, two different 4D STEM methods, which are used in *Chapter 3* and *Chapter 4*, are discussed more in depth.

2.1.1. Nano Beam Electron Diffraction

In nano beam electron diffraction (NBED) a nanometre sized probe is scanned over the specimen where at every probe position a diffraction pattern is recorded. The real space size of the probe is restricted by the choice of convergence angle where in general an angle is chosen that the bragg reflections of the crystalline structure do not overlap. These diffraction patterns give information on the local structure of the material such as orientation and lattice parameter. In Fig. 2.2, two example diffraction patterns coming from a silicon (a) and germanium (b) crystal are shown. From such a diffraction pattern, the two basis vectors which describe the spot positions can be extracted. Many algorithms have been developed to extract accurate spot positions which makes use of the Hough transform, cross correlations or edge disc detection [61–64]. In Fig. 2.2, the found peak positions are marked whereas the fitted reciprocal basis vector is also indicated with the red arrow. After the peak finding algorithm, a linear least square fit is performed to retrieve the two reciprocal basis vectors $\vec{v}_1$ and $\vec{v}_2$ resulting in a matrix G [58].

$$G = \begin{bmatrix} v_{1,x} & v_{2,x} \\ v_{1,y} & v_{2,y} \end{bmatrix} \tag{2.1}$$

The strain, shear and in-plane orientation can be retrieved by calculating the affine transformation A between the matrix G and a reference G_0 which is described by following equation:

$$A = G_0 G^{-1} \tag{2.2}$$

The in-plane rotation (θ), strain (ϵ_{xx}, ϵ_{yy}) and shear (ϵ_{xy}) and are found by performing a polar decomposition on A:

$$A = \begin{bmatrix} \cos\theta & -\sin\theta \\ \sin\theta & \cos\theta \end{bmatrix} \begin{bmatrix} c_{xx} & c_{yx} \\ c_{xy} & c_{yy} \end{bmatrix} \tag{2.3}$$

$$\epsilon_{xx} = c_{xx} - 1 \qquad \epsilon_{yy} = c_{yy} - 1 \qquad \epsilon_{xy} = \frac{c_{xy} + c_{yx}}{2} \tag{2.4}$$

The methodology explained is used for every acquired diffraction pattern. Hence for every probe position the affine matrix A can be retrieved giving access to the strain and orientation map.

Another application of NBED is for orientation mapping of materials where the diffraction pattern gives information on the crystal orientation with respect to the incoming electron beam. Grain size, local texture and twin boundaries can be extracted from the orientation map which are important in understanding the properties of materials [65–67]. The orientation can be determined via first performing the peak finding algorithm and secondly comparing the peak positions and its intensities with a simulated library where the best match with the library gives the orientation.

This technique is developed for the use in the TEM however the FOV is limited in this microscope making it difficult to gather large statistical data on the specimen. Furthermore, due to the complicated mode of operation and elaborate specimen preparation/insertion, the TEM is not the ideal device to perform fast automated characterization of materials. In *Chapter 3*, a novel setup is described where NBED experiments are performed in a SEM showing FOV scans in the mm^2 range where the simpler mode of operation of the SEM makes this method advantageous for fast automated characterization.

2.1.2. High Resolution Imaging

In the TEM, a sub-angstrom size probe can be achieved by using a aberration-corrected microscope with a large convergence angle. This operation mode is used to get atomic resolution images by scanning the probe over the specimen and acquiring a signal, depending on the detector configuration used, at every probe position. The conventional STEM methods use an annular detector ring where the choice of inner and outer angle determine the contrast in the image. For instance, for annular dark field (ADF), the inner angle is chosen to be larger than the central bright disc giving a dark field type of contrast (see Fig. 2.3(d)). In Fig. 2.3(b), the position averaged convergent electron diffraction (PACBED) pattern of a simulated $SrTiO_3$ with one unit cell thickness is shown. The simulation uses a convergence angle of 25 mrad with an acceleration voltage of 300 kV. The simulations are performed using the open-source software Multem with the multislice algorithm [68, 69]. The different virtual detector representing bright

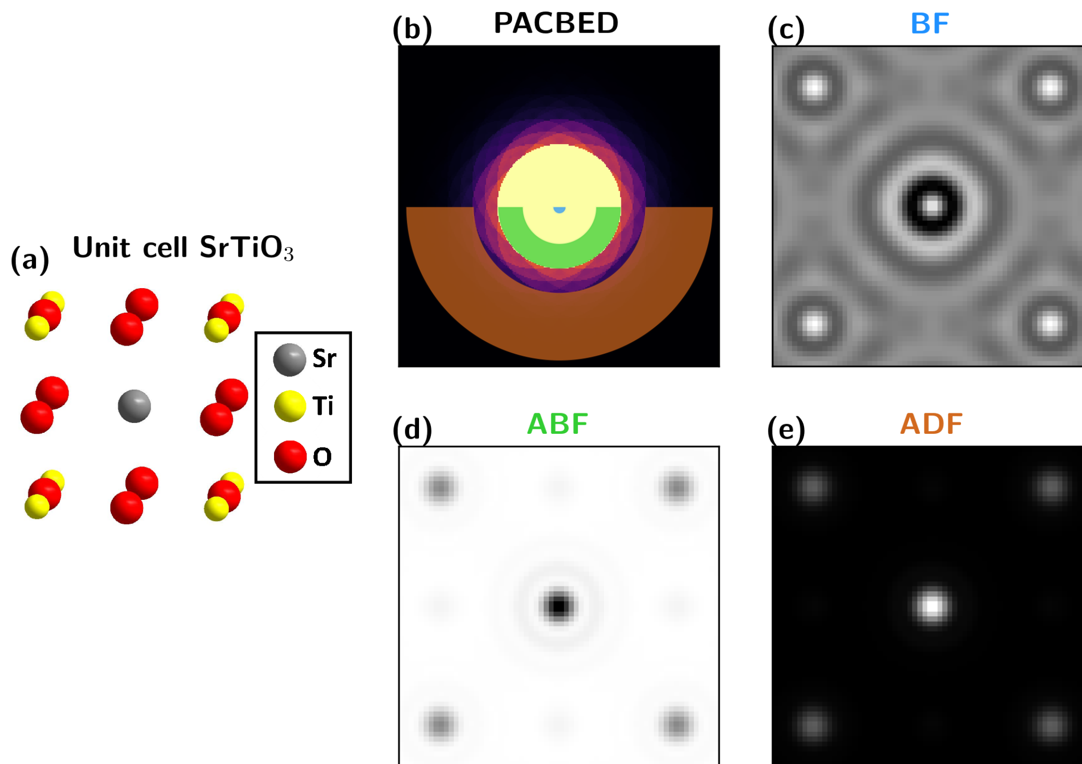

Figure 2.3.: **(a)** The simulated unit cell of $SrTiO_3$ **(b)**The PACBED is shown where the lower halve of the different virtual detectors are indicated. The colors of the virtual detectors correspond to the title of the reconstructed images. **(c)** The bright field image coming from the blue detector configuration. **(d)** The annular bright field image coming from the green detector configuration. **(e)** The annular dark field image coming from the orange detector configuration. Note the strong effect on the contrast depending on the detector geometry chosen.

field (BF), annular bright field (ABF) and ADF are shown in Fig. 2.3. The colors shown in the title correspond to the color of the virtual detector. These methods use only an integrated signal whereas in 4D STEM, the entire far-field pattern is recorded giving the ability to select the detector configurations in post processing to get the appropriate signal as seen in Fig. 2.3 [50]. However, the annular detector signals are not dose efficient which is of utmost importance when performing experiments on beam sensitive materials [70, 71]. Therefore, more advanced types of processing on the 4D STEM data can be performed to improve the contrast for the low dose experiments. In this section, two frequently used dose efficient methods that are described are the integrated centre-of-mass and the single side band ptychographic reconstruction.

Integrated Centre-of-Mass

The integrated center-of-mass (iCoM) uses the first moment ($\langle\vec{k}\rangle$) of the diffraction pattern to reconstruct the specimens projected electric potential. In order to show how the first moment gives a signal corresponding to the potential, we start by rewriting Eq. 1.6 where another variable is introduced which described the change of the specimens positions with respect to the incoming probe:

$$\Psi_{out}(\vec{k},\vec{r_p}) = \mathcal{F}\left\{\psi_{in}(\vec{r})\cdot e^{i\Delta\phi(\vec{r}+\vec{r_p})}\right\}(\vec{k}) \tag{2.5}$$

where $\vec{r_p}$ is the new position of the specimen with respect to the electron probe. We start by describing the x component of the first moment ($\langle k_x\rangle$) from the far-field pattern:

$$\langle k_x\rangle(\vec{r_p}) = \iint_{-\infty}^{\infty} k_x|\Psi_{out}(\vec{k},\vec{r_p})|^2 d^2\vec{k} \tag{2.6}$$

This equation can be simplified by making use of the properties of the Fourier transform (see Lazić *et al.* [72] for the full derivation) into the following:

$$\langle k_x\rangle(\vec{r_p}) = \frac{1}{2\pi i}\iint_{-\infty}^{\infty} \frac{\partial\psi_{out}(\vec{r},\vec{r_p})}{\partial x}\cdot\psi^*_{out}(\vec{r},\vec{r_p})d^2\vec{r} \tag{2.7}$$

by using the phase approximation of Eq 1.5, Eq. 2.7 can be simplified to the following:

$$\langle k_x\rangle(\vec{r_p}) = \frac{1}{2\pi i}\iint_{-\infty}^{\infty} \frac{\partial\psi_{in}(\vec{r})}{\partial x}\psi^*_{in}(\vec{r})d^2\vec{r} + \frac{1}{2\pi}\iint_{-\infty}^{\infty} |\psi_{in}|^2\frac{\partial\phi(\vec{r}+\vec{r_p})}{\partial x}d^2\vec{r} \tag{2.8}$$

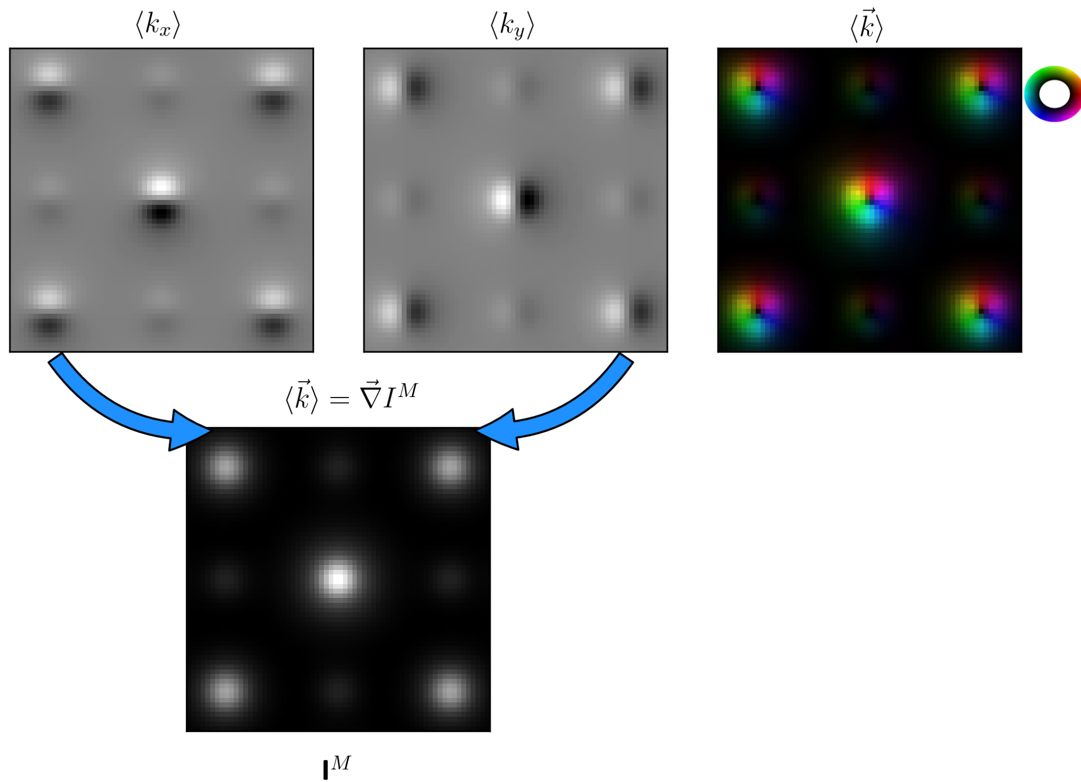

Figure 2.4.: The x and y-component of the first moment calculated from the 4D STEM dataset. The first moment vector $\langle \vec{k} \rangle$ is shown where on the atomic positions, the magnitude of $\langle \vec{k} \rangle$ is small since no electric field is present on the atomic positions. The integrated signal, derived from the first moment using the algorithm described in Eq. 2.11, is shown where the correspondence with the projected potential is identified.

Note that the first term does not depend on $\vec{r_p}$ which results in a constant value. The second term can be identified as the cross correlation ($\star$) between $|\psi_{in}|^2$ and $\frac{\partial \phi}{\partial x}$. The same type of derivation can be performed for the y-component of the first moment after which the first moment vector ($\langle \vec{k} \rangle$) becomes:

$$\langle \vec{k} \rangle(\vec{r_p}) = \langle k_x \rangle(\vec{r_p})\vec{e_x} + \langle k_y \rangle(\vec{r_p})\vec{e_y} = Cte + \frac{1}{2\pi}\left(|\psi_{in}(\vec{r})|^2 \star \vec{\nabla}\phi(\vec{r})\right)(\vec{r_p}) \tag{2.9}$$

This shows that the first moment of the measured intensity pattern depends on the phase gradient of the projected potential ϕ, which the projected electric field. To reconstruct an image which is linear with respect to ϕ, the first moment should be integrated and this is referred to as the integrated center of mass signal(I^M). Hence, the relation between the $\langle \vec{k} \rangle$ and I^M is following:

$$\langle \vec{k} \rangle(\vec{r_p}) = \vec{\nabla} I^M(\vec{r_p}) \tag{2.10}$$

One possible method to find I^M is by doing the integration in the Fourier domain and making use of the Fourier differentiation property.

$$\mathcal{F}\{I^M(\vec{r_p})\} = \frac{\vec{k_p}\mathcal{F}\{\langle \vec{k} \rangle(\vec{r_p})\}(\vec{k_p})}{2\pi i k_p^2} \tag{2.11}$$

By simplifying Eq. 2.11 and taking the inverse Fourier transform the final result is obtained:

$$I^M(\vec{r_p}) = \frac{1}{2\pi}\left(|\psi_{in}(\vec{r})|^2 \star \phi(\vec{r})\right)(\vec{r_p}) \tag{2.12}$$

This shows that the I^M is given by the cross correlation between the incoming probability density and phase shift which as seen from Eq. 1.1 is proportional to the projected electric potential when no magnetic interaction is taken into account. Furthermore, the first moment depends on the gradient of the phase which is the projected electric field. In Fig. 2.4, the same simulated dataset using $SrTiO_3$ is used to calculate the x and y-component of the first moments. The vector plot is shown where it is clear that the first moment describes the electric field of the atomic potentials. The integrated signal (I^M) shows a linear signal with respect to the electric

atomic potential; notice that the oxygen starts to be visible whereas detecting the presence of the oxygen atoms with the annular detector is hard (see Fig. 2.3). The POA was used to describe the specimen during the derivation of the iCoM signal. Hence, the iCOM signal does not represent the projected electric atomic potential for thicker specimens, therefore this method is not able to quantify their projected potential [73]. Next to iCoM imaging, integrated differential phase contrast imaging exists, which uses a quadrant detector to get an approximation of the first moment at every probe position [72]. The advantage of using the quadrant detector is that much higher readout speeds can be obtained as four quadrants each have their own individual readout electronics. This is much faster than the serialised output stream of a conventional CCD camera with multi-million pixels. However, the first moment is only approximated using the quadrants which introduces a non-isotropic contrast transfer function. This introduces an error for the quantification of the atomic electric field and potential [74].

Ptychography: Single Sideband Reconstruction

Electron ptychography uses the redundant 4D STEM data to reconstruct the object under illumination. There are two branches of ptychographic reconstruction, where one retrieves the object via an analytical solution such as the single sideband reconstruction (SSB) [75] and the Wigner distribution deconvolution method [76]. The other branch uses iterative algorithms to retrieve the phase and amplitude of the object by knowing the incoming probe and updating the guessed object until the best match is found with the experimental diffraction patterns [77–79]. In this work, the SSB algorithm is discussed since this is used in *Chapter 4*.

Let's start from Eq. 2.5, where the measured diffraction pattern is given by the square modulus of this function. The Fourier transform with respect to the probe position coordinate ($\vec{r_p}$) can be performed:

$$G(\vec{k}, \vec{k_p}) = \int |\Psi_{out}(\vec{k}, \vec{r_p})|^2 \cdot e^{2\pi i \vec{k_p} \cdot \vec{r_p}} \cdot d\vec{r_p} \tag{2.13}$$

The next step is to invoke the weak phase object approximation (WPOA) which approximates $e^{-i\Delta\phi(\vec{r})}$ as $1 - i\Delta\phi(\vec{r})$ which is valid when $\Delta\phi << \pi/2$. From this a scattered wave β_s is defined

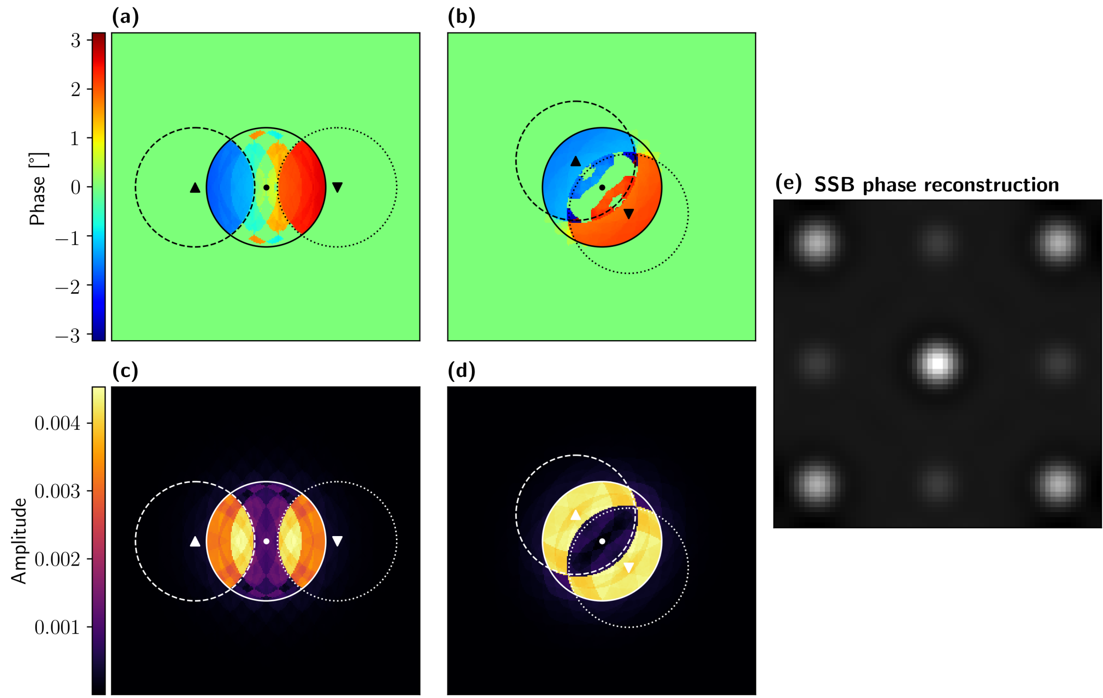

Figure 2.5.: **(a,b)** Two maps where the calculated phase of G is plotted for two different orientations of $\vec{k_p}$. The maps arise from the simulated $SrTiO_3$ dataset which uses the multisclice method instead of the WPOA for the simulation. The three discs, two scattered and one unscattered, are indicated on the figures where in the double overlap region, the phase $\Delta\phi(\vec{k_p})$ is given which for both regions is π out of phase. In the triple overlap, the theoretical value when using the WPOA should be zero. However since the simulations were done using the multislice method, which better approximates reality, some residual signal is seen. **(c,d)** Similar to (a,b) except the amplitude of G is shown. The non homogeneities arise from the fact that the specimen does not really fulfill the WPOA. **(e)** The reconstructed phase using the SSB algorithm.

as following:

$$\beta_s(\vec{k}) = -i\Delta\phi(\vec{k}) \tag{2.14}$$

where $\Delta\phi(\vec{k})$ is the Fourier transform of the phase shift (see Eq. 1.1). Using this approximation, Rodenburg *et al.* [75] shows that G becomes:

$$G(\vec{k}, \vec{k_p}) = |\Psi_{in}(\vec{k})|^2\delta(\vec{k_p}) + \Psi_{in}(\vec{k})\Psi^*_{in}(\vec{k} + \vec{k_p})\beta^*_s(-\vec{k_p}) + \Psi^*_{in}(\vec{k})\Psi_{in}(\vec{k} - \vec{k_p})\beta_s(\vec{k_p}) \tag{2.15}$$

The first term of Eq 2.15 is only non-zero when $\vec{k_p} = 0$ which is the modulus squared of the incoming wave in the back focal plane being the aperture function from Eq. 1.2. The other two terms of Eq 2.15 describe a logical AND function which is only non-zero where the central disc and scattered disc at $\vec{k_p}$ or $-\vec{k_p}$ overlap. The value at the double overlap region is equal to the Fourier transform of the phase shift (see Eq 2.14). In the region where the two last terms are both non zero, which is called the triple overlap region, the value for G is equal to $\beta^*_s(-\vec{k_p}) + \beta_s(\vec{k_p})$. The phase shift is a real valued function, $\beta_s(\vec{k_p}) = -\beta^*_s(-\vec{k_p})$ resulting that the sum is equal to zero. In Fig. 2.5(a,b) the phase of G for two examples, using different values of $\vec{k_p}$, are shown. The same simulation of $SrTiO_3$, as in Fig. 2.3, was used for the SSB reconstruction. Note that the simulation used the multislice approximation and therefore does not fulfill the WPOA which results in some small deviation from analytical theory. The different discs are indicated with the double overlap giving the phase and the triple overlap regions (see Fig 2.5(b)) giving a zero value in the WPOA. Nonetheless, there is still some residual signal since the multislice, which better approximates reality, is used. In Fig. 2.5(c,d), the amplitude of the complex valued G is shown where again the non homogeneities arise from higher order effects since the multislice algorithm was used.

The final step to retrieve $\Delta\phi(\vec{r})$ is to select the region inside the double disc overlap for every $\vec{k_p}$ which gives $\beta_s(\vec{k_p})$. The real space phase ($\Delta\phi(\vec{r_p})$) is obtained by Fourier transforming $i\Delta\phi(\vec{k_p})$ where the result is shown in Fig. 2.5(e).

It is necessary for both iCoM, and especially SSB, to measure the diffraction pattern at every probe position. Hence fast pixelated detectors are of crucial importance. However as

seen in *Section 1.2.1* the frame-based detectors are still an order of magnitude slower than the conventional STEM techniques. Therefore, the implementation of 4D STEM using an event driven detector can overcome the limit on the frame rate of the detector where the results are shown in *Chapter 4*.

Low dose regime

In the two previous sections, two algorithms were applied to retrieve a signal from the 4D STEM data where the reconstructed signal corresponds to the atomic potential. To show that they are more robust to noise, the same simulated 4D dataset with the $SrTiO_3$ is used where the total number of electrons is varied and Poisson noise is added to mimic the noise present in the real experimental data. In Fig. 2.6, the different reconstructed signals are shown for multiple total doses (N_e). The BF and ABF do not show any atomic features at low doses. The ADF is very noisy since almost no electrons scatter at these high angles but some atomic contrast is still present

show some atomic contrast at the lowest dose which makes these methods very interesting for low dose experiments where the specimens are beam sensitive and undergo beam damage relatively fast.

2.2. Electron Energy Loss Spectroscopy

Electron energy loss spectroscopy (EELS) is the technique which analyses the energy distribution of the inelastic scattered electrons. Usually these experiments are performed with a condensed incoming electron probe such that, similar to STEM, the beam can be scanned over the specimen where at multiple points, the energy loss spectrum can be measured. EELS provides a wealth of information about the specimen such as chemical content of the specimen, vibrational spectroscopy, plasmonics, specimen thickness, *etc.* [11, 80–83]. Moreover, the fine structure of the inner shells provide chemically specific insight into the bonding and oxidation

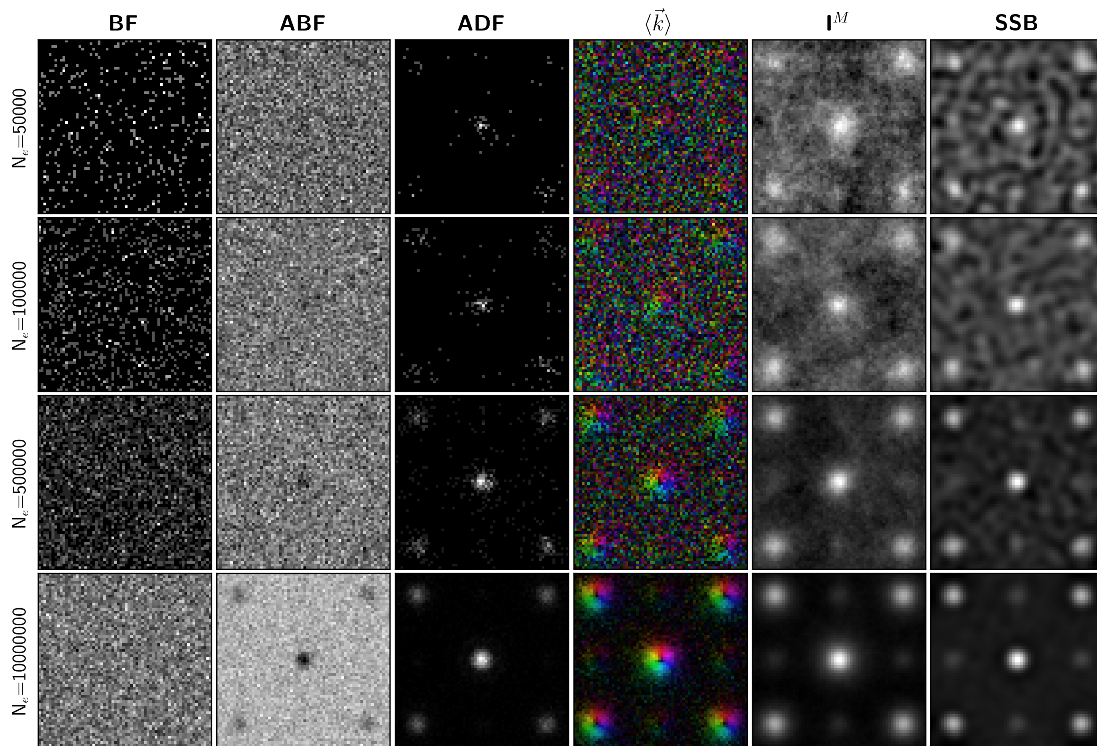

Figure 2.6.: The different images reconstruction which are described in this section where the total number of electrons in the dataset is indicated on the left. For low doses it is clear the the iCoM and SSB reconstruction are able to better resolve the atomic structure of the $SrTiO_3$.

states [84, 85]. All this is combined with the high spatial resolution where the small size of the electron probe enables this type of information at the atomic scale.

2.2.1. EELS Setup

When electrons are inelastically scattered from the specimen, the energy of the outgoing electron should be determined. One possibility would be to measure the energy deposited inside a semiconductor similarly to the x-ray detection method (see Section 1.2.2). However, the energy resolution using this type of detection is very poor (~100 eV). Another method would be to separate the energies in space, this is commonly done in optics where a prism is used to disperse the incoming light. The equivalent of such a prism in electron optics is the magnetic prism where due to the Lorentz force, electrons at different velocities are subjected to different forces hence the deflection depends on the energy of the electron.

An aperture is placed before the magnetic prism, where, when the TEM is operated in diffraction mode, the collection angle for the EEL spectrum can be chosen. The collection angle is an important parameter in the EELS acquisition since every type of inelastic scattering has a particular angular scattering distribution where even the crystal orientation of the specimen affects this distribution. Thus, via smart choice of collection angles, the SNR of a particular core-loss edge can be improved [86].

The energy resolution of the EELS setup is important since some features will be lost when the resolution is not sufficient and also the SNR depends on the resolution. The main limit arises from the energy spread of the incoming electron beam which is generated via an electron source. In an electron microscope different types of sources are available, one of them are the field emission guns which can achieve a spread of ~0.3 eV. This can be made even smaller via the use of a monochromator. This apparatus is able to reduce the energy spread of the incoming electrons. The monochromator can be seen has a magnetic prism where a slit is placed in the dispersion plane which selects only a sub part of the incoming electron beam reducing the energy spread [87]. The placement of the slit also removes a large portion of the incoming

electron beam current reducing the maximum available current.

The last step, after the electrons have passed the prism, is the detection of the electrons using a pixelated camera where the different types of camera were explained in *Section 1.2.* Since EEL spectra are recorded when scanning the electron probe over the specimen, the maximum scan speed is limited by the frame rate of the camera which are in the order of ms for conventional CCDs. Therefore, the fast hybrid pixel detectors (10000 fps) seem to be very attractive for EELS experiments. Additionally, these detectors provide a large dynamic range and no readout noise which is beneficial for EELS where the zero-loss peak can be orders of magnitude larger than the signal of interest [88].

2.2.2. Background Subtraction EELS

In Fig. 2.7(a), a typical EEL spectrum is shown where edges arising from the interaction with oxygen, nickel and neodymium are indicated. These edges are accompanied by a large background signal which arises from the inelastic scattering of electrons with lower energy loss. As seen in Fig. 2.7, this background signal is substantial and proper modelling is essential for quantification. In general, this background is fitted with a power law function (AE^{-r}) where the fitting region should be a window before the core-loss edge. Hence for every ionization edge, this power-law fitting should be performed. The fitted background is then extrapolated to model the background signal under the edge. In Fig. 2.7(a), the different fitted background regions are indicated as an area and the extrapolated fits are shown. Notice that due to the limit energy range, the pre-edge of oxygen is too small to provide an accurate fit which is shown in Fig. 2.7(b). In Fig. 2.7(c,d), the background subtracted EEL spectra for the other elements are shown where the background model seems to accurately describe the pre-edge. This method usually works well for thin samples where the core-loss edge has a high SNR, the energy is above 100 eV and no other edge are overlapping [89]. However, these conditions are generally not valid resulting in a poor estimation of the background. Multiple methods have been proposed to get a better estimate on the background where for each different methodology prior knowledge on the

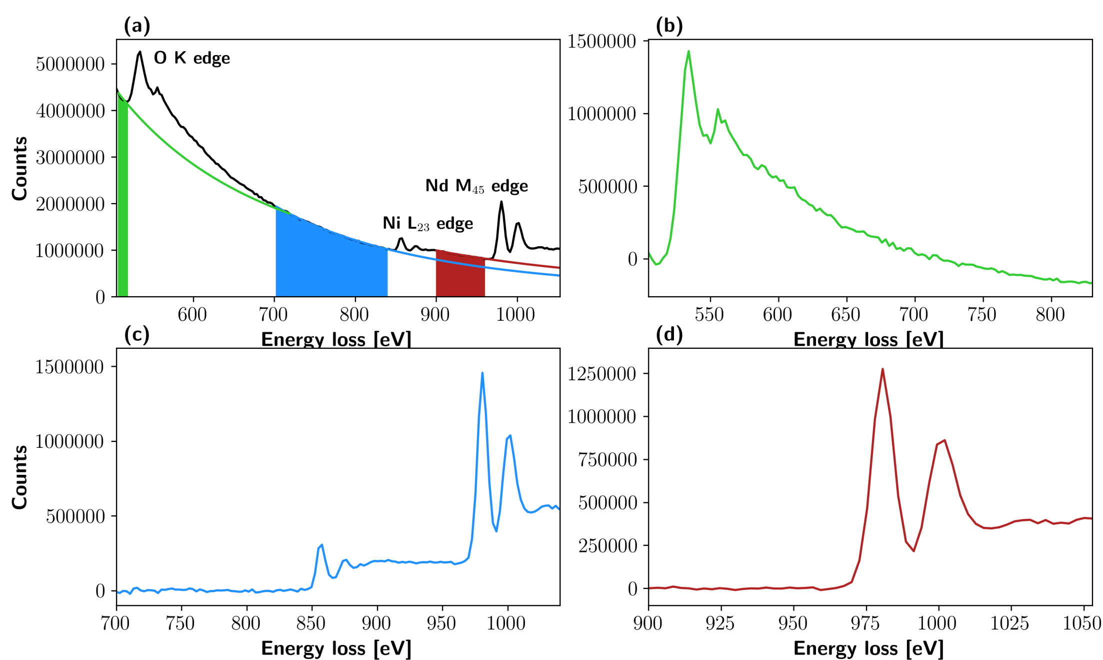

Figure 2.7.: **(a)** An EEL spectrum where oxygen, nickel and neodymium are present in the specimen. The fitted background, using the power-law method, for each edge is shown. The filled area indicates the fitting region and the line shows the extrapolation of the fit. **(b-d)** The background-subtracted spectra of the different elements where the colours correspond to the used background.

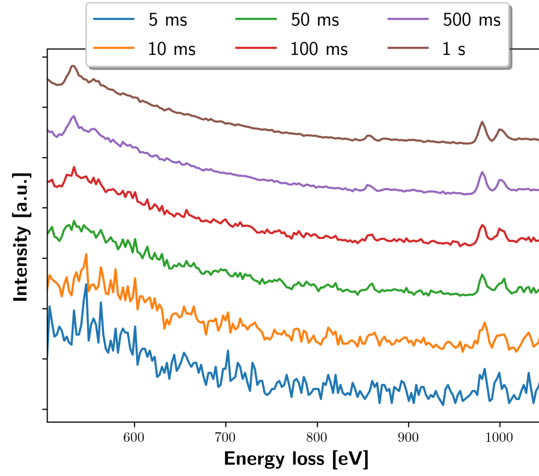

Figure 2.8.: The same EEL spectrum which was shown in Fig. 2.7 where the acquisition time is varied. When the acquisition time is too low, the edges are buried in the noise and not observable. At larger acquisition time, the edge signal emerge from the noise as the SNR is increasing.

background shape is used [90–94]. In *Chapter 5*, a novel method to accurately determine the background signal in EELS is discussed which uses the time correlation with the characteristic x-rays which requires no model of this background signal.

2.2.3. Quantitative EELS

In order to quantify the elemental abundance from the EEL spectrum, a mathematical description on the number of scattered electrons detected coming from a core-loss ($N_{e,e}$) is proposed:

$$N_{e,e} = C \cdot \sigma(\beta, \Delta) \cdot \epsilon_e I t \tag{2.16}$$

where C is the areal density, equal to the product of the concentration and the specimen thickness. $\sigma(\beta, \Delta)$ is the inelastic scattering cross section depending on the beam energy,

energy integration range (Δ) and collection angle (β) of the EELS setup. ϵ_e is the collection efficiency which describes how many of the scattered electrons are really detected, I is the incoming electron current and t is the acquisition time. In Eq. 2.16 the influence of multiple scattering has been excluded. This effect will become dominant for thicker specimen where the multiple scattering results in a convolution of the core-loss edges with the low-loss energy spectrum. However in this description we assume that the specimen is thin enough such that it approximates kinematical scattering.

Apart from the core-loss edge, there is also a background signal ($N_{e,b}$) present in the EEL spectrum which is given by:

$$N_{e,b} = B_e \cdot \epsilon_e I t \tag{2.17}$$

where B_e is the cross section for all processes that contribute to the background. It is possible to describe B_e when the material under investigation is known but this is outside the scope of this work [80]. For quantitative EELS, the first step is the background subtraction where after removal only $N_{e,e}$ remains. From Eq. 2.16 it is clear that the areal density C can be determined when $\sigma(\beta, \Delta)$, ϵ_e, I and t are known. In general, there is more interest in the relative abundance of two elements which is found by taking the ratio between the areal density of element A and B:

$$\frac{C_A}{C_B} = \frac{N_{e,e}(A)}{N_{e,e}(B)} \frac{\sigma_B(\beta, \Delta_A)}{\sigma_A(\beta, \Delta_B)} \tag{2.18}$$

from which it is seen that the ratio is independent of I, t and ϵ_e when approximating that ϵ_e does not depend on the energy loss. From *Section 1.1.2*, it is known that the exact value of the cross sections are difficult to calculate and depend on the chemical environment. However, when the integrated energy window is wide enough to include the fine structure oscillations it is expected that the calculated cross section are accurate within 5% [95].

Since the inner-shell ionization cross sections are relatively small, and the number of incoming electrons is not infinite, there is a limit on detecting a specific element in a matrix. This limit is usually described via the use of an SNR which defines when the edge is statistically significant. A common definition for a statistically significant signal is when the signal has a value of SNR

larger than three. Because the electron detection is fundamentally a Poisson process, the noise can be described by the square root of the detected signal which is the sum of $N_{e,e}$ and $N_{e,b}$, using Eq. 2.16 and Eq 2.17 the gives following result [86]:

$$SNR_e = \frac{N_{e,e}}{\sqrt{N_{e,e} + N_{e,b}}} = \frac{C \cdot \sigma(\beta, \Delta)}{\sqrt{C \cdot \sigma(\beta, \Delta) + B_e}} \sqrt{\epsilon_e I t} \tag{2.19}$$

From Eq. 2.19 it is clear that SNR goes as the square root of I and t hence if one want to detect a small edge, extending the acquisition time or increasing the current are viable methods to make the signal appear out of the noise. The dependence of SNR with acquisition time is visualized in Fig. 2.8 where snapshots at different acquisition times are shown from the same EEL spectrum as in Fig. 2.7. At short acquisition times, the noise dominates the spectrum and the edges are not observable indicating the SNR is small. However at longer times, the edges start appearing out of the noise making it possible to identify them. In the spectrum at 10 ms, the Nd M_{45} edge becomes identifiable whereas the Ni L_{23} edge is still buried in the noise which is simply due to the fact that more electrons undergo scattering on the Nd M_{45} edge than on the Ni L_{23} edge. Note that the definition of SNR does not take the detector response (DQE) and uncertainty from the background fit into account hence, Eq. 2.19 is an upper limit on the best SNR possible when having a perfect detector and background subtraction method.

2.3. Energy Dispersive X-ray Spectroscopy

Energy dispersive x-ray spectroscopy (EDX) measures the energy spectrum of the x-rays present in the electron microscope. As discussed in *Section 1.1.3*, two main types of interactions create x-rays when a highly energetic electron interacts with material. The characteristic x-rays give information on the chemical content in the material. Similar to EELS, EDX mapping can be performed by scanning a condensed probe over the specimen and acquiring an x-ray energy spectrum at every probe position enabling elemental quantification ranging from micrometer to angstrom resolution. In contrast to the EELS setup, no complicated electron optical elements are needed to measure the energy spectrum of the x-rays where for EDX only a detector is

needed. The x-ray detectors are placed as close to the specimen as possible to maximize the collection efficiency. Recent setups describe a coverage of 1 sr which would correspond to a collection efficiency of ~8%. Knowing that not every inelastic electron produces an x-ray, which is described by the fluorescence yield, the count rate of EDX is rather low compared to EELS. However, compared to EELS, EDX does not have the presence of the large background signal where the background signal in EDX mainly arises from Bremsstrahlung radiation which is relatively small for thin samples.

2.3.1. The X-ray Energy Spectrum

As discussed in *Section 1.1.3*, the generated x-rays due to the interaction with a fast electron are the Bremsstrahlung and characteristic x-rays. However, additional signals are measured with the x-ray detectors and it is important to identify them since they can change the interpretation of the x-ray spectrum [19].

- Pulse pile-up peaks occur when two x-rays are detected as one in the pulse processor circuit. This happens when the two x-rays are arriving in the detector at almost the same time where the energy of the peak is given by the sum of the two x-rays. The number of pulse pile-up events depends on the count rate and processing time of the incoming x-ray signal.

- Escape peaks arise in the spectrum when the incoming x-ray interacts with the material of the detector via the ionization of an inner-shell which can then decay via x-ray emission. If this x-ray escapes the detector, this energy will not be measured hence an escape peak is expected at an energy which is equal to the incoming x-ray energy minus the energy of the outgoing created x-ray which for an SDD is the K_α line of Si (1.839 keV).

- Compton scattering can occur between the atoms in the detector and incoming x-rays. The incoming x-ray then scatters with an electron where another x-ray of less energy gets created. If this x-ray can escape the detector, this energy is lost. Compared to the

escape peak, this will give a more broad spectrum and fortunately, the cross section for this process is very low compared to the photoelectric absorption.

- System x-rays originate as a secondary process where created x-rays interact with the material inside the column (grid, objective lens, holder, *etc.*) which can again create x-rays. For instance, x-rays originating from copper is almost always present since the majority of grids are made from copper.

Hence when interpreting the x-ray spectrum and quantifying the chemical content one should always be careful for the presence of these spurious x-ray signals since they can significantly modify the results.

2.3.2. Quantitative EDX

The main aim for EDX is to obtain knowledge on the chemical composition of the specimen hence the interest is in the characteristic x-rays. The other signals in the x-ray spectrum originating from other processes are of less concern to us and will be regarded as background signal. Therefore, it is important to disentangle the characteristic x-ray signal from the background. Contrary to EELS, this background does not have a power-law shape but exists out of a weakly varying signal arising from Bremsstrahlung and the overlap of x-ray lines due to the poor energy resolution (~100 eV) of the x-ray detection. The easiest method to remove the weakly varying background underneath an x-ray line is by linear fitting the background underneath the peak where the fitting window is chosen before and after the x-ray line. When multiple peaks are overlapping, these can be disentangled using a deconvolution method [20, 96, 97]. However caution is warranted when applying these methods since artefacts can arise [97]. Once the number of characteristic x-rays are determined, the quantitative analysis can be performed.

The theoretical number of counts for a given characteristic x-ray ($N_{x,e}$) is given by the probability that an incoming electron interacts inelastically with the given inner-shell and that the core hole is created via the emission of an x-ray which is given by the fluorescence yield

(ω) [98]:

$$N_{x,e} = C \cdot \sigma_T \cdot \omega \cdot \epsilon_x \cdot It \tag{2.20}$$

where C is the areal density, σ_T is the total cross section of the inelastic scattering and ϵ_x is collection efficiency which consists out of the geometric solid angle as well as the energy dependence of the x-ray detection efficiency. Eq 2.20 is only an approximation since it does not take absorption and fluorescence into account. Absorption occurs due to the finite extent of the specimen where the created x-ray is again absorbed by the specimen, hence these x-ray counts are lost and an underestimate of $N_{x,e}$ is obtained. The absorption cross section depends on the thickness, x-ray energy, and elements in the specimen and models have been described to take this into account [99–101]. Fluorescence occurs when the absorbed x-ray creates another x-ray having a different energy than the initial x-ray. The energy of the outgoing x-ray should always be lower or equal to the initial x-ray energy due to conservation of energy. Compared to absorption, this effect is minor and usually not taken care of in the quantification.

Similar to EELS, the number of background counts ($N_{x,b}$) is given by:

$$N_{x,b} = B_x \cdot \epsilon_x It \tag{2.21}$$

where B_x is the background cross section which includes all unwanted signals in the x-ray energy spectrum. This consists out of a broad continuum spectrum arising from the Bremsstrahlung and the other x-ray peaks which are of no concern.

Via the determination of $N_{x,e}$, the ratio between the areal density of two elements can be obtained using the following equation:

$$\frac{C_A}{C_B} = \frac{\sigma_{T,B} \cdot \omega_B}{\sigma_{T,A} \cdot \omega_A} \frac{N_{x,e}(A)}{N_{x,e}(B)} = k_{AB} \frac{N_{x,e}(A)}{N_{x,e}(B)} \tag{2.22}$$

where k_{AB} is known as the Cliff-Lorimer k-factor [102]. In Eq. 2.22 it is approximated that the collection efficiency is independent on the x-ray energy which holds for x-rays between 1 and 10 keV. The dependence of the efficiency as a function of energy can be incorporated into Eq 2.22 where usually the dependence should be determined experimentally. Due to the

incomplete knowledge of the specimen, the theoretical k-factors present large uncertainties. Therefore, they are frequently determined by using specimens from which the chemical content is know beforehand and then applied to unknown specimens [20].

Due to the relatively low count rates and limited acquisition times in EDX, counting noise will always be dominantly present in the x-ray spectrum and a SNR can be defined to describe how significant the detected signal is. Similar to EELS (see Eq 2.19), the noise can be described by the square root of the detected signal where it is implied that the background subtraction does not add any uncertainty to the measurement. Using the same definition as Eq 2.19 gives:

$$SNR_x = \frac{N_{x,e}}{\sqrt{N_{x,e} + N_{x,b}}} = \frac{C \cdot \sigma_T \omega}{\sqrt{C \cdot \sigma_T \omega + B_x}} \sqrt{\epsilon_x I t} \tag{2.23}$$

The SNR defined for EELS (Eq. 2.19) and EDX (Eq. 2.23) can be used to get an estimate on which method would be better to measure a particular element. From the equation it is seen that the background signal has a significant contribution to the SNR which in general is larger for EELS than for EDX. However, for EDX there is the fluorescence yield which is small for low Z materials (<5%) and the collection efficiency of EDX is only ~5% where it is 20-50% for EELS. Therefore the EELS method mostly is better for low Z materials such as carbon and oxygen whereas EDX outperforms EELS for the high Z materials such as gold and silver. Furthermore, for thicker specimens, multiple scattering broadens the edges of EELS making it harder to distinguish the edge from the background making it that EDX performs better for thicker specimens since this type of broadening does not occur for EDX [80].

3. 4D STEM-in-SEM

This chapter is based on:

A. Orekhov, D. Jannis, N. Gauquelin, G. Guzzinati, A. Nalin Mehta, S. Psilodimitrakopoulos, L. Mouchliadis, P. K. Sahoo, I. Paradisanos, A.C. Ferrari, G. Kioseoglou, E. Stratakis, J. Verbeeck, *Wide field of view crystal orientation mapping of layered materials*, (2021) *(Under review in ACS Applied Materials & Interfaces)*

3.1. Introduction

Layered materials (LMs) such as graphene and transition metal dichalcogenides (TMDs) have gained a lot of interest and are promising for the future of functional materials due to their unique mechanical, chemical and electrical properties [103]. It is known that the structure of the LMs can affect the properties to a great extent. For instance, the grain boundaries influence the mechanical properties [104–106], electrical properties [107, 108] and thermal conductivity [109, 110]. The twist angle for multilayer (ML) systems is an important parameter for the electric properties. For instance, for graphene at a magical angle, the system becomes a superconductor [111]. Furthermore, the electronic and optical properties of LMs hybrid systems depend on the stacking type of the layers [112–114]. For hexagonal 2D materials, such as graphene and MoS_2, two sheets can be stacked on top of each other in two configurations AA or AB. For AB stacking, half of the atoms lie directly over the centre of a hexagon in the other sheet and the other half lies over an atom. For AA stacking, the layers are exactly aligned.

Since these structural parameter are of such importance, there is a need for fast and large-scale structural characterization. Raman spectroscopy is a popular method which probes the electronic and vibrational properties and links these to the structure such as orientation, strain and number of layers [115–117]. The advantage of Raman is that it is non-invasive and large areas are easily investigated. In order to probe graphene or other 2D materials on the atomic scale, scanning probe microscopy (SPM) [118, 119] or TEM [120–122] is often used. Both techniques resolve the individual atoms in real space but suffer from small fields of view (<100 nm^2). In selected area electron diffraction and dark field TEM a slightly larger field of view is offered while losing the atomic contrast [123–125]. SEMs on the other hand, are able to retrieve nanometer resolution while being able to scan large fields of view and they typically use electron beam energies from 0.5 to 30 keV, which are considerably lower than the typical 60-300 keV used in TEM. For 2D materials, the increased interaction strength at lower beam energies results in more scattering, hence, increasing the contrast for thin low Z materials such as graphene [126–128]. The downside of the increased interaction strength is that the incoming electron beam can also

induce more beam damage. Compared to TEM, operation of a SEM is easier as no elaborate alignment procedure is required making it easier to fully automate the data acquisition process. Furthermore, there is a larger working volume inside the SEM vacuum chamber which offers much needed space for new experimental setups. Due to these advantages compared to TEM instruments, interest has been emerging in using an SEM in transmission mode by inserting a detector for transmitted electrons underneath the specimen [129–134]. Furthermore, the hybrid pixelated detectors seem to be an optimal candidate due to their capability to detect single electrons, no dark noise, high frame rates, beam hardness and large dynamic range.

In this chapter, we present a setup based on a modest SEM in which we integrate a hybrid pixel detector. The detector is placed in the far field below the specimen and records a diffraction pattern for each position the electron probe visits on the specimen. These diffraction patterns contain a wealth of structural information while the spatial resolution is determined by the size of the incoming electron probe. Such a setup is known in the TEM community as 4D STEM, and we will show that transposing it to SEM offers attractive advantages for the study of LMs over large fields of view. We show that different types of local structure information can be extracted, ranging from orientation of grains, to detection of twisted layers, unit cell deformation and stacking of ML systems.

3.2. Experimental Setup

A standard JEOL JSM 5510 SEM with a tungsten electron source was selected to perform the 4D STEM in SEM experiments. This is a very common SEM which is perfect for a proof of principle. A Thorlabs 30 mm optical cage (see Fig. 3.1(b)) was used to mount the specimen on top. This cage gave the freedom to vary the distance between the specimen and the detector (5-50 mm)) which is known as the camera length. The diffraction pattern acquisition is performed using an Advacam®MiniPix detector with a 300 μm Si active layer. This is a 256×256 hybrid pixel detector based on a Timepix1 chip, integrated with its readout electronics in a USB stick format. In combination with the fixed 55 μm pixel size of the detector, this results in a minimum

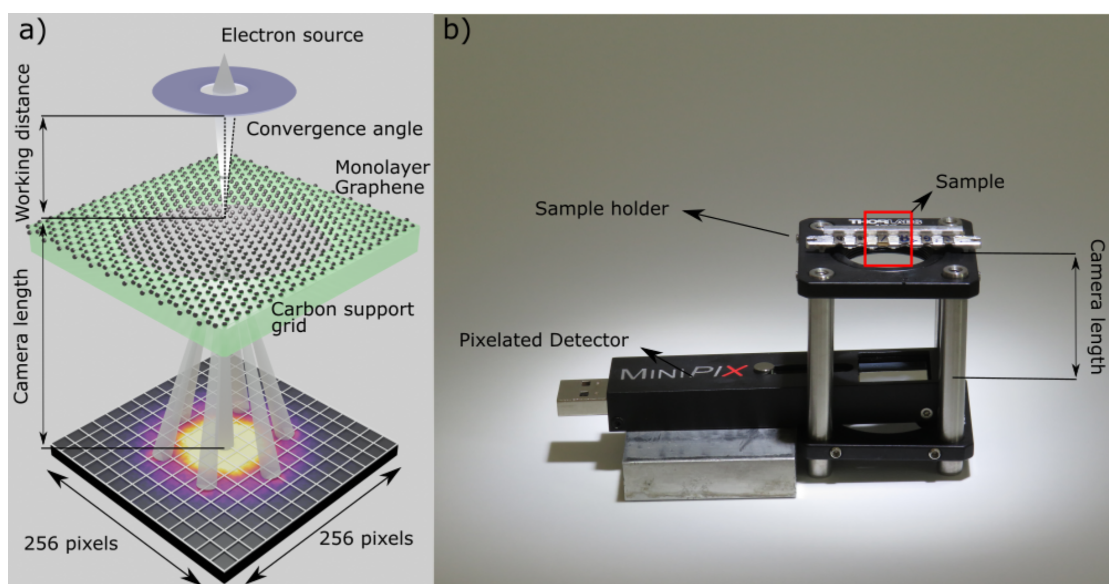

Figure 3.1.: **(a)** Schematic drawing of the experimental setup, where the sample consists out of a monolayer graphene on top of a holey carbon support grid. **(b)** Picture of the setup, the sample mount allows camera length adjustment.

resolvable angle ~1.1 mrad. For an electron beam of 20 keV, this corresponds to a reciprocal resolution of 1/7 nm^{-1}. The scan coils are controlled using a custom scan engine [135], which allows for synchronization between the detector readout and the probe position. Since no trigger signal is available for the detector, the synchronization between the probe and the camera is done via software which gives overhead on the scan speed. Although, since the dead time of the camera is 20 ms, the overhead due to the software triggering is minor. In Fig. 3.1, the schematic and real setup which is used inside the SEM is shown where the different parameters are indicated.

The spatial resolution of the incoming probe was estimated from a 4D STEM in SEM experiment where the LM, in this case MOCVD 1L-MoS_2, had a hole. This hole is sharp since

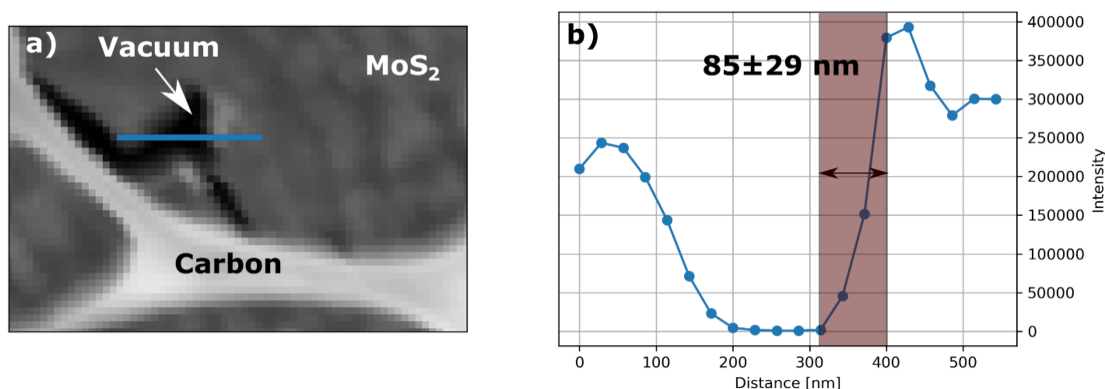

Figure 3.2.: **(a)** Magnified VDF area of MOCVD-1L-MoS_2 film. **(b)** Line profile across the hole (vacuum) in MOCVD-1L-MoS_2. The sharp edge is used to estimate the probe size.

the material is only one layer thick and is used to get an estimate of the spatial resolution. In Fig.3.2(a), a magnified virtual dark field (VDF) map of 1L-MoS_2 is shown where the crack is indicated. The spatial resolution is estimated from the line profile shown in Fig. 3.2(b) which is ~85 nm. This is a rather poor resolution for a typical SEM but for the experiments we performed this was sufficient since we had no interest in higher resolution scans. The improvement of the spatial resolution can easily be done by placing the compact setup into a more advanced SEM. Another method to increase the spatial resolution would be to increase the convergence angle which is done by decreasing the working distance. This would result in a diffraction pattern where the diffraction spots would increase in radius, hence the accuracy and precision on the disc position would deteriorate.

3.3. Materials

As a showcase for the developed technique, four types of representative LMs are used.

- Commercial single layer graphene (SLG) and bilayer graphene (BLG) which are suspended

on TEM grids from Graphenea [136]

- Commercial graphene oxide (GO) is sourced from Sigma-Aldrich (763705-25ML). A GO and H_2O is centrifuged and drop-cast onto a quantifoil TEM grid with amorphous carbon [137].

- 1L-MoS_2 is grown by metal organic chemical vapor deposition (MOCVD) on sapphire [138], then transferred on a TEM grid via ultrasonic delamination, using polymethyl methacrylate (PMMA) as a support layer [139].

- 2L-MoS_2 flakes with AB stacking are prepared on SiO_2/Si via chemical vapor deposition (CVD), and wet-transferred using PMMA followed by a controlled lift off process onto TEM grids [140–142].

3.4. Data Analysis

The amount of data generated during typical 4D STEM scans is minimally 8 GB for the 256×256 probe positions and 128 GB for the larger scans using the 1024×1024. For this reason, special algorithms need to be developed which are able to handle such large sizes of datasets. The algorithms used in this work are implemented in the open-source Pixstem and Pyxem library [48, 49] and the full data treatment can be found on the Zenodo repository [143].

3.4.1. Central Beam Shift

The first step in the data analysis is finding the coordinate of the central beam. Since the probe is scanned over the specimen, the diffraction pattern will be translated over the detector if the FOV scanned is larger than the pixel size of the detector which was 55 μm for this experiment. One method to get an accurate measurement of this translation is to perform a scan in a vacuum where the position of the central beam can be easily tracked. The position of the central beam is used to measure the relative translation between the patterns. However, due

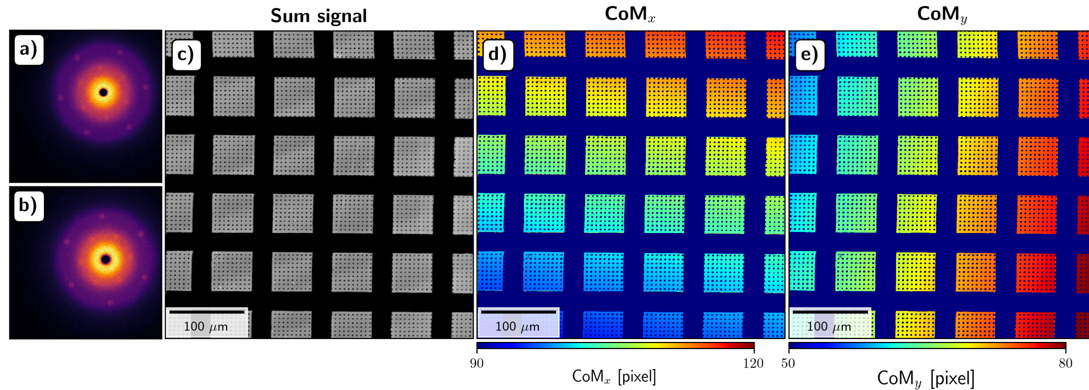

Figure 3.3.: **(a,b)** Two measured diffraction patterns from a different probe position from which the translation of the central beam is apparent. Due to the large current at the central beam, no intensity is measured. **(c)** The sum signal of the scan where the small holes indicate the presence of free standing graphene. **(d,e)** The x and y-component of the first moment where the linear dependence on the probe position is clearly visible. Only the diffraction patterns, where there is both graphene and amorphous carbon, are used for the fit since due to the edges of the holes, the first moment of these diffraction patterns do not represent the shift of the diffraction pattern.

to the large acquisition time (12 hours for 1024×1024), this is not the most attractive method. Another approach would be to track the central beam but, since the incoming current used in the experiment is too high for the detector to handle at the central beam, almost no signal is detected in this area making it hard to track this feature in the image. This is shown in Fig. 3.3(a,b) where two diffractions from distant probe positions are shown where the central beam is dark indicating the lack of intensity. The reason for this non-linear response at high current is that there is pulse pile up, such as in the x-ray detectors, because the electrons arrive to fast after each other.

In this work, the translation is determined by calculating the first moment for every probe

position. Since the shift is expected to behave linear as a function of probe position, the x and y-components of the first moment are fitted to a linear plane to reduce the noise arising from the individual diffraction patterns. In Fig. 3.3(d,e), the x and y component of first moment is shown for a 1024×1024 scan on a graphene sample with a FOV of $0.5\ \mathrm{mm}^2$. The fitted values are used to estimate the position of the central beam and to align the central beam for every probe position. Only the diffraction patterns, where there is both graphene and amorphous carbon, are used for the fit since, due to the edges of the holes, the first moment of these diffraction patterns do not represent the translation of the diffraction pattern. This shift determination is needed for the background subtraction where the centre of the diffraction pattern should be known to remove the signal arising from the inelastic and amorphous scattering. Another reason for knowing the central beam position is that the placement of a virtual detectors gives contrast from the specimen and not from the translation of the diffraction pattern which does not give any information about the specimen. Note that this method for finding the central beam is not universal and for other specimens, other types of algorithms should be used to get the coordinate of the central beam.

3.4.2. Background Subtraction

Fig. 3.4 shows diffraction patterns of SLG/BLG using electrons of 20 keV recorded at a camera length of 35 mm. Fig. 3.4(a,b) show the diffraction pattern of SLG supported by a holey carbon membrane and over a freestanding hole. The pattern originating from the substrate supported area shows a larger background signal stemming from diffraction on the amorphous carbon substrate. Although, even for the freestanding SLG, a smaller amount of isotropic background is observed which arises from the inelastic scattering, contamination and/or defects. The diffraction patterns in Fig. 3.4(c, d) both have twelve diffraction spots whereas the intensity in (d) is around halve the intensity of (b), hence this is a grain boundary, where due to the finite extent of the incoming electron probe, a diffraction pattern is obtained from the overlap region. The diffraction pattern in (c) is freestanding BLG since the intensity of the spots are similar to (b),

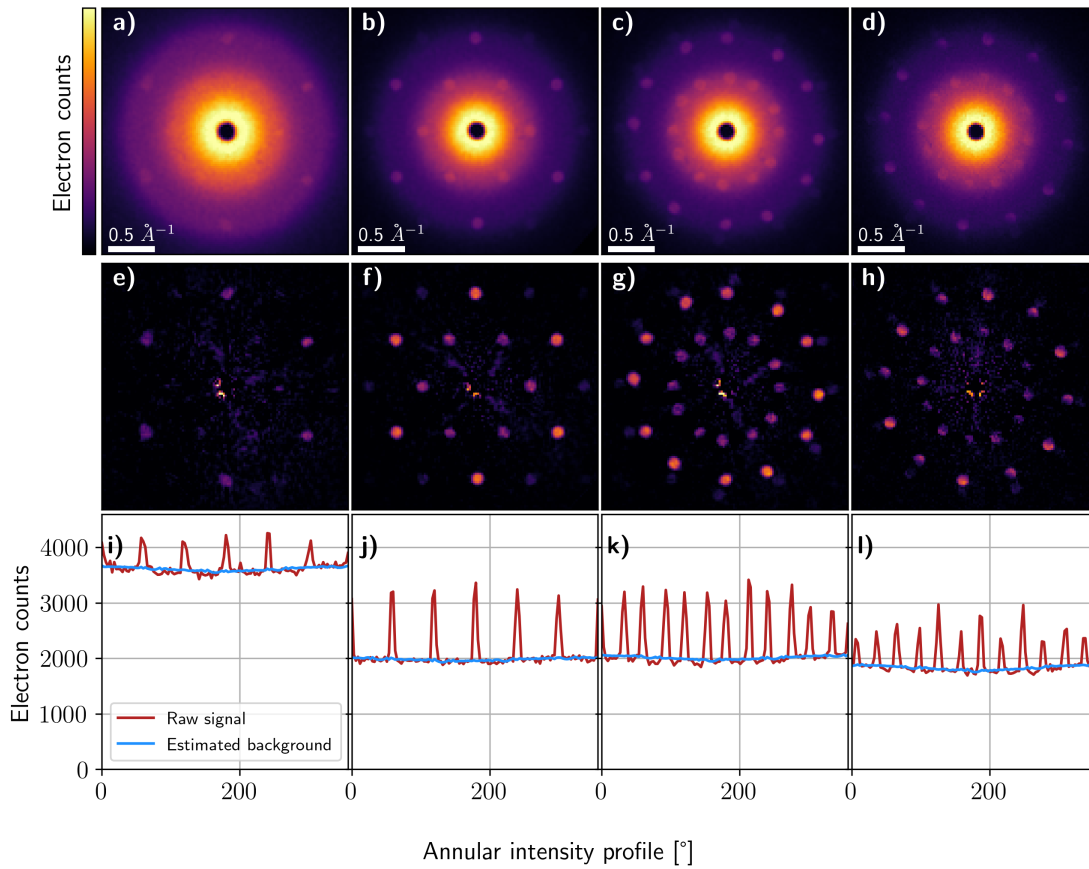

Figure 3.4.: **(a-d)** Experimental diffraction patterns of SLG and BLG where (a) is SLG on substrate, (b) free standing SLG, (c) BLG, and (f) free standing SLG at grain boundary. **(e-h)** The background-subtracted diffraction patterns using the radial median method. **(i-l)** Annular intensity profile of the second order spots for the corresponding diffraction patterns (red). The estimated background signal from the radial median is also shown.

in *Section 3.5.4* simulations are performed to confirm this statement.

From all these patterns, it is noticeable that the background signal is isotropic, therefore this background can be removed by calculating the azimuthal median for all radii. The median is used instead of the average since the median is less affected by the outlier pixel values. Additionally, another more general method using the median kernel filter to remove the background was performed but it was observed that the azimuthal median method outperformed this method. Since the azimuthal median is taken, it is important to know the centre of each diffraction pattern. Fig. 3.4(e-h) shows the background-subtracted diffraction pattern where only the sparse diffraction spots remain. To investigate if the radial median method is able to correctly identify the background signal, the annular intensity profiles for all four diffraction patterns are shown in Fig. 3.4(i-l) where the intensity of the second order spots are shown. The estimated background from the radial median method is shown in blue and it is seen that it is able to correctly identify the background signal. Note that this works since the diffraction pattern arising from the graphene is sparse whereas if the convergence angle would increase and the diffraction spots would become larger, this method would overestimate the background.

3.4.3. Peak Finding

The next step in the data analysis is the determination of the peak positions. Multiple algorithms have been developed to get an accurate measure of the peak positions in NBED [61–64]. In this work, the phase correlation method [144] was used where a template disc, with the same radius as the convergence angle, is phase correlated with the measured diffraction patterns where the phase correlation (Pc) between two images a and b is defined as follows:

$$Pc = \mathcal{F}^{-1}\left\{ \frac{\mathcal{F}(a) \cdot \mathcal{F}(b)^*}{|\mathcal{F}(a) \cdot \mathcal{F}(b)^*|} \right\} \tag{3.1}$$

This method is frequently used to determine the translation between two images. This occurs in electron microscopy when multiple images are acquired with a shift between them due to the instabilities of the microscope [145]. Hence, by phase correlating the disc with the diffraction

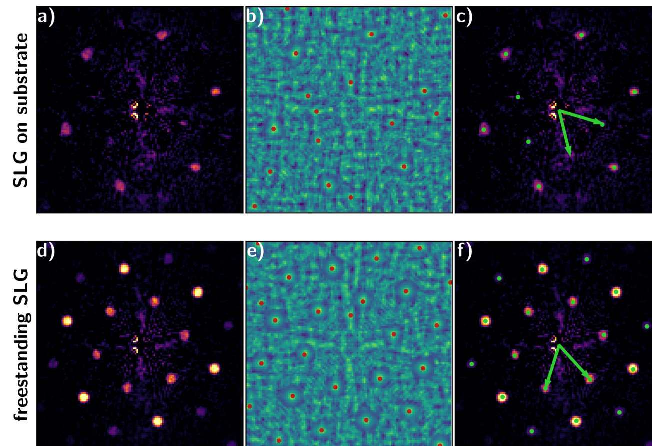

Figure 3.5.: **(a,d)** The background-subtracted diffraction patterns on the substrate (a) and freestanding (d) SLG. **(b,e)** The resulting phase correlation map with the template disc where the result of the blob dog peak finding algorithm is shown. **(c,f)** The resulting peaks after filtering where the fitted basis vector is shown (blue).

pattern, the position of the disc features will have a local maximum in the phase correlated image. Compared to the cross correlation, the phase correlation makes it so the low intensity diffraction spots have a similar intensity in the phase correlated image making it easier to detect these low intensity spots. In Fig. 3.5 (a,d) two examples of background-subtracted diffraction patterns are shown where the aim is to find the peak positions. The phase correlation using a template disc with a radius of three pixels is shown in Fig. 3.5(b,e). The peak positions are determined from the phase correlated image via the use of a local maximum peak finding algorithm where the found peaks are shown in Fig. 3.5(b,e). It is clear that the freestanding SLG has a higher signal-to-background, hence the peak fitting procedure will be more precise compared to the SLG on the substrate where even the first order spots are not always detectable. Several parameters, such as a threshold value, can be tweaked to optimize the peak finding where it is chosen to overestimate the number peaks and to filter them afterwards. The filtering

is performed by selecting the highest intense spots, and use this to get a first set of basis vectors. The next step is to calculate the guessed positions from these basis vectors and, if the detected peak is not within the proximity of the guessed peak, then it will be discarded. This proximity parameter is defined by the user and a value of 10 pixels was used in this analysis. The final result is shown Fig. 3.5(c,f), where the resulting peaks and the final fit of the basis vectors are shown. As described in *Section 2.1.1*, the method to get the strain and orientation can be derived from the basis vectors.

3.4.4. Orientation, Strain and Diffraction Spot Intensity Mapping

From the 4D STEM dataset, multiple different types of information can be obtained. As a showcase for these different types of signals, a 512 × 512 scan with a dwell time of ~40 ms was performed on the commerical SLG sample which consists out of SLG and BLG on top of a carbon quantifoil with a periodic set of holes. In Fig. 3.6(a), the VDF image is shown where the inset shows the virtual detector configuration. The virtual detector is chosen such that the contrast in the image depends on the thickness from which the freestanding holes and empty holes are clearly identifiable.

Another type of signal is the orientation map (see Fig. 3.6(b)) which is determined using the approach from *Section 2.1.1*, where the fitted basis vectors are used to determine the orientation. Even when the SLG is on the substrate, due to the peak finding method, the orientation of the SLG can still be determined where the precision will be smaller due to the lower signal-to-background. The orientation map will be used to extract the grain boundaries, the angle between the adjacent grains and the shape of the individual grains.

The strain map can be reconstructed where the unit cell expansion ($\epsilon_{u.c.}$), which describes expansion or reduction on the area of the unit cell, is shown in Fig. 3.6(c) . The area of the unit cell is calculated by performing the cross product between the two basis vectors. From Fig. 3.6(c), it seems that there is a small increase of the unit cell for the freestanding holes which could be attributed by the sagging of the freestanding SLG [146]. However, further investigation

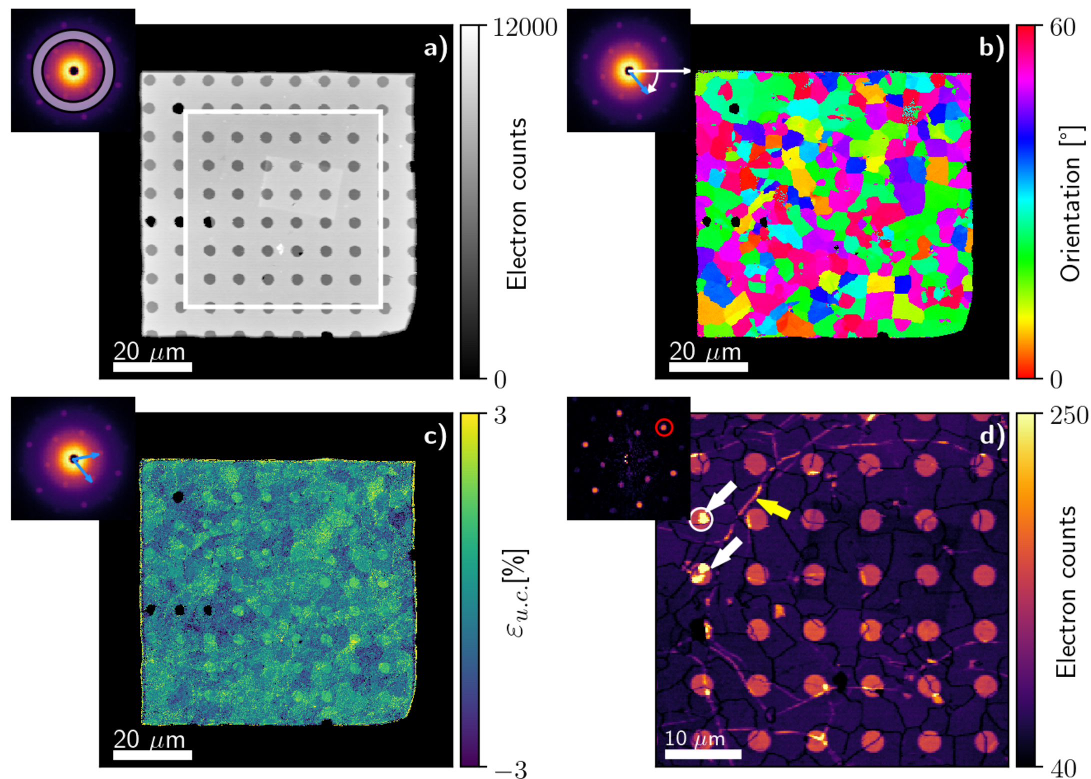

Figure 3.6.: A scan of 512 × 512 probe positions with a dwell time of ~40 ms is obtained from the SLG sample on a carbon quantifoil with a periodic set of holes. **(a)** a VDF image obtained from applying a virtually defined detector area, shown as inset.**(b)** Orientation mapping showing grain boundaries and mean orientation of each grain also in the areas where the support grid is present. **(c)** $\epsilon_{u.c.}$ unit cell expansion compared to the average unit cell across the entire FOV. ~0.5% positive strain is seen in the holes, indicating an increase of unit cell area. **(d)** VDF image of central area indicated by a white rectangle in (a), calculated based on the intensity of the brightest second order spots of the background subtracted diffraction patterns (see inset) showing a mixed contrast due to grain boundaries (lower intensity lines have the same contours from (b)), wrinkles (yellow arrow) and multiple layers (white arrows).

should be performed to confirm these results.

Not only do the position of the spots hold structural information, the intensity of the diffraction spots also give information about the local structure of the specimen. In Fig. 3.6(d), a map is constructed where for every probe position the intensity of the most intense second order spot, from the background-subtracted diffraction pattern, is shown. Over the entire map, dark lines are visible which indicates the presence of grain boundaries. The reason for this is seen in Fig. 3.4(d), where the intensity of the diffraction spots decreases since two different grains are probed at the same time. The increase of intensity at the two white arrows of Fig. 3.6(d) indicates the presence of BLG, which are stacked on top of each other where in *Section 3.5.4*, the type of stacking AA or AB is determined. The intense lines indicated by the blue arrow arise from wrinkles in the graphene sheet where, due to the folding, more material is present which increases the signal in Fig. 3.6(d). Lastly, it is clearly seen that the most intense beam of the second order spots for the freestanding SLG is noticeably larger than on the substrate. If the incoming electron beam would scatter kinematically (one time), there should be no such distinction between the diffraction patterns on the substrate and freestanding. However, this behaviour indicates the multiple scattering of the incoming electron beam where the scattering with the amorphous carbon substrate removes intensity from the diffraction spots.

3.4.5. Grain Analysis

From the 4D STEM experiments, the orientation map can be calculated. From the orientation map information about the grain boundaries, shape of the grains, angle between adjacent grains, *etc.* can be determined. The first step, to go from orientation map to grains, is to apply a Sobel filter [147] to the orientation map which enhances its edges. The next step is applying a threshold to give the edges equal weight. The value of the threshold determines which the minimal grain mismatch angle is where a proper choice can be made depending on the precision of the orientation mapping. This image is put into the watershed segmentation algorithm [148] implemented by the open-source scikit-image python library. From the resulting segmented

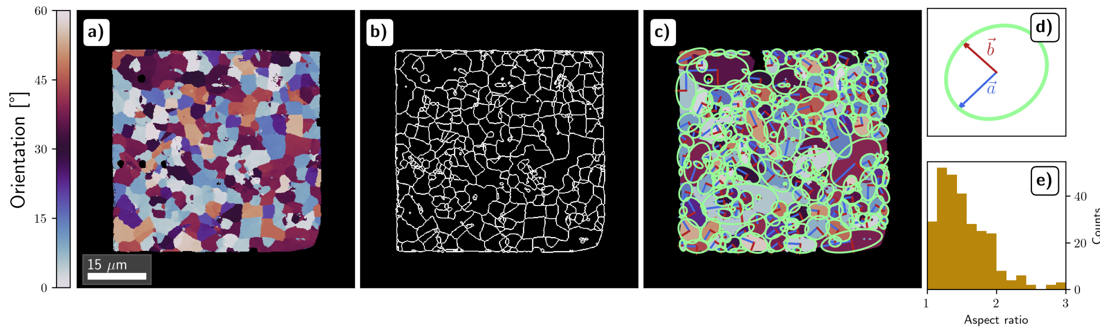

Figure 3.7.: **(a)** The orientation map obtained from the same 512 × 512 scan on SLG. **(b)** The boundaries of the segmented grains using the watershed algorithm. **(c)** The fitted ellipses for every grain where the principal axes of the ellipses are shown. **(d)** Schematic view of one ellipse with the two principal axes indicated. **(e)** Histogram of aspect ratios showing that the grain shape is not spherical on average.

image, the average orientation per grain can be calculated. In Fig. 3.7(a), the orientation map of the same 512 × 512 scan as in Fig. 3.6 is shown. The boundaries of the segmented image, using the algorithm described previously, is shown in Fig. 3.7(b). Once, the grains are identified multiple types of analysis can be performed on them. Here, one possibility is shown which is fitting the grain boundaries to ellipses using the least squares method where the fit is shown in Fig. 3.7(c). An histogram from the aspect ratio of the ellipses (see Fig. 3.7(e)) is created showing that the average grain shape is not spherical.

3.4.6. Dose Dependency Orientation Mapping

To have an estimate on the precision and accuracy of the method used to determine the orientation, a SLG with the same acceleration voltage (20 keV), camera length (33 mm) and convergence angle (3.5 mrad) is used for the experiment is simulated. In the simulation only elastic scattering is taken into account whereas the inelastic part is neglected to simplify the calculations. From

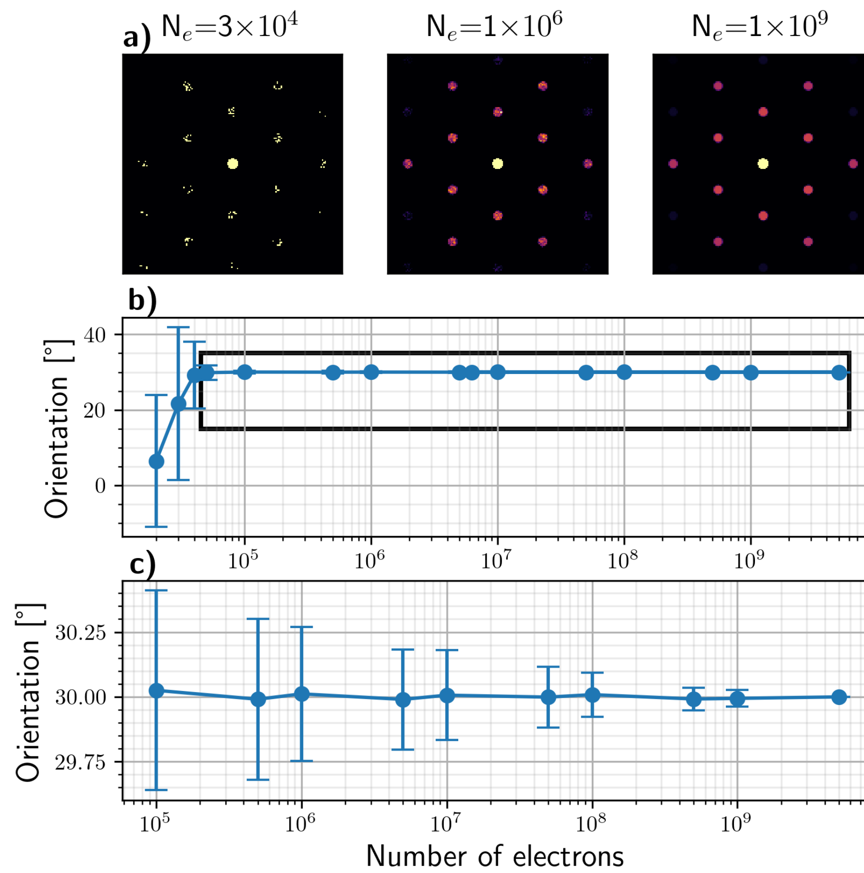

Figure 3.8.: **a)** Three different diffraction patterns of SLG with different amounts of dose where only Poisson noise is added. **(b)** The average and standard deviation at different doses where for each dose 500 different realizations were made. **(c)** Zoomed in on the black rectangle shown in (b).

Ref. [88], we expect an 'ideal' detector, but with a ~20% loss of incoming electrons. In Fig. 3.8(a), three representations of the simulated patterns, each having a different total amount of dose (N_e), are shown. We apply the same orientation mapping algorithm, and determine that 10^5 electrons are required to obtain 1° precision in orientation determination (see Fig. 3.8(b,c)). To obtain a value of the precision, 500 different realizations are made at every dose and each time the orientation is determined from which the precision is given by the standard deviation. Neglecting inelastic scattering, and potentially overestimating the DQE might deteriorate the precision, but not change the order of magnitude [80]. The precision on the experimental data is determined by calculating the standard deviation on the orientation inside one grain. The experimental 0.23° well compares to the simulated 0.19°. This shows that, for the same beam current, the acquisition speed could be increased by up to a factor of 100 with an upgraded camera system, while still maintaining rotation precision of ~0.5°.

3.5. Results

3.5.1. Orientation Mapping in SLG

To demonstrate the ranges in the FOV applicable using the new developed method, four maps at different magnification centered around the same location were performed. The magnification of the scan decreased from 9000× to 300×, which translates into scanned areas from 100 to 50000 μm^2. In Fig. 3.9(a-d), the four processed grain maps are shown. The grains are identified using the methodology explained in *Section 3.4.5* where a mismatch of 2° is defined as a grain boundary in order to stay well above the noise level of the orientation determination step. From this segmented data, a rich variety of information is obtained, such as mean orientation, grain size, average grain shape, grain boundaries, etc. In Fig. 3.9(a-c), the corresponding areas (inside a white rectangle) are identified, demonstrating negligible beam damage from the consecutive scans. The ability to scan from nm-scale to mm-scale could lead to automated scans of wafer size areas, while only spending time on the interesting regions, as long as a reasonable indicator

for “interesting” can be formulated.

In order to achieve a mm-scale FOV, but have spatial resolution able to resolve μm size grains of a polycrystalline sample, a 1024×1024 probe position scan is performed at $250\times$ magnification (see Fig. 3.10(a)). The number of different grains identified at this magnification is ~4200 over 0.168 mm^2. This gives access to unprecedented statistics on structural information, missing in the common tens μm^2 fields of view TEM investigations [20]. Fig. 3.10(b) plots the grain size distribution. The average grain size is ~42 μm and the 50th percentile is ~22 μm^2. The maximum detected grain size is ~192 μm^2 (white square in Fig. 3.10(a)). As an example of mining this rich data, a correlation between grain size and orientation can be extracted by classifying these in three categories, corresponding to small ~0.6-13 μm^2, medium ~13-32 μm^2, and large ~32-192 μm^2 grains. These intervals are chosen to show the evolution of different parameters with grain size. For large grains, we detect two preferential orientations, 30°apart from each other. Fig. 3.10(c) plots the distribution of the three size classes. The solid lines are the result of fitting the distribution to the sum of two Gaussians and an offset. With increasing grain size, the orientations of the grains are progressively taking two preferential directions (22°and 52°)[1] seen by the increasing amplitude of the Gaussian peaks compared to the constant background. Another correlation is between grain size and number of adjacent grains, as more adjacent grains are expected around larger grains. Fig. 3.10(d) plots the histograms corresponding to the different size categories. A correlation is observed, as the average number of surrounding grains is 3.29, 4.55, 7.39. The shape anisotropy of each grain can be determined by fitting its boundaries to an ellipse and taking the aspect ratio of its principal axes. Fig. 3.10(e) plots the aspect ratio for different grain sizes, where the distribution changes with grain size. The solid line is a skewnormal fit from which the mean value of the aspect ratio is 1.31, 1.39,1.46, indicating that larger grains are less spherical than smaller ones.

[1]The zero angle is defined with respect to the x-axis of the detector.

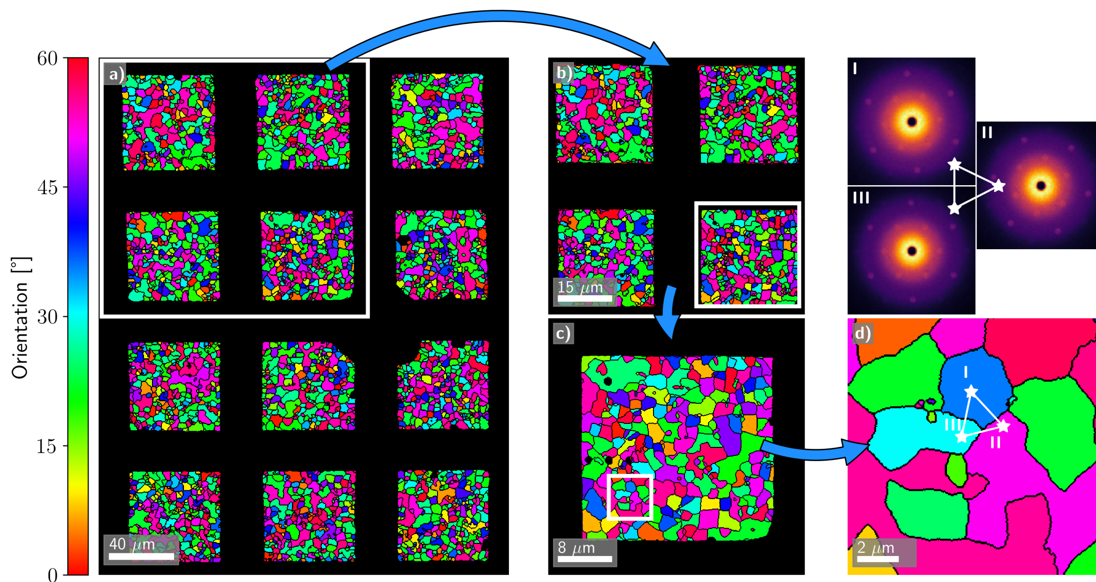

Figure 3.9.: Orientation mapping of a SLG over a wide range of fields of view: from mm-scale (250× magnification) to nm-scale (9000×). **(a-d)** Orientation maps at different magnifications of the same area of the sample, showing no noticeable beam damage. (a) 50000 μm^2 FOV (300× magnification). **(b)** Zoom on the 4 squares at the top left of (a) scanned with 512x512 probe positions. **(c)** Zoom on the bottom right square of (b) using a 512x512 scan raster, corresponding to a FOV 3600 μm^2. (d) High magnification scan (9000×) with a raster of 256 × 256 probe positions over 100 μm^2, corresponding to the area indicated with a white square in panel (c). **(I-III)** Three diffraction patterns from adjacent grains identified by the same indices in panel (d).

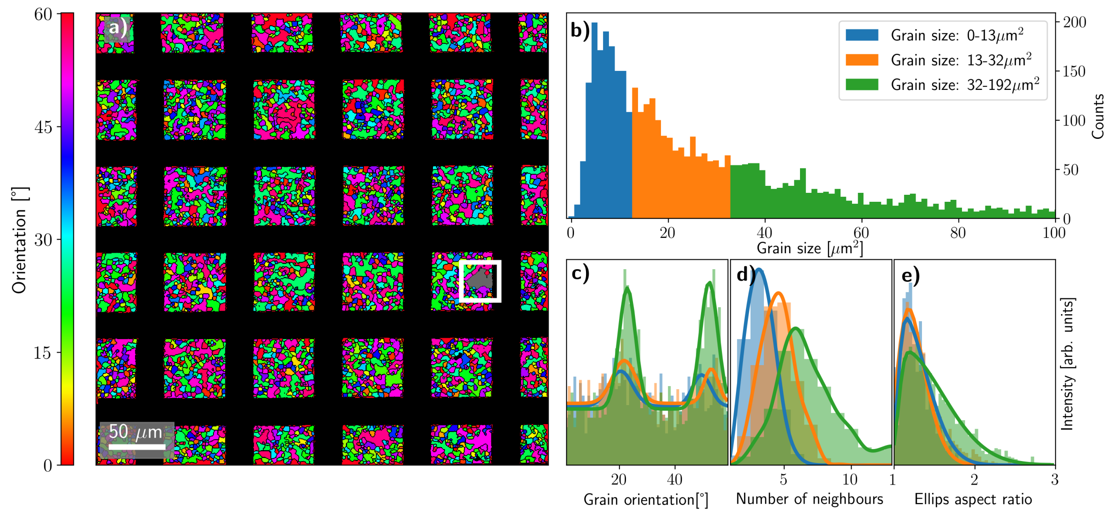

Figure 3.10.: **(a)** 1024 × 1024 orientation mapping of commercial SLG over ~0.168 mm^2 (250× magnification). The largest grain is indicated with a white square. **(b)** Grain size distribution calculated from the segmented dataset. **(c)** Correlation between grain size and orientation, indicating a preferential orientation for larger grains. The solid lines are the fitted results to the sum of two Gaussians and an offset. **(d)** Distribution of the number of neighbors as a function of grain size showing an increase in neighbors with increasing grain size. The solid line is a smoothed line through the data points. **(e)** Analysis of the aspect ratio of grain shape as a function of the grain size. The solid line is a skew normal fit through the data points.

3.5.2. MoS_2 Orientation Mapping

In order to demonstrate the applicability of the method to other LMs, such as TMDs, a MOCVD-MoS_2 sample is analyzed (see Fig. 3.11). To achieve the largest FOV, without movement of the stage, we use the longest available working distance, and perform a 512×512 probe position scan on ~2.36 mm^2, with a dwell time of ~40ms. The acceleration voltage, working distance, camera length and pixel size are 20 keV, 16 mm, 34 mm and 3 μm respectively. This MOCVD-MoS_2 ranges from one to three layers, with grain sizes in the nm range as can be seen in magnified VDF image Fig. 3.11(d). Black contrast corresponds to lacey carbon support grid, while bright regions are several-layer grains of MoS_2. The large FOV scan cannot resolve the small grains since the probe step size is 3 μm, larger than the small grain size. Fig. 3.11(a) shows the orientation map, indicating a single orientation (the positions of the diffraction spots remain the same across the scanned area), related to the epitaxial growth on sapphire giving the same crystal orientation with respect to the original substrate before exfoliation. Fig. 3.11(b,c) plots MoS_2 diffraction patterns at two points 1.3 mm apart, showing that the orientation is the same for both. Note that contrary to the experiments on SLG, the central beam is visible since, due to the stronger scattering on the MoS_2, less count rate remains in the central beam. Another scan at 25000× magnification, where the FOV corresponds to 3 pixels in the large scan (50×), is acquired in order to check the MoS_2 microstructure. In Fig. 3.11(d), the intensity of the second order spots indicates the presence of MLs. The orientation map of the high magnification scan in Fig. 3.11(e) confirms that most 2 and 3L areas are epitaxially grown on top of the first layer. However, regions with different orientations are also present (~3%), in good agreement with 4D STEM TEM measurements performed at ~1Mx magnification [149]. D

The rich 4D STEM data can additionally be used to prove the existence of the 1L-3L MoS_2. This is done by checking the intensity of the second order diffraction spots since a significant difference in intensity between 1,2 and 3L MoS_2 is expected [149]. In Fig. 3.12(a) a VDF using an annular detector on the second order diffraction spots is shown. Normally, a clear distinction between intensities should be seen for different number of layers. However since the grain

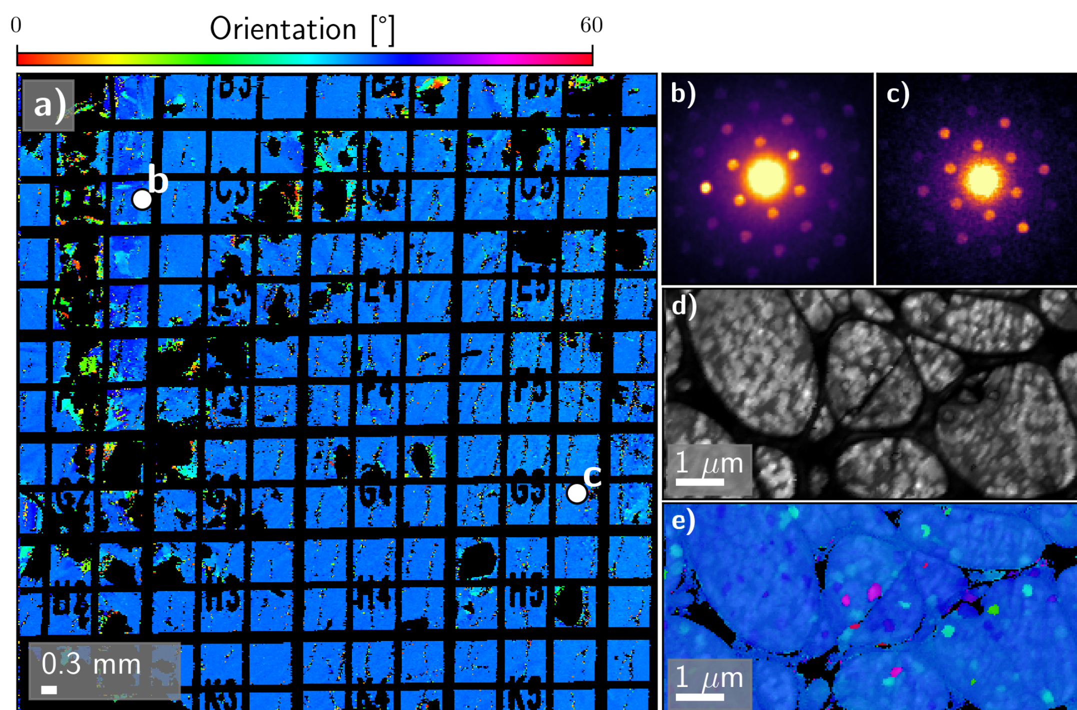

Figure 3.11.: **(a)** Orientation map of MoS_2 film, showing a single orientation (the positions of the diffraction spots remain the same across the scanned area) over a $\sim 2.36\ mm^2$ field of view. **(b-c)** Diffraction patterns from positions indicated on (a). **(d)** The second order diffraction spot intensity mapping from scan at higher magnification (250×), where bright areas are 2 and 3L MoS_2 grains. **(e)** Orientation map (with overlapped VDF (d) for visual effect) showing that most 2 and 3L are epitaxially grown on top of the first layer.

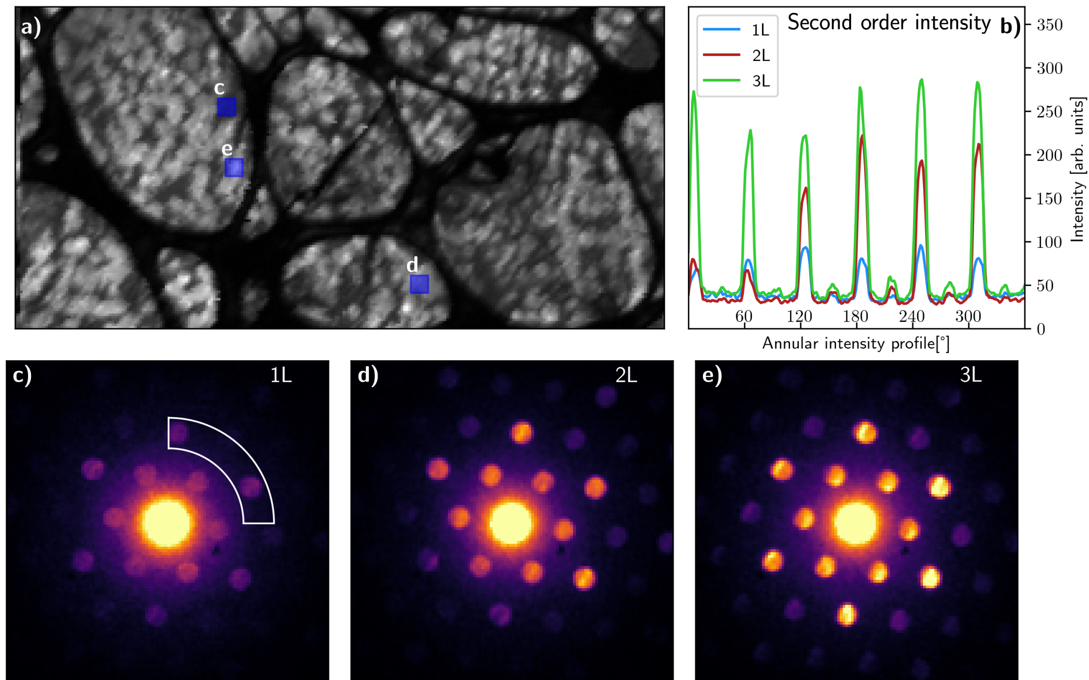

Figure 3.12.: **(a)** The second order diffraction spot intensity mapping from scan at higher magnification (250×), where bright areas are 2 and 3L MoS_2 grains. **(b)** The annular intensity profiles of three diffraction patterns indicated on (a). The increase in intensity indicates the presence of multiple layers. The non uniformity arises from a tilt with respect to the incoming electron probe. **(c-e)** The diffraction patterns where a clear increase is seen for the second order intensity diffraction spots.

sizes are similar to the size of the incoming probe, the measured diffraction pattern is a linear combination of the different ML systems, making it hard to distinguish between 1, 2 or 3L MoS_2 since the signal will be blurred. In order to validate the presence of 1, 2 and 3L, diffraction patterns corresponding to these different number of layers are shown in Fig. 3.12(c-e). To quantitatively show the increase of the signal, the annular intensity profile of the three different diffraction patterns is shown in Fig. 3.12(b). The difference between the layers is clearly visible. Note that the 2L diffraction pattern has a non uniform intensity for the six spots which is due to a tilt of the MoS_2 crystal with respect to the incoming electron beam.

3.5.3. Comparison between P-SHG and 4D STEM Orientation Mapping

The comparison of our approach with alternative optical methods, like second harmonics generation (SHG) imaging microscopy [150], provides a benchmark for the performance. We compare orientation mapping results with polarization-resolved SHG (P-SHG) microscopy [151, 152]. We use a CVD 2L-MoS_2 as a test sample, transferred onto a carbon quantifoil grid and place this in both measurement setups, targeting the same sample areas. The 2L-MoS_2 sample has AB stacking with a broken inversion symmetry along the armchair direction [151]. This allows detectable SHG signals using e.g. photomultiplier tubes, since the second-order nonlinear optical susceptibility tensor is non-zero [152].

Mapping the armchair orientation gives us the same orientation information as 4D STEM. Fig. 3.13(a) shows the VDF for a region with two MoS_2 flakes (marked with red and blue squares). The orientation map is in Fig. 3.13(b). The two regions have approximately the same orientation. By fitting the peaks with a Gaussian, the average difference in orientation between both grains is $0.2 \pm 0.1^\circ$. The same area is analyzed by P-SHG, with the polarization of the incoming light undergoing a rotation from 0° to 360° in steps of 2°. The integrated intensity map and the armchair orientation determined for every pixel are shown in Fig. 3.13(d,e). The average difference in the orientation is $1.7 \pm 0.1^\circ$, as seen from the histograms in Fig. 3.13(f). In our P-SHG experiments, the carbon quantifoil TEM grid, where the samples under examination

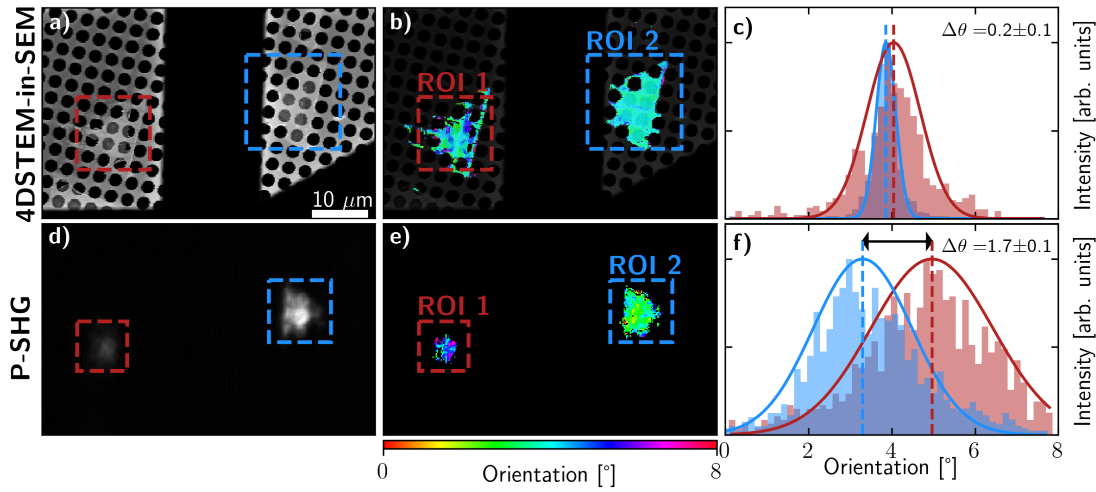

Figure 3.13.: Comparison of 4D STEM in SEM and P-SHG data on CVD-MoS2. **(a,d)** VDF signal and integration of P-SHG data for [0°–360°] with a 2° step. Regions of interest corresponding to two flakes are indicated. **(b, e)** Orientation map (with overlapped VDF image) based on 4D STEM data and mapping of armchair orientations over a large (2300 μm^2) sample area. **(c,f)** Histograms of two flakes orientation (colors correspond to selected areas in orientation map) from 4D STEM and P-SHG, showing a qualitative match.

are placed, is not compatible with the 1027 nm, 90 fs, 76 MHz laser source used to excite the SHG signals and strong degradation of the TEM grid is observed. Thus, we use a low 1-2mW excitation power, resulting in very low SHG signals from MoS_2 (although MoS_2 has a large SHG response [153]) Thus, the peak broadening and 1.5° discrepancy in flake orientation between the two techniques could be attributed to the low SNR of our SHG signals.

In the work of Psilodimitrakopoulos *et al.* [154] a similar experiment was performed where a Si_3Ni_4 support grid was used. This greatly reduced the damage induced via the P-SHG measurements. Furthermore, instead of a SEM, a STEM microscope was used to measure the orientation of the flakes using the similar 4D STEM technique. For this experiment an excellent agreement

was found between the P-SHG and 4D STEM experiments indicating that both methods provide the same information. Fig. 3.13 shows that both methods have a similar domain of application, although significant differences exist. Nevertheless, the need for electron transparent samples in SEM is relieved for P-SHG (which does not need samples on a TEM grid), making it more suitable for inline quality control of LMs placed on thick (>100 nm) substrates. The spatial resolution is up to a factor 100 better for SEM, and both can deal with similar fields of view.

3.5.4. Multilayer Analysis

As already briefly discussed in *Section 3.5.2*, the diffraction patterns contain information on the number of layers. Moreover, the type of stacking is accessible as shown in this section. First, electron diffraction patterns are simulated to show how the layer thickness and stacking can be obtained from the diffraction patterns. We start by subdividing the ML system in two different regimes. The first is where the MLs have a twist angle with respect to each other as seen in Fig. 3.4(c) where the number of diffraction spots increases compared to SLG. The other regime is when the MLs are stacked on top of each other, hence the number of diffraction spots remain the same as for SLG.

A Simulation Study

Let's start with the first regime where there is a twist angle between the diffraction spots. To confirm that Fig. 3.14(b) is indeed a BLG, different types of electron diffraction simulations are performed. The software used for the simulations is Multem [68, 69]. This software has implemented different types of approximations for the simulations such as POA [155] and multislice approximation [156]. The convergence angle (3.5 mrad) and incoming electron energy (20 keV) are the same as for the experiments.

We start with defining the pattern in Fig. 3.14(a) as a SLG. This can be done since, over the entire film, there are no diffraction patterns in which a lower intensity of the second order diffraction spots is observed. This could be because the entire film consists out of AA stacked

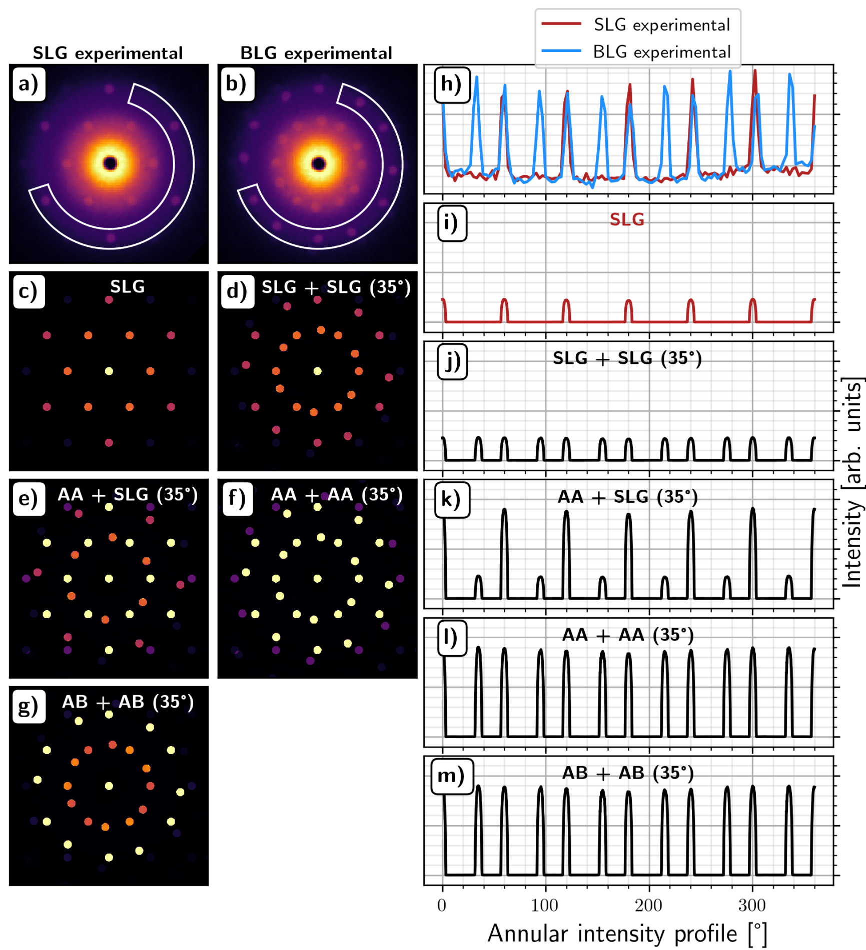

Figure 3.14.: **(a-b)** Experimental diffraction patterns from SLG and BLG (shown in Fig. 3.4(a,c)) and **(h)** comparison of annular intensity profiles of second order diffraction spots. **(c-g)** Simulated diffraction patterns of different configuration where twelve spots are present in the second order diffraction spots. The twist angle between the layers are similar to the experimental data. **(i-m)** Annular intensity profiles of SLG and two twisted SLG at 35°, SLG and AA bilayer and two AA and AB stacked bilayers respectively.

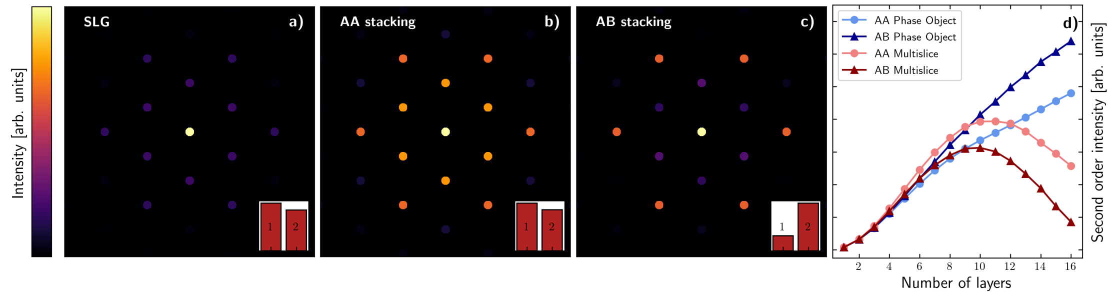

Figure 3.15.: **(a-c)** Multislice diffraction pattern simulation of SLG, BLG with AA and AB stacking. The inset is a bar plot of I_2/I_1. For SLG and AA BLG, we get I_2/I_1=0.89, for AB stacking I_2/I_1=3.17. **(d)** Intensity of second order spots with monotonic increase with N for AA and AB stacked MLG. Both PO and multislice approximation indicate kinematical behavior until N=8.

BLG but this seems to be very unlikely since AB stacking is more energy favorable. Therefore for ML graphene, AB stacking is expected instead of AA and this is not what is observed [157]. Once this reference is known, the other MLs configuration can be derived from it. To validate the BLG shown in Fig. 3.14(b), four different configuration of ML systems are simulated where for each one of them twelve diffraction spots are present for the second order reflections. These simulations are shown in Fig. 3.14(d-g). From these patterns, the annular intensity profiles of the second order spots are shown (see Fig. 3.14(j-m)) from which it is clear that the diffraction pattern in Fig. 3.14(b) can only be from BLG since the intensity of the twelve peaks are the same as for SLG which is not the case for the other types of MLs.

For the second type of ML configurations, simulations have been performed where the number of layers and type of stacking AA or AB have been varied. Fig. 3.15(a-c) plots graphene simulated diffraction patterns for (a) SLG, (b) AA and (c) AB stacking. From the simulation it is clear that the intensity of the first (I_1) and second (I_2) order diffraction spots vary for AA and AB stacked graphene. The inset image in Fig. 3.15(a-c) shows the relative intensities of I_1 and I_2. The simulations show that the ratio between I_2/I_1 gives information on the stacking

type. Fig. 3.15(d) shows the I_2 for multiple number of layers where they are AA and AB stacked for both the POA and the multislice. Both stacking types shows a similar increase in intensity hence, the I_2 can be used to determine the number of layers which does not depend on the stacking type. However, as seen for the multislice simulation, this only holds up to eight layers since dynamical scattering will start playing a role and I_2 is not monotonic with respect to the number of layers, making it harder to disentangle the number of layers.

Experimental Verification

From the simulations it is seen that the twist angle and number of layers can be determined from a diffraction pattern of graphene. To validate it experimentally, a 512×1024 scan was performed on GO flakes over a FOV of 12800 μm^2. GO is comparable to graphene hence the same type of analysis can be performed to determine the twist angle and number of layers.

Direct visual identification of multiple GO layers is hardly accessible from the SE image, due to the large difference in sample/support thickness (~1/200), and lack of contrast, due to the comparably (to substrate thickness) minor change in thickness caused by the film stacking. 4D STEM allows us to find interesting regions using offline diffraction data processing where in Fig. 3.16(a), the VDF signal of the scan is shown. The virtual aperture is placed at the second order spots to increase diffraction contrast. Some increase in the signal is seen where GO is positioned. An overall demise of signal is seen at the top due the instability of the electron gun. The distortions on the image are due to sample drift during the acquisition. The flakes can be better identified if the background signal from the diffraction patterns is removed, via the method explained in *Section 3.4.2*, and the same type of virtual detector is placed on the background-subtracted 4D STEM dataset. This is shown in Fig. 3.16(c) where the regions of GO are clearly identifiable. Note the brighter intensity for freestanding SLGO which is due to the multiple scattering of the incoming electron probe when the GO is on the substrate. At the top left, an overall increase is seen, indicating the presence of ML-GO. This area will be further investigated to show the presence of ML and determine the twist angle between them.

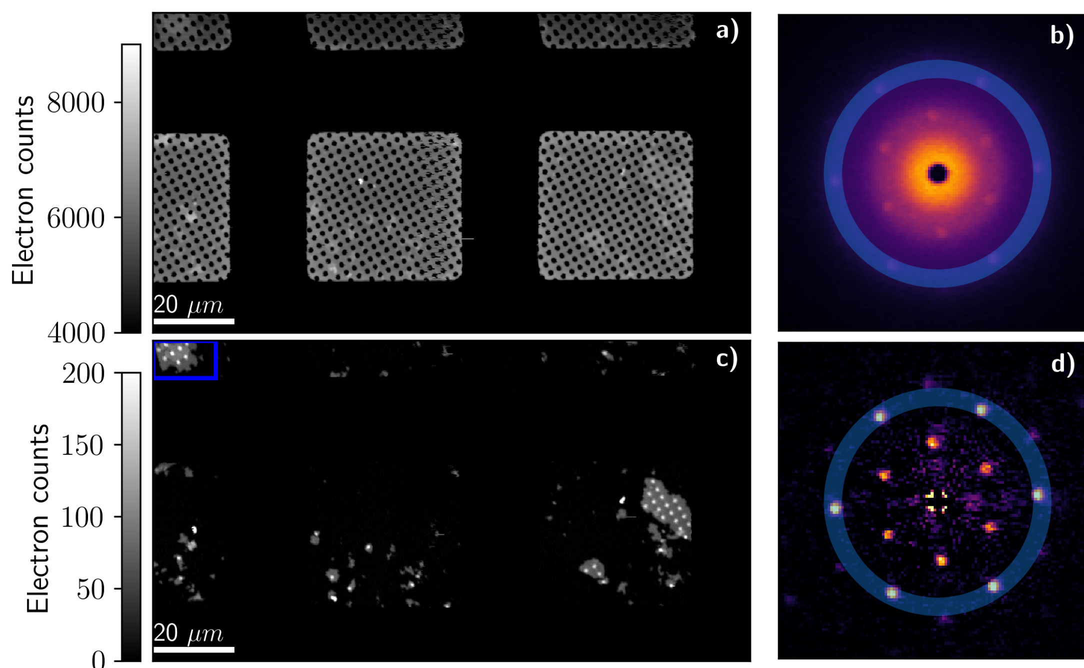

Figure 3.16.: **(a)** VDF signal of the scan. The virtual aperture is placed at the second order spots to increase diffraction contrast. Some increase in the signal is seen where GO is positioned. An overall demise of signal is seen at the top due to the instability of the electron gun. The distortions on the image are due to sample drift during the acquisition. **(b)** An unprocessed electron diffraction pattern originating from a GO flake. **(c)** VDF of subtracted diffraction patterns. The contrast comes from the sparse diffraction intensities. The lighter dots arise from the diffraction pattern inside holes, where the diffraction intensities are larger than on the substrate, due to additional scattering of electrons with substrate. At the top left, an overall increase is seen, indicating ML-GO. **(d)** Diffraction pattern shown in (b) after background subtraction using the method explained in *Section 3.4.2*

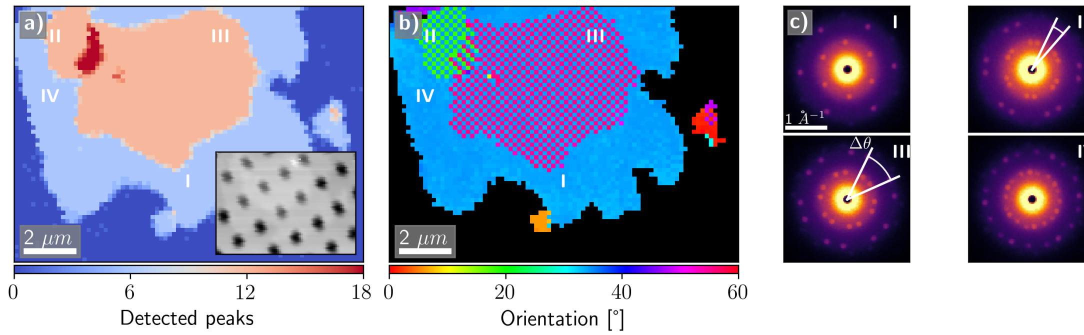

Figure 3.17.: **(a)** Number of peaks detected in the second order diffraction spots, indicating the number of layers (N), if the twist-angles are resolvable. For AB and AA stacking, N cannot be retrieved from the number of peaks, since no new spots arise with respect to 1L GO. The inset shows the VDF image. **(b)** Orientation map of GO sheets, where in total three flakes are seen with two (green and red) small flakes on top of the large flake (blue). In some region, the two smaller flakes also overlap creating a 3L region. **(c)** Diffraction patterns from regions where the twist angle is visible. The twist angle in 2L is indicated on the patterns.

In order to determine the number of layers from this region, the peak finding algorithm is applied to each diffraction pattern. Next, the number of peaks at the radius of the second order spots are counted. Six peaks indicate a 1L (AA and AB stacking excluded), while twelve peaks indicate a 2L. In Fig. 3.17(a), the number of detected peaks for the second order diffractions spots is shown where 1 to 3L GO is seen. The number of spots are not the only indication on the number of layers since some layers can be stacked on top of each other without increasing the number of spots. To exclude the presence of stacked layers, the intensity of the diffraction spots can be investigated. Therefore, a reference of SLGO is needed. This is done by taking a diffraction pattern containing six second order diffraction spots. The intensity is then compared to SLG since they would be very similar to each other [123] which is shown in Fig. 3.18(a-b). Since the intensities of the diffraction spots remain constant for the other diffraction patterns

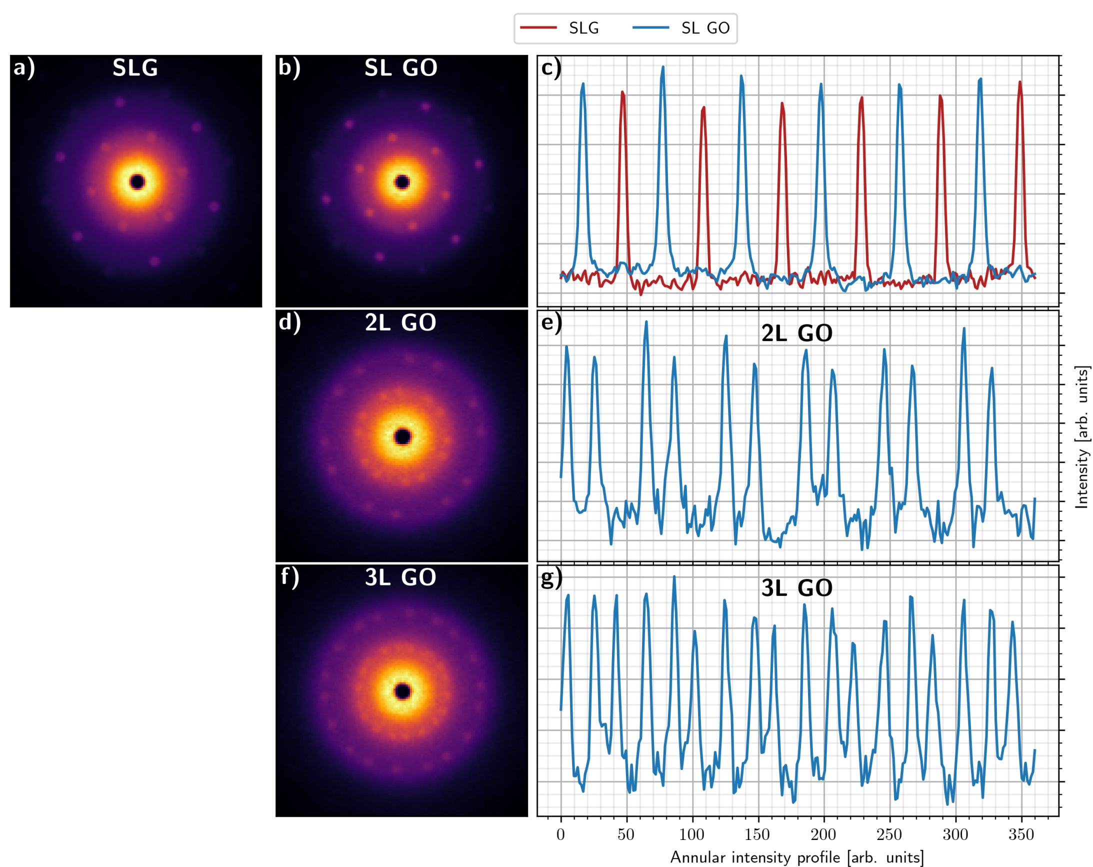

Figure 3.18.: **(a-b)** Experimental diffraction patterns from SLG and 1L-GO. **(c)** Comparison of annular intensity profiles of second order diffraction spots. **(d,e; f,g)** Diffraction patterns of 2L-GO and 3L-GO, respectively, and annular intensity profiles with the same diffraction spot intensity as 1L-GO.

where twelve and eighteen spots are detected, it is concluded that there are no stacked layers in the material and the maximum layer thickness is 3L (see Fig. 3.18). Note that since the intensity remains the same as the SLGO that the diffraction patterns do not arise from a grain boundary.

After the number of layers are calculated, the twist angle between the different layers can be obtained via calculation of the angle between the spots where an example is shown in Fig. 3.17(c). This can be performed for every diffraction pattern where for 2L GO, two values of orientation are obtained. In Fig. 3.17(b) the orientation map is shown. From the orientation map it is clear that there are three flakes in total where two smaller flakes lay on top of one large flake (blue). At some point the two smaller flakes also overlap creating a 3L region.

We now consider BLG where no twist angle is observed between the two layers. Diffraction patterns of SLG and BLG are shown in Fig 3.19(a,e). For BLG an increase in the second order peak intensity is seen. The corresponding probe positions are indicated on Fig. 3.19(c). The full scan of SLG is shown in Fig. 3.6(d), where the BLG region is indicated with a white arrow. To further investigate the BLG stacking, the annular intensity profiles of the first and second order peaks from SLG and BLG are plotted in Fig 3.19(b,f). The intensity of the first order peaks does not show much variation, whereas the second order intensity increases significantly, indicating AB stacking for BLG. Moreover, AA stacking would result in an increase of the same amount for the first order peaks [158] which is not seen here (Fig. 3.15). Therefore, the ratio between the first and second order intensities can reveal the type of stacking. This process can be applied to every diffraction pattern in the maps in Fig. 3.19, where panels (d,g) show the average peak intensities of the first and second order peaks. In Fig. 3.19(g) MLs can be identified as regions where an increase in signal is observed. To investigate stacking, the ratio between maps (g) and (d) is plotted in panel (h). A decrease of intensity in the BLG region is seen, identifying its AB stacking. For MLs other stacking sequences can occur, such as ABA, AAA, ABAA, *etc.* In order to identify these types of stacking sequences, more elaborate methods should be used [158].

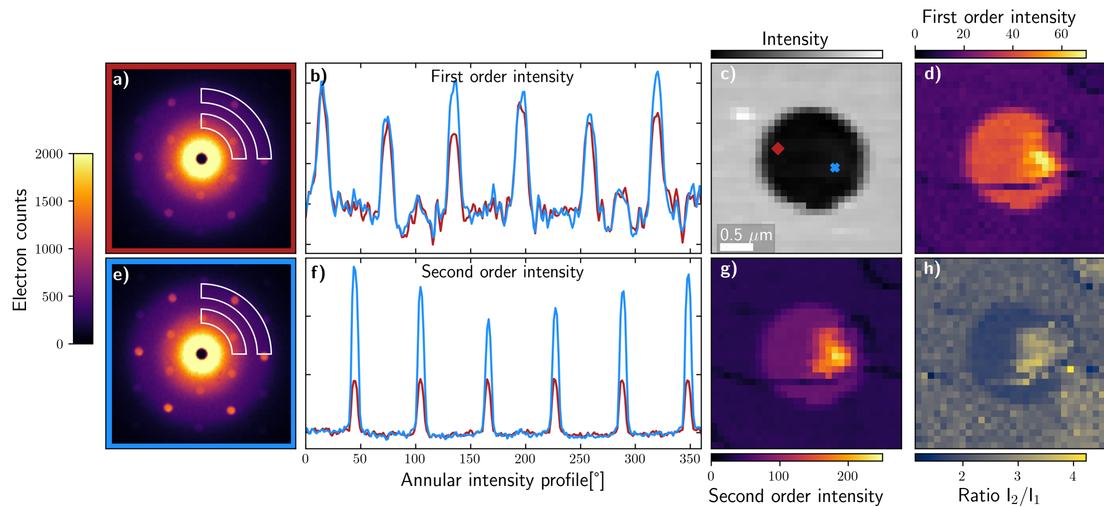

Figure 3.19.: **(a,e)** Diffraction pattern of SLG and BLG, corresponding to probe positions indicated in (c). **(b,f)** BLG stacking analysis using the comparison of annular intensity profiles of the first (b) and second order (f) spots. AB stacking is identified by a 2.5 times increase in the second order intensity, while no significant change of the first order intensity is observed. **(c)** VDF signal of the area mapped, as indicated in Fig. 3.6. (uppermost white arrow). **(d,g)** Average intensity map of first and second order spots. The area where the signals increase indicates MLs. **(k)** Identification of BLG stacking by taking the ratio between second and first order VDF images where the decrease of increase indicates AB stacking.

3.6. Conclusion

By mounting a hybrid pixel detector in an SEM, we showed that 4D STEM data can be obtained from various LMs. Their few-layer thickness makes them highly suited for transmission electron diffraction, with no need of sample preparation even at beam energies of a few 10 keV, if the material is on an electron-transparent support, or is self-supported. The method provides a rich source of information on grain orientation and boundaries, twist-angle, stacking and number of layers. Scans of up to mm sized fields of view with a nm scale electron probe are possible. The direct geometrical projection of the diffraction pattern onto the hybrid pixel detector provides a robust calibration of the scattering angles not influenced by lens drift and optical distortions, which hampers optically coupled scintillator setups. This can be especially important for measuring strain with high precision. Data processing can be automated and runs over a full dataset unattended after an initial calibration setup. This requires ~430 minutes for acquisition and a few hours of data processing on a standard desktop PC for a 1024×1024 dataset, decreased by using a detector offering a recording time reduction by more than two orders of magnitude when a more advanced version of the same camera. Even a higher reduction is expected for next generation Timepix and Medipix chips.

4. 4D STEM in Event Driven Mode

This chapter is based on:

D. Jannis, C. Hofer, C. Gao, X. Xie, T.J. Pennycook, J. Verbeeck, *Event driven 4D STEM acquisition with a Timepix3 detector: microsecond dwell time and faster scans for high precision and low dose applications*, (2021) *(Under review in Ultramicroscopy)*

4.1. Introduction

The development of the direct electron detectors (see *Section 1.2.1*) has revolutionized the imaging capabilities in TEM where due to the improved DQE, more dose efficient experiments where possible. One obvious example of this is in the field of molecular biology where the resolution provided by the electron microscopes is limited by the poor signal achievable using the extremely low doses required to avoid unacceptable damage to the material than by the electron optics themselves [34, 35].

The most fragile dose sensitive samples, such as proteins, have largely been the preserve of conventional phase contrast TEM imaging as in cyro-EM. Phase contrast imaging in STEM has historically been far less dose efficient, but advanced STEM methods that also provide highly dose efficient phase contrast signals have been developed and also benefited greatly from advances in pixelated detector technology [159]. Two of these dose efficient 4D STEM reconstruction algorithms are explained in *Section 2.1.2* where ptychographic methods have been shown capable of providing significantly enhanced dose efficiency over conventional TEM phase contrast [160], thus offering the prospect of another leap forward in low dose performance as well as a greater precision, for example for mapping local charge densities [161–163].

4D STEM methods such as iCoM or ptychography do not require cameras with particularly large numbers of pixels [164, 165]. The achievable frame rate depends on the number and bit depth of the pixels due to finite readout and data transfer rates, the development of small direct electron detectors has greatly benefited 4D STEM. Small fast hybrid pixel direct electron detectors such as the Medipix3 [166] are particularly attractive as they also offer the benefit of beam hardness, with the detection layer physically separated from the readout electronics. However, such detectors have typically been employed at frame rates of at most a few thousand frames per second [167].

By utilizing the much reduced bandwidth required for a 1-bit counting depth in each pixel of a Medipix3 detector, O'Leary *et al.* demonstrated a significant speedup of 4D STEM acquisition at a 12.5 kHz frame rate, corresponding to an 80 microsecond dwell time [168]. Although this

allowed them to achieve a relatively low dose of 200 e^{-}Å^{-2} by using an extremely low probe current in a focused probe configuration, such a dose is still much higher than required by the most beam sensitive materials and the speed is still far slower than the single to few microsecond dwell times used in rapid conventional ADF based STEM measurements. Detector technology continues to advance and achievable frame rates are increasing. For example 11 microsecond dwell time 4D STEM has recently been achieved with a specially designed custom extremely high frame rate camera [169, 170], but this is still an order of magnitude slower than typical for rapid scanning STEM.

Here we demonstrate the use of an alternative event driven detector architecture to completely remove the bottleneck in speed for 4D STEM in comparison to conventional STEM detectors based on scintillators and photomultipliers for the low probe currents desirable for low dose operation. The event driven Timepix3 detector was developed with an emphasis on time resolution for applications in a wide range of scientific disciplines with a maximum time resolution of 1.56 ns [171, 172]. Event driven operation allows one to take advantage of event sparsity to achieve enhanced time resolution by avoiding the readout of pixels containing zero counts. A conventional frame-based detector spends an equal amount of time reading out such zero pixels which add nothing to the information content of the data. In STEM, one can reduce the dose imposed on a sample per unit area by reducing the probe current and dwell time, both of which increase the sparsity of the events in each probe position. We present results from 4D STEM performed with a Timepix3 detector at dwell times of a few microseconds down to 100 ns at both 60 and 200 kV accelerating voltages. Although the detector configuration used herein requires the use of low probe currents, we show how the speed facilitates multiply scanned 4D STEM to be used in order to increase the SNR with minimal susceptibility to drift. The results demonstrate that event driven camera technology enables the efficiency of 4D STEM, and in particular, electron ptychography to be exploited for both large fields of view and the extremely low doses.

4.2. Experimental Setup

The event-based detector used in the camera setup in this work is the AdvaPIX TPX3 [173] which is a Timepix3 based detector where the thickness of the sensitive silicon layer is 300 μm. Timepix3 chips are 3-side tileable with a maximum event capacity of $0.43{\times}10^6/\text{mm}^2/\text{s}$. A single Timepix3 chip contains 256×256 pixels where each pixel has a size of 55×55 μm, resulting in a theoretical capacity of $80{\times}10^6$ counts per second for a single chip device. However due to the bandwidth of the USB 3.0 port used for the readout from our device to the computer, the maximum capacity for our single chip setup is $40{\times}10^6$ counts per second when using flat field illumination. In Fig. 4.1(a), a schematic view of the setup is shown where an incoming convergent electron beam interacts with the sample. After the interaction with the sample, the electron beam propagates into the far-field regime where the detector is placed. In Fig. 4.1(b) an example of the data is shown where for every incoming event its point of impact and time of arrival (TOA) are saved. Knowing the probe position at each time, the conventional 4D STEM dataset can be obtained. In Fig. 4.1(c) some measured diffraction patterns are shown in which the sparsity is seen due to the low dose per scanned point. The resulting PACBED pattern, calculated from the sum of all diffraction patterns, is also shown.

The Timepix3 detector was mounted on a probe-corrected FEI Themis Z using a custom designed retractable mount interface shown in Fig. 4.1(d). In order to synchronize the scan coils with the detector, a custom scan engine is used [135, 174]. The detector and scan engine are synchronized using a 10 MHz reference clock output which is then multiplied with a custom designed phase locked loop circuit to act as a 40 MHz master clock for the Advapix in order to keep both scan engine and camera synchronised in time. At the start of the acquisition, a synchronisation signal is generated by the scan engine which triggers a recording sequence on the detector side. In this work, no flyback time is applied since we aim to reduce the dose as much as possible and we do not have access to a fast enough beam blanker to shut the beam down. Both the detector and scan engine have an application programming interface (API) in Python3 giving us the ability to automate the acquisition sequence.

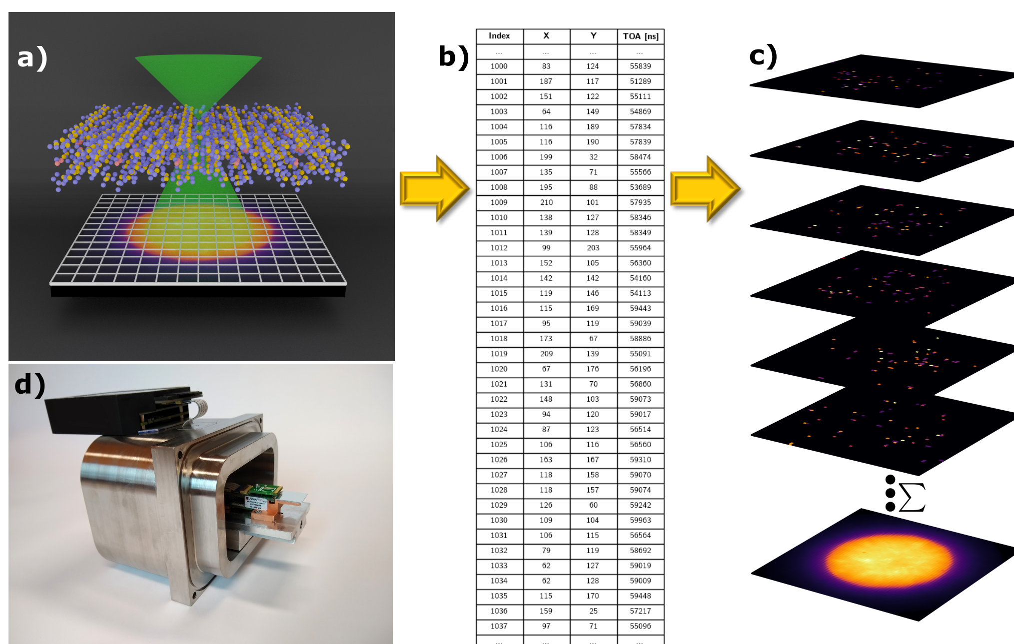

Index	X	Y	TOA [ns]
...	...	...	...
1000	83	124	55839
1001	187	117	51289
1002	151	122	55111
1003	64	149	54869
1004	116	189	57834
1005	116	190	57839
1006	199	32	58474
1007	135	71	55566
1008	195	88	53689
1009	210	101	57935
1010	138	127	58346
1011	139	128	58349
1012	99	203	55964
1013	152	105	56360
1014	142	142	54160
1015	119	146	54113
1016	115	169	59443
1017	95	119	59039
1018	173	67	58886
1019	209	139	55091
1020	67	176	56196
1021	131	70	56860
1022	148	103	59073
1023	94	120	59017
1024	87	123	56514
1025	106	116	56560
1026	163	167	59310
1027	118	158	59070
1028	118	157	59074
1029	126	60	59242
1030	109	104	59963
1031	106	115	56564
1032	79	119	58692
1033	62	127	59019
1034	62	128	59009
1035	115	170	59448
1036	159	25	57217
1037	97	71	55096
...	...	...	...

Figure 4.1.: **(a)** The schematic setup, where a convergent electron beam is scanned across the sample and during the scan, the point of impact and TOA is measured for each incoming electron. **(b)** The data list created by the detector where for every event the point of impact and TOA is indicated. **(c)** When the probe position at each time is accurately known, a diffraction pattern belonging to the time range for a given probe position can be obtained resulting in a full 4D STEM dataset. **(d)** Custom built retractable assembly to place the Timepix3 detector in the electron microscope column.

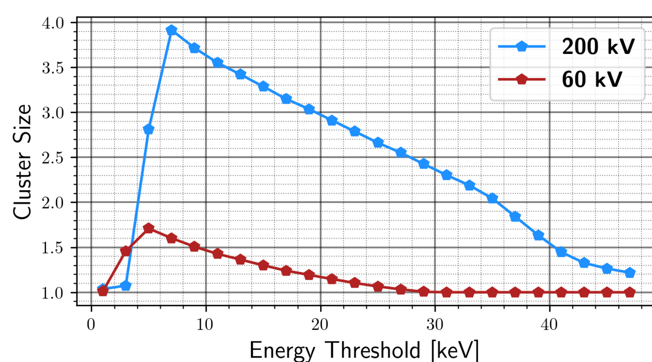

Figure 4.2.: The average cluster size calculated as a function of threshold for 60 and 200 kV accelerating voltages.

The incoming raw data from the detector is processed using self-written software and the ptychographic reconstruction is performed using the single side band ptychography reconstruction algorithm. The full recorded dataset and data processing software is made available in Zenodo allowing others to duplicate our efforts or to experiment with new algorithms that are optimised for event-based data streams [175].

4.3. Detector Characterization

The Timepix3 detector is a hybrid direct electron detector where the silicon sensor layer is bonded onto the underlying processing ASIC electronics similar to the Medipix chips [176, 177]. As for the Medipix detectors, the main parameter to be changed is the energy threshold which is a pre-set discrimination level used to discriminate an electron event above the noise floor. Hence, by varying this parameter we can select the amount of signal detected for a particular beam current. The energy threshold influences mainly two things, firstly the amount of detected events when one electron hits the detector and secondly the number of detected electrons. Throughout the rest of this chapter the amount of pixels which are excited by a single

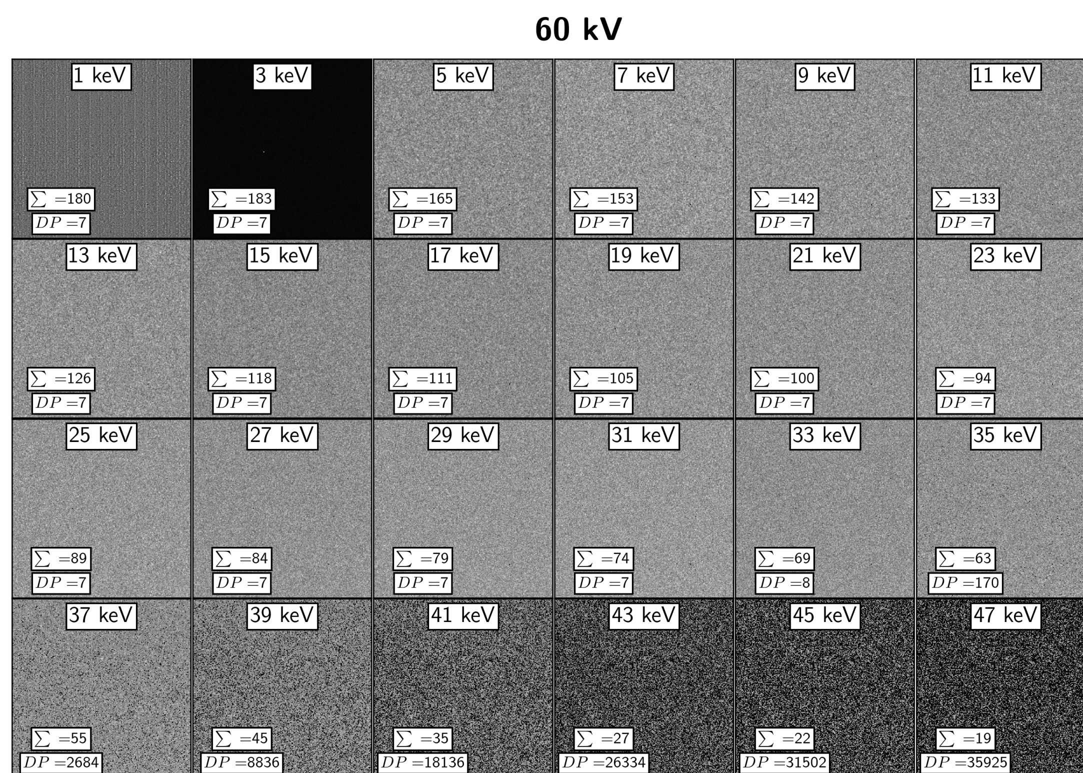

Figure 4.3.: The flat field illumination of 60 kV electrons where the threshold is varied. The relative total number of detected electrons compared to 21 keV in percentage (Σ) is indicated and also the number of dead pixels (DP) is indicated in the plots.

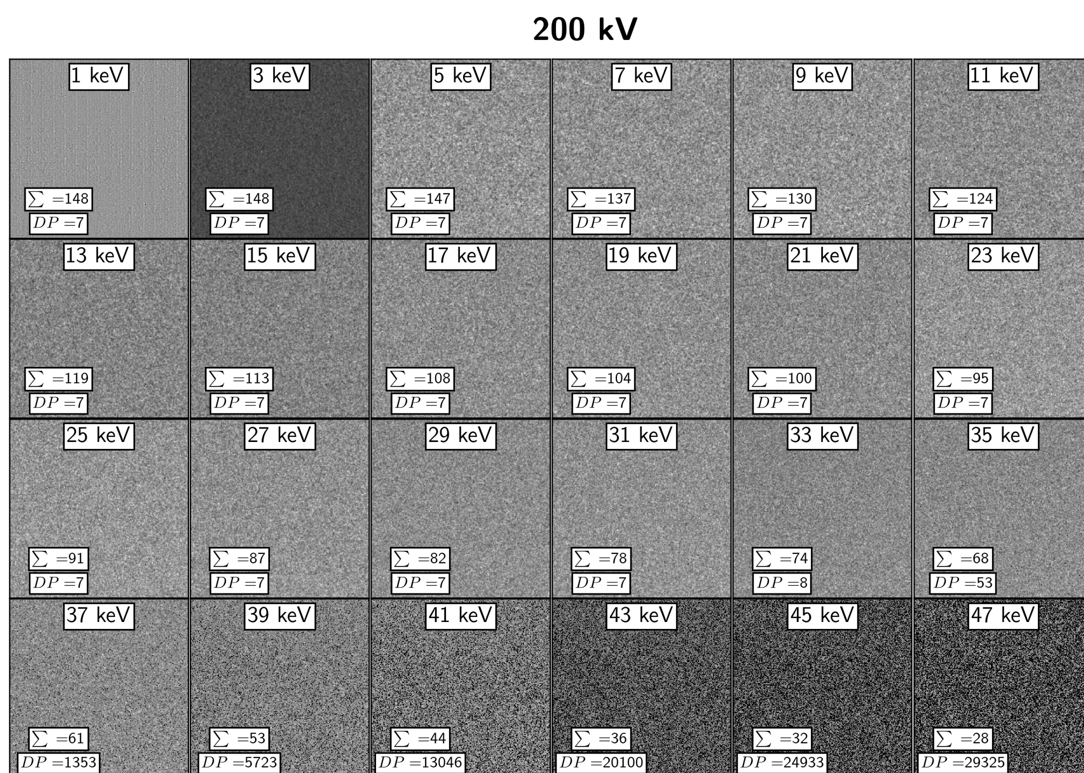

Figure 4.4.: The flat field illumination of 200 kV electrons where the threshold is varied. The relative total number of detected electrons compared to 21 keV in percentage (Σ) is indicated and also the number of dead pixels (DP) is indicated in the plots.

electron will be referred to as a cluster. The identification of the clusters is derived from the work by van Schayck *et al.* [178] where clusters are identified by checking if neighbouring pixels are excited within a small time interval (~100 ns). The energy threshold also influences the number of detected electrons because increasing the threshold will results in some events remaining undetected since they do not exceed the threshold value while scattering inside the sensitive silicon layer.

The first step is to find the appropriate interval of threshold values under which the camera performs without any artefacts. In Fig. 4.2 the average cluster size calculated as a function of threshold for 60 and 200 kV accelerating voltages by using a flat field illumination is shown. At low thresholds from 1-5 keV the cluster size decreases with decreasing threshold. This might seem nonphysical since the lower the threshold the larger the cluster size induced by an electron hit should be. However, one possible explanation for this effect would be that at low thresholds ≤5 keV thermal noise or other types of random noise start to be detected resulting in a smaller average cluster size since the average cluster size of random noise is one. Although we note that at 1 kV the grid pattern artefact that appears in the flat field images is likely due to the underlying detector geometry. The results of flat field illumination of the incoming electron beam at 60 and 200 kV accelerating voltages are shown in Fig. 4.3 and 4.4 as a function of the threshold voltage. In order to remove the influence of such noise, the minimum usable threshold was determined to be at 7 keV. From Fig. 4.3 and 4.4, a maximum value of the threshold is determined by investigating the number of dead pixels as a function of threshold. A dead pixel is defined as a pixel which is not giving any counts during the acquisition. At 35 keV a sharp increase in the number of dead pixels is seen making higher threshold values undesirable for the experiments. Therefore the valid range of thresholds is determined to be between 7 and 33 keV. Note that these settings depend on an internal calibration routine that is performed when producing the detector.

In Fig. 4.5(a), the cluster size as a function of energy threshold is plotted for 60 and 200 kV acceleration voltages. As expected, the cluster size decreases as a function of increasing energy threshold where for 200 kV the lowest cluster size is approximately 2.2 pixels and for 60 kV

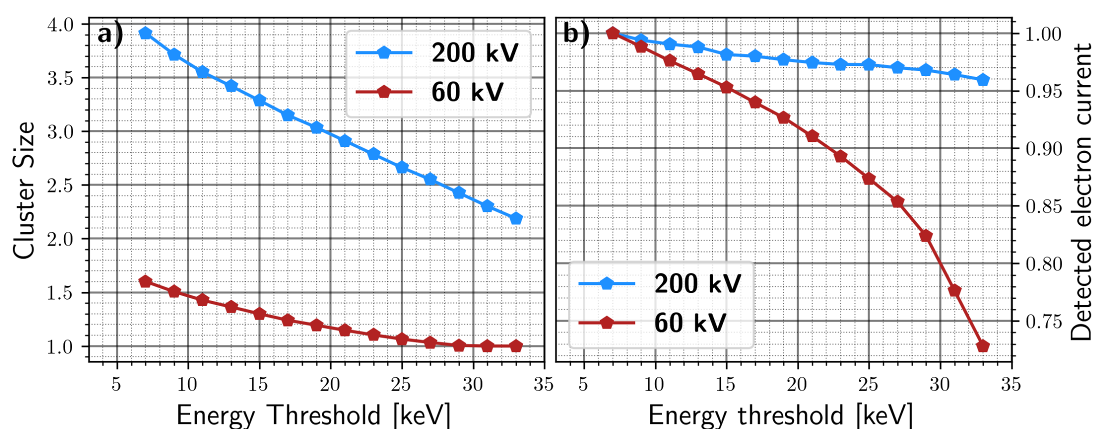

Figure 4.5.: **(a)** The cluster size as a function of energy threshold for the two acceleration voltages 60 and 200 kV. **(b)** The detected electron current which is calculated by dividing the number of events per second on the detector by the average cluster size. The detected current is relative compared to the detected current at a energy threshold of 7 keV.

the size drops to 1 pixel at a threshold of 33 keV. In Fig. 4.5(b), the detected electron current is shown as a function of energy threshold for the two acceleration voltages. The detected electron current is calculated by dividing the number of events on the detector by the cluster size within a fixed amount of time (two seconds in this experiment). From Fig. 4.5(b), it is seen that at higher energy thresholds (33 keV) for 60 kV, a significant amount of electrons (25 % at 33 keV) remain undetected. Since the incoming electron current is lower than the detection threshold for measuring the current via the fluorescent screen or spectrum drift tube method, no absolute measurement of the electron current could be performed here. However in the work of Krause *et al.* [179] it is shown that direct electron detectors provide an accurate estimate for low currents. Since the 7 keV threshold loses the least amount of electrons (see Fig. 4.5), this threshold is the most accurate measurement of the incoming electron count rate. Note that this is a lower boundary on the actual current since some electrons will backscatter and other

electrons will scatter inside the silicon layer without exceeding the threshold energy. In the rest of this work, the total incoming electrons are calculated by dividing the number of detected events by the cluster size which is then multiplied by the ratio between the electron current at 7 keV and the used threshold value (see Fig. 4.5). For example if $1{\times}10^6$ events per second are detected with a threshold of 30 keV at a 60 keV accelerating voltage, the incoming electron current is calculated by multiplying this value by 1/1.2, the inverse of the cluster size, and 0.8, the ratio between the detector electron current at 7 and 30 keV. From Fig. 4.5 we can conclude that at this lowest threshold, more electrons are detected, but they make on average a larger cluster size reducing the maximum current on the detector. At 200 kV, the amount of events at the highest threshold (33 keV) is only 4% less compared than when using a threshold of 7 keV while it significantly reduces the cluster size. This results in a higher allowable beam current as compared to lower threshold levels since there is an upper limit on the maximum count rate of the detector. The detector was also briefly tested with an acceleration voltage of 300 kV. The cluster size increases quite considerably to an average of six pixels at a threshold of 33 keV. This means that the incoming current should be dropped by a factor of three compared to 200 kV which makes the use of 300 keV electrons much less attractive and is therefore not considered further.

When recording a data stream we find that sometimes the camera does not record the incoming electrons for certain time periods ranging from 50 μs to 1.75 ms. To investigate this, the dataset of the low magnification scan shown in *Section 4.4.2* is used. In Fig. 4.6(a), a histogram calculated from the TOA of the incoming events with a bin size of 10 μs is shown. This shows the number of events where at some particular times, the counts drop unphysicaly to zero. The time that the camera is down for this acquisition is 0.12%, which is a relatively small proportion of time compared to the entire acquisition. In Fig. 4.6(b), the corresponding VDF image is shown where the virtual detector region is shown in Fig 4.9(b). The black lines on the image are due to the artefacts. In this work a very simple method is used to mitigate the artefacts by filling these pixels with the average value of the image. While this is likely not the best way to reconstruct the images, this is beyond the scope of our present work. In the future we expect other improved

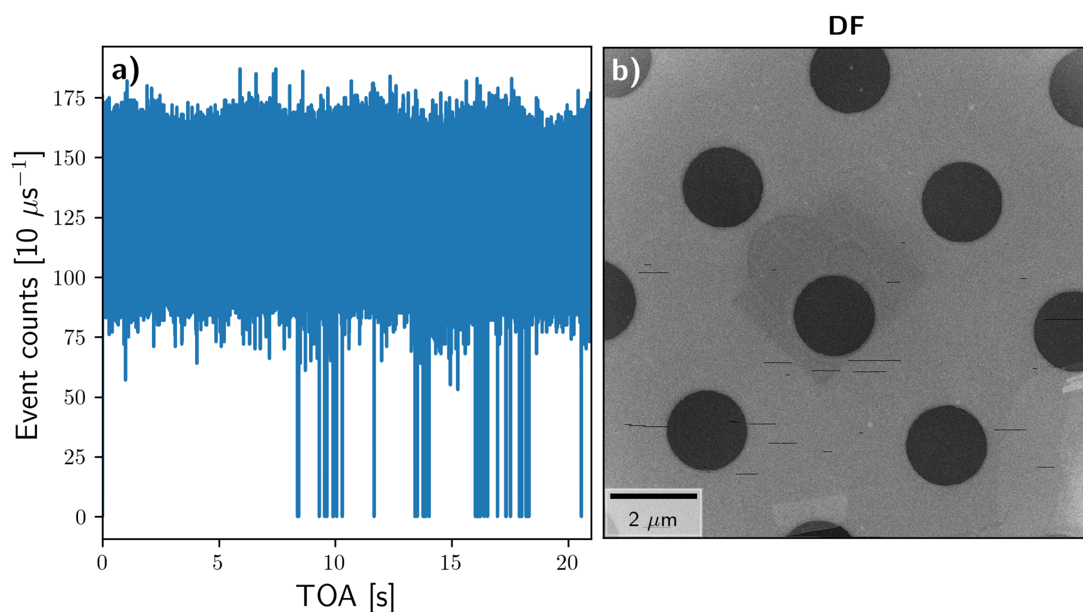

Figure 4.6.: **(a)** A histogram of the TOA of the incoming events with a bin size of 10 μs. **(b)** The reconstructed DF signal where the dark lines correspond to the artefacts which arise when the detector does not detect signal in some time windows.

methods for image restoration or ideally ways to avoid the artefacts in the first place can be developed.

4.4. Results

4.4.1. Signal Reconstruction

A 2D WS_2 sample was used to showcase the performance of the detector at 60 kV. A multi-frame acquisition is performed where the probe, with a convergence angle of 25 mrad, is scanned three times over 1024×1024 probe positions at a dwell time of 6 μs. The dose per frame is

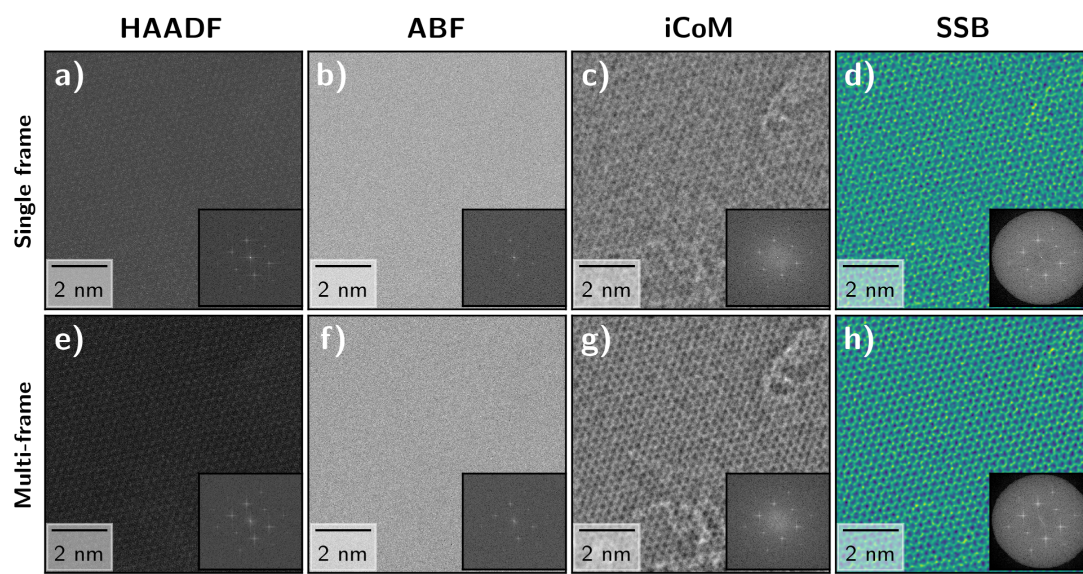

Figure 4.7.: **(a,e)** Single and summed multi-frame HAADF images from a $3 \times 1024 \times 1024$ scan at 6 μs dwell time. The sample is a monolayer of WS_2. The HAADF signal is collected with the conventional HAADF detector. **(b,f)** Single and multi-frame ABF images reconstructed from the simultaneously acquired 4D STEM dataset. **(c,g)** The reconstructed iCoM images from the single and multi-frame scans. **(d,h)** The reconstructed SSB images from the single and multi-frame scans. The power spectrum of each image is shown in the inset.

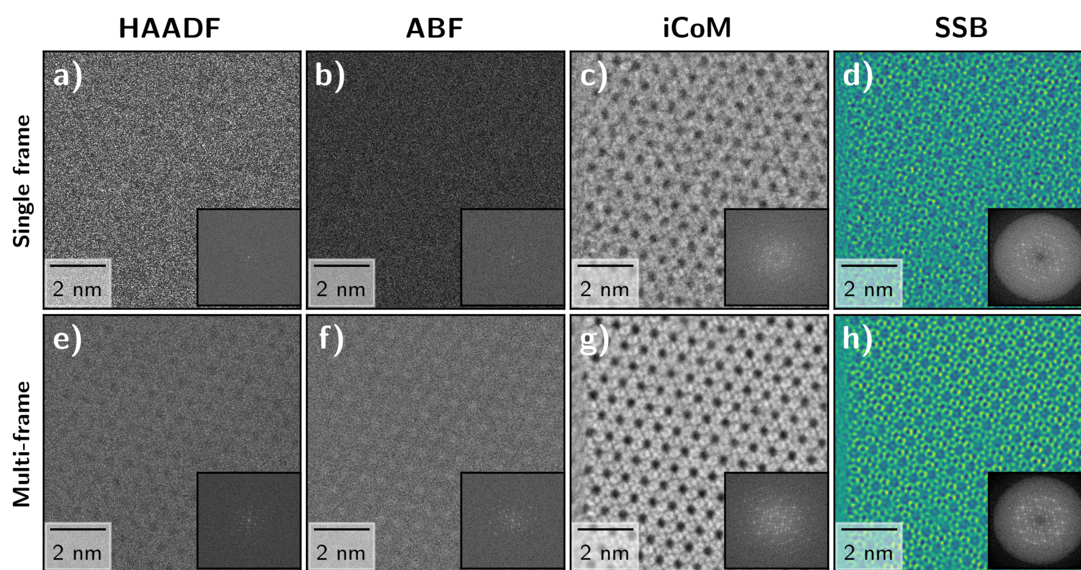

Figure 4.8.: **(a,e)** Single and summed multi-frame HAADF images from a 1 μs dwell time $10 \times 1024 \times 1024$ scan of a silicalite-1 zeolite sample. **(b,f)** Single and summed multi-frame ABF images reconstructed from the use of a virtual detector. **(c,g)** The reconstructed iCoM images from the single and multi-frame scans. On the left of the image the distortions due to finite response time of the scan coils are visible. **(d,h)** The reconstructed SSB images from the single and multi-frame scans. The power spectrum of each image is shown in the inset.

estimated to be 6000 $e^{-}Å^{-2}$. The size of the dataset is 6.6 GB which is a significantly lower data storage requirement than using a 1-bit mode of an equivalently sized frame-based detector where the data size would be 33 GB.

In recent years, another type of data storage for frame-based detectors have been developed. The compression method is named electron-event representation (EER) which stores each electron-detection event as a tuple of position and time [180]. This is similar to the output of event-based detectors. However the speed of the frame-based camera is still determined by the fps which is not the limit for the event-based detectors [181, 182].

During the acquisition, the signal from the high-angle annular dark-field (HAADF) detector was read out simultaneously to collect the electrons which scatter to higher angles than the pixelated detector and provide a simultaneous Z-contrast image. The detector geometry of the HAADF is similar to the ADF (see Fig. 2.3) where the inner angle of the detector is larger. In this work we provide three different signal reconstruction methods which are ABF (see Fig. 2.3 for detector configuration), where only events which land on an annular ring on the detector is integrated from 33 to 100% relative to the convergence angle in order to obtain the image. Secondly, the iCoM signal is reconstructed using the algorithm described in *Section 2.1.2*. Finally, the single side-band (SSB) method is used to retrieve the phase of the object which is described in *Section 2.1.2*. The ABF and iCoM signals are calculated directly from the event list (see Fig. 4.1(b)) whereas for the SSB reconstruction the data was converted to standard non-sparse four-dimensional data for the most facile input to our existing ptychographic processing software, which was written with framing cameras in mind. In the future the algorithms can be modified to accept the sparse event data directly or even perform 'live' imaging [182, 183].

The resulting signals (ABF, iCoM and SSB) created from the 4D STEM images are shown in Fig. 4.7. The HAADF signal in Fig. 4.7(a,e) arises from the conventional HAADF detector (47-210 mrad) which we recorded in parallel with the event-based detector data. The reconstructed multi-frame images are aligned using an open-source software which was developed for low SNR cryo-STEM data [184]. The software uses all possible combinations of image correlations, instead of using a single reference image, to determine the optimal shift. The relative image distortions

between the scans are calculated using the SSB images due to its good contrast. The resulting images shifts were then also applied to the HAADF, ABF and iCOM images to align them. In Fig. 4.7(b,f) the ABF signal is shown where the low contrast arises as a result from the low dose conditions. This is not particularly surprising as in the WPOA zero contrast is expected when using a centrosymmetric detector configuration, and the 2D WS_2 is of course thin, relatively weak and lacking in channeling contrast in comparison to typical 3D materials [185]. The iCoM signal shown in Fig. 4.7(d,h) and the SSB ptychographic reconstruction shown in Fig. 4.7(c,g) both take greater advantage of the 4D data and show much stronger signals. The difference in contrast of the SSB with respect to the iCoM signal arises from the different contrast transfer functions (CTF) of both signals [72, 186] and the way in which the ptychographic method keeps track explicitly of where in probe reciprocal space each frequency is transferred [164, 185]. The lower limit of the electron dose is calculated using the information from Fig. 4.5 (b) where the experiment was performed at a energy threshold of 30 keV indicating that minimally ~25% of the incoming electrons are not detected. This gives a minimum dose of ~6000 $e^{-}Å^{-2}$ per frame.

The same type of data acquisition at 60 kV can be performed at 200 kV where the main difference is the larger cluster size at 200 kV. However in terms of lost electrons, the 200 kV is better since only a small fraction (3%) seems to be lost by increasing the energy threshold to the 31 keV used for the 200 kV data presented here taken of a silicalite-1 zeolite [187]. A $10 \times 1024 \times 1024$ probe position scan is performed at a dwell time of 1 μs where the dose per frame was 300 $e^{-}Å^{-2}$ and the total dose over the ten scans was 3000 $e^{-}Å^{-2}$. The convergence angle used during the experiment was 12 mrad. In Fig. 4.8, the reconstructed signals are shown where the HAADF and ABF show, as expected, very low contrast. As for the WS_2, the iCoM and SSB signals both show good contrast. The distortions visible on the left of the images are due to the slow response of the scan coils at this dwell time as we have chosen to use no flyback time to keep beam damage as low as possible.

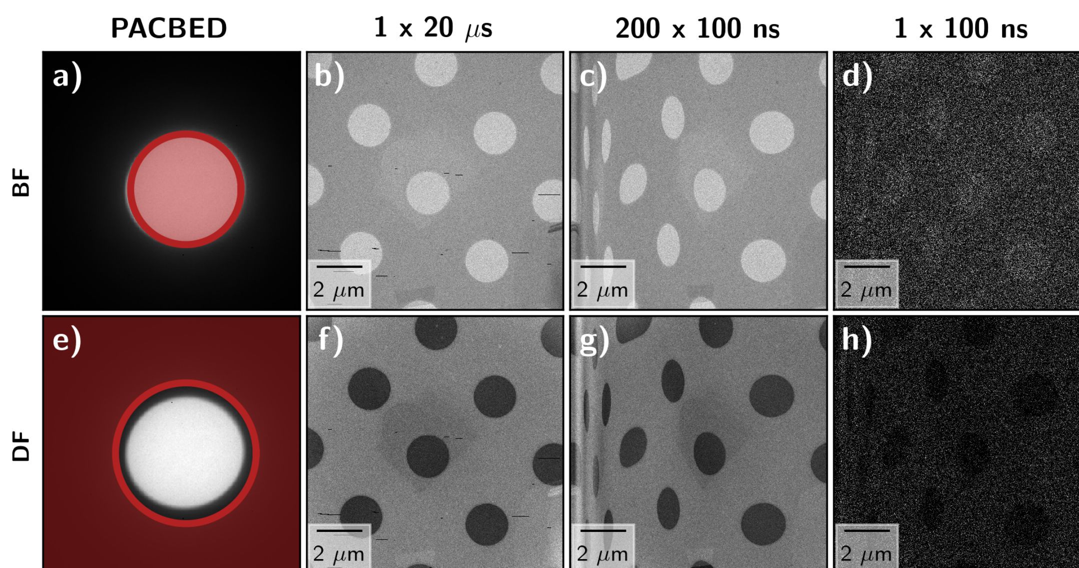

Figure 4.9.: **(a,e)** The PACBED of the 4D STEM scan where, for both signals bright field (BF) and dark field (DF), the virtual detectors are shown. **(b,f)** The BF and DF signal of a 1024×1024 scan at 20 μs dwell time where the sample is a low magnification image of a holey carbon film. **(c,g)** The summed BF and DF image of the same scan size with a dwell time of 100 ns and 200 frames which are scanned. Clear distortions arising from the response time of the coils are visible but the detector has no significant issues with this dwell time. **(d,h)** A single BF and DF frame of the fast scan using a dwell time of 100 ns.

4.4.2. Nanoseconds Dwell Time

To check if we were able to record 4D STEM scans at dwell times of 100 ns and that the detector is still able to record a proper 4D STEM dataset, a low magnification scan on a holey carbon film was performed. This sample and magnification was selected to have a high contrast and to minimize the effect of drift since the individual 100 ns scans have such a low SNR that aligning them would be very challenging and beyond the scope of the present study. First a 1024×1024 scan at a 20 μs dwell time was performed, the bright field (BF) and dark field (DF) images are shown in Fig. 4.9(b,f). The virtual detectors used to reconstruct the signal are shown in Fig. 4.9(a,e) where the BF signal arises from the integration over the entire central beam, which is a different definition then shown in *Section 2.1.2*, and the DF collects all the signal which lands outside the central beam. Further the same FOV is scanned with the same number of probe positions except the dwell time is decreased to 100 ns where a total of 200 frames were scanned to have an equal dose as the slower 20 μs scan. The resulting summed BF and DF are shown in Fig. 4.9(c,g). Large distortions due to the finite response of the scan coils are visible but in essence, the 4D STEM signal is recorded properly showing that the detector can handle such short dwell times with ease. In Fig. 4.9(d,h) the BF and DF of a single scan are shown where the low SNR results from the very small number of counts per probe position. These results show that even shorter dwell times would be possible if the scanning system bandwidth could be improved, possibly at the expense of maximum FOV capabilities. Efforts in this direction are reported for magnetic deflection [188] but also electrostatic deflection coupled to high bandwidth amplifiers are a possibility.

4.4.3. Declustering Events

The identification of clusters can be used to increase the modulation transfer function (MTF) of the detector as shown in the work of van Schayck *et al.* [178] where they trained a neural network to better estimate the point of initial impact. However for our work such increasing of the MTF are expected not to greatly modify the result of the reconstructed images since the

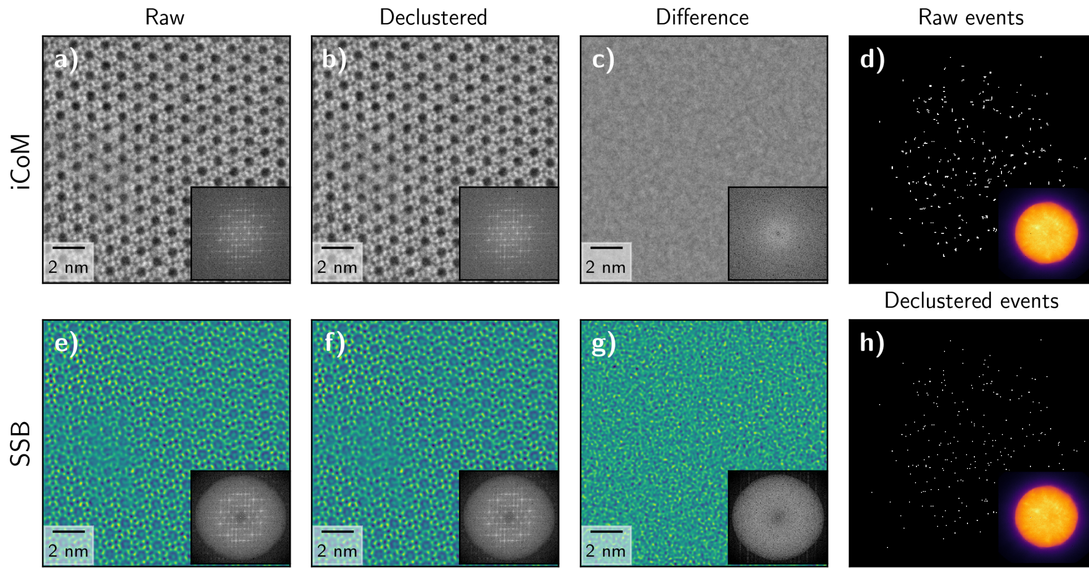

Figure 4.10.: **(a)** The reconstructed iCoM image of the raw dataset from a silicalite-1 zeolite. The scan size is 1024×1024, the dwell time is 6 μs, and the acceleration voltage is 200 kV. In the insets the Fourier transform of the iCoM signal is shown. **(b)** The same as (a) except declustering is applied. **(c)** The difference between (a) and (b) showing the similarity between the two signals. **e-g** The raw, declustered and difference SSB reconstruction. **(d)** a set of 500 sequential events from the same dataset detected on the Timepix3 camera, in which the declustered event is clearly seen. In the inset the PACBED pattern is shown. The power spectrum of each image is shown in the inset. **(h)** The same as (d) but now with declustering applied.

algorithms used to reconstruct the signal are not very sensitive to this [164, 165].

The influence on the declustering is checked on a 1024×1024 scan using a 200 kV acceleration voltage with a dwell time of 6 μs where the sample is zeolite silicalite-1. The declustering algorithm searches for adjacent pixels which are excited within a time interval of 100 ns [178]. From this cluster the new corrected time-of-arrival (TOA) is when the first pixel of the cluster is

excited. The point of impact is calculated using the centre-of-mass of the cluster. In Fig. 4.10(a,b), respectively, the raw and declustered reconstructed iCoM images are shown and seen to be very similar. The difference between the two signals is shown in Fig. 4.10(c), showing that for iCoM the reduction of modulation transfer function (MTF) has no visual influence on the result. The average value of the difference is 1%. The same procedure for the SSB reconstruction is performed which is shown in Fig. 4.10(e-g). From the difference between the raw and declustered reconstructions it is seen that when the aim is to extract the atomic positions, the raw signal performs adequate. However, when quantitative information is desired from the iCOM and SSB signal, declustering is expected to improve the results.

4.4.4. Minimal dose for reconstruction

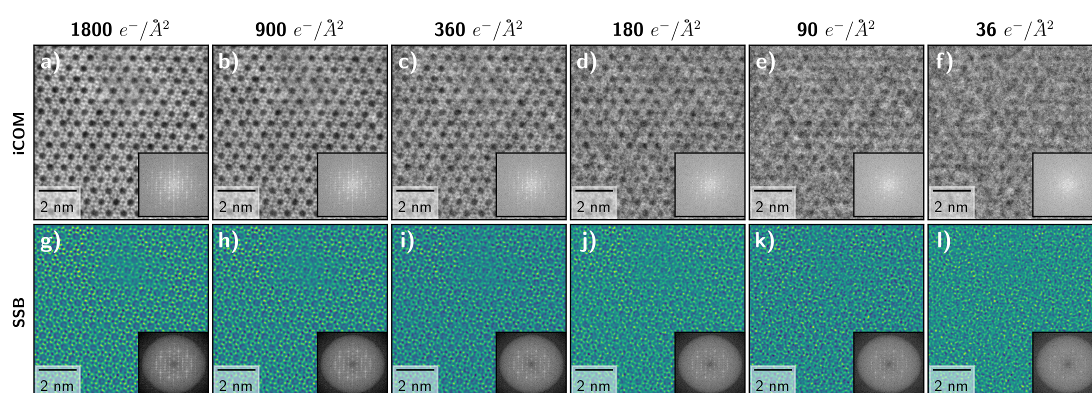

Figure 4.11.: **(a-f)** The iCOM reconstructed signal from the 1024 × 1024 scan at 6 μs on the SI-1 zeolite using 200 kV. The total dose used to reconstruct the signal is shown in the title. **(g-l)** The reconstructed SSB signal. The power spectrum of each image is shown in the inset.

It is relatively easy to investigate how the iCOM and SSB reconstruction are influenced by the number of events since the individual electron events are recorded during the acquisition. This gives information on the minimal dose needed to still capture a reasonable image. The

definition of reasonable depends on which features are of interest for the researcher. In Fig. 4.11 the iCOM and SSB reconstruction for a 1024×1024 scan at 6μs are shown. The sample was the SI1-zeolite and the acceleration was 200 kV. The total dose when using 100% of the electrons was 1800 $e^{-}Å^{-2}$. The total dose of each reconstruction is shown in the title of each image. In order to chose which events to keep, a random number generator was used to select a subset of events corresponding to the percentage indicated. From Fig. 4.11 it is clear that when using only a dose 180 $e^{-}Å^{-2}$) of the electrons the reconstructed signals still show the high resolution features however when removing more electrons these features start to disappear. This prior knowledge can be used to investigate at how the resolution deteriorates with lower the total dose and a minimal dose needed can be determined.

4.5. Discussion

Due to the speed at which full 4D STEM data sets can now be recorded with event-based detectors, this technique has the capability to be combined with other conventional high resolution STEM (HR-STEM) methods. For instance, tomographic series can be performed where instead of just the HAADF signal, the full diffraction pattern can be recorded where a large range of scattering angles is available. In fact it would be a pity to not record this rich dataset if all we need to trade in is more storage space. In the post-processing steps, different signals can be reconstructed to increase the information gathered from the experiment [189] with the potential for even online processing of the datastream [190].

Another method that becomes more attractive for 4D STEM is depth sectioning, where instead of the simple fixed focus multi-frame acquisition used in this work, were the focus is changed between every subsequent scan in order to get three dimensional information about sample [191–195]. Adding the 4D STEM dataset to such optical sectioning could potentially improve its performance where for instance for S-matrix reconstruction this depth sectioning is necessary [196]. Finally, acquiring 4D STEM data when the scan sequence is changed is easily accessible if one knows at each time where the probe is positioned. These different scanning

strategies are used e.g. to decrease damage [197, 198], or distortions [199, 200].

Although the main limit of the current Timepix3 camera is its limited dose rate, new plans for a Timepix4 chip have been revealed where the number of pixels almost quadruples to 512×448 and the maximum dose rate increases with a factor of six. This allows for a current increase by approximately a factor of 24 bringing it, in the coming years, much more in line with conventional beam currents used in STEM imaging [201].

4.6. Conclusion

In this chapter, it is shown that using a hybrid pixel direct electron event-based detector rather than conventional frame-based cameras enables the recording of 4D STEM datasets with dwell times as low as 100 ns. The detector was characterised at two different acceleration voltages, 60 and 200 kV. For 200 kV, the maximum electron count rate is half that of 60 kV. However when increasing the threshold for 60 kV, a significant decrease in collection efficiency is observed. Hence when performing experiments, a compromise on the threshold is required where the higher the threshold, the higher the electron dose rate that can be detected. However this decreases the collection efficiency which is detrimental for beam sensitive materials. Furthermore, by synchronizing the detector with a versatile scan engine, multi-frame 4D STEM acquisitions could be performed with scan sizes of 1024×1024 or larger using dwell times in the order of μs. This opens up the possibility to always perform 4D STEM acquisition instead of conventional STEM and profit from the significantly higher information content about the sample for the same incoming beam current. In the future, we anticipate improvements in both the data processing times and the maximum count rates detectable by event-based detectors to make this type of setup become the de-facto standard for STEM imaging.

5. Event Driven Coincidence Detection in Transmission Electron Microscopy

This chapter is based on:

D. Jannis, K. Müller-Caspary, A. Béché, A. Oelsner, J. Verbeeck, *Spectroscopic coincidence experiments in transmission electron microscopy.* Appl. Phys. Lett. 114, 143101 (2019); DOI: 10.1063/1.5092945

and

D. Jannis, K. Müller-Caspary, A. Béché, J. Verbeeck, *Coincidence detection of EELS and EDX spectral events in the electron microscope*, Applied sciences (2021); DOI:10.1038/s41699-021-00258-5

5.1. Introduction

In TEM there are two frequently used spectroscopic methods which are EELS and EDX (see *Section 2.2*). Both methods can be applied in parallel, scanning a sub-angstrom probe over the specimen and collecting both EELS and EDX spectra simultaneously. Algorithms are then applied to correlate this multi-detector signal, sometimes together with e.g. the HAADF signal, into a meaningful representation of the details of the specimen [202]. As much as this field is in development, an important factor is missed in this process: the excitation (EELS) and de-excitation (EDX) are intrinsically coupled and are expected to take place in very close temporal succession [203, 204]. The idea of observing these temporal correlations has been applied by Kruit *et al.* making use of real time event filtering with mixed digital/analog electronics [205], imposing a predetermined energy window on the EELS or EDX.

We expand on this idea with an updated setup that is capable of digitally storing all detected events together with their TOA. This setup keeps all detected events and allows for much more extensive post processing while using a detector setup that is less complicated profiting from advances in high speed digital electronics since the 1980-ies. Since EELS and EDX both probe the same process, one could infer that no extra information would be gained by measuring the temporal correlation between the two signals. However, there are clear distinctions between both methods that are partly technological and partly physical. A technological limitation is the limited energy resolution of current EDX detectors, hiding fine details that would provide bonding information. EELS suffers from the presence of a background signal which poses a physical limit. Indeed, this background comes with its own counting noise which can, in many cases, swamp the signal of interest from e.g. a low concentration element in a sample [17, 206].

In this chapter, we begin with the description of two different coincidence setups which were used to measure the individual electrons and x-rays with nanosecond resolution. After this, the equations describing the coincidence experiments are given to provide insight in the performance gains and the role of the instrumental parameters in comparison to conventional EELS and EDX setups. Next, the results from the first preliminary experiments, using the DLD,

are discussed. Furthermore, a novel method for collection efficiency measurement omitting the need for a reference sample is described. Additionally, the influence on the coincidence measurement when varying the electron beam current is investigated and the performance of model free background subtraction in EELS and EDX is demonstrated. Subsequently, a statistical analysis of the SNR demonstrates how coincidence counting provides superior results over conventional EELS and EDX for cases with low signal to background and/or low beam current, making the method ideal for extending the capabilities of analytical TEM for trace element analysis. Finally, the current limitations in time resolution of the setup are described and possible ways for improvement are discussed.

5.2. Experimental Setup

The first aim was to develop a setup which was able to record the temporal correlation between the inelastic electron and x-rays. Once it was verified that the proof of principle worked, the experimental setup was modified to improve the overall performance of the setup. In this section, both setups will be described. For both setups, a FEI Tecnai Osiris microscope was used which was equipped with a Super-X EDX detector [207] and a Gatan Imaging Filter (GIF 200). The EDX detection setup consists of four SDD providing a collection solid angle of approximately 0.7 sr.

5.2.1. Setup: DLD

The first setup used a DLD to detect the electrons which was placed at the back end of the GIF 200 such that the electrons are dispersed and the EEL spectrum can be measured. The readout system of the DLD has a timing resolution of ~30 ps which is more than sufficient to reveal the coincidence information. For the EDX setup, only two of four detectors were used due to limitations in our current hardware setup.

In Fig. 5.1, a sketch of the coincidence detection setup is shown, depicting the excitation via

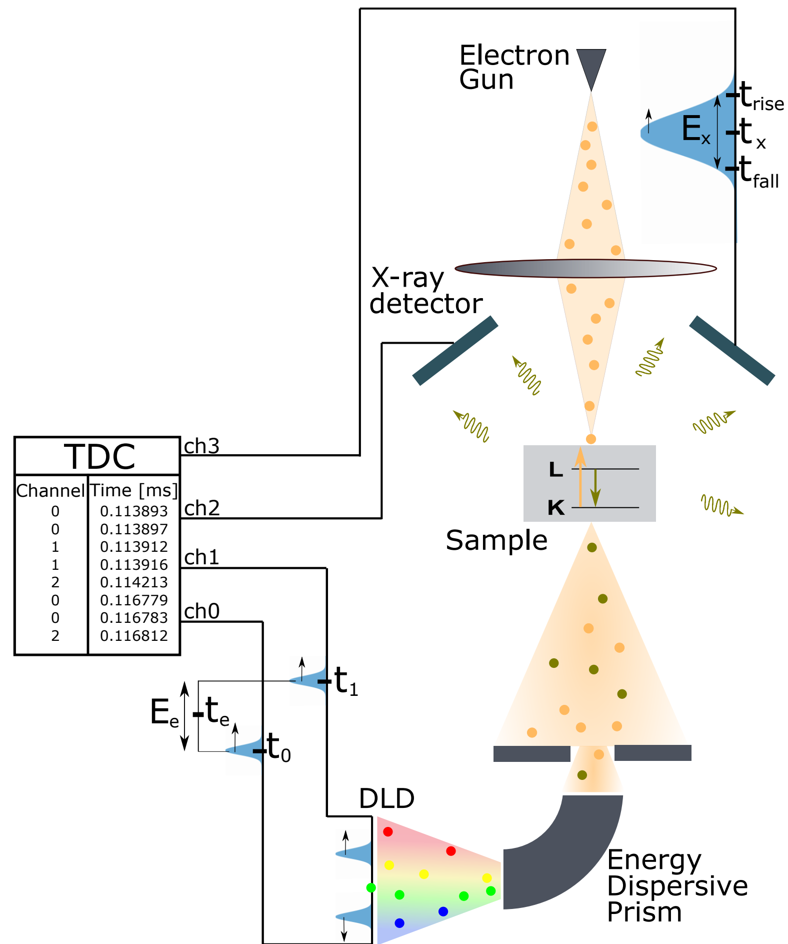

Figure 5.1.: Sketch of the implemented coincidence detection setup using the DLD. The incoming electron creates a inner-shell excitation which decays, emitting an x-ray. The correlated x-rays and electrons are indicated with the same color. Both events (electrons and x-rays) are detected and their energy and time of occurrence are determined after processing the data stream of the TDC.

inelastic electron scattering to an atom in the specimen which undergoes a core-level ionization. Next, the excited atom can decay by emitting an x-ray while filling up the vacancy created in the EEL event. The electron and x-ray are detected by the DLD and SDD, respectively. In order to measure the arrival time and energy of the EDX signal, we use a comparator circuit to the two (out of four) analog outputs of the pulse shaping hardware of the SDD in order to record the rising and falling edge of this pulse through external inputs on the time-to-digital converter (TDC). Since we use the output of the pulse shaping hardware, the pulse will have a more or less Gaussian shape (see Fig. 5.1) which is different from the output signal from the detector (step function). The energy of the x-ray will be proportional to the width of the pulse since normally the energy is determined from the amplitude of the pulse.

The data acquired during the experiment is a list of two columns. The first column stores the channel and the second one stores the time when this channel was triggered. In this experiment four channels where used. Two channels (0 and 1) detect the pulses coming from the delay-line detector (DLD) and the other two (2 and 3) are from two EDX detectors. The channel is triggered on the leading and falling edge of the incoming pulse (illustrated in Fig. 5.1). This procedure leads to the data stream shown in Fig. 5.2. The internal (reference) clock has a maximum of 125 ms, therefore every time the counter wraps around, the wrap around time is added to the rest of the data stream to have absolute time stamping of the channels. In Fig. 5.2 the detection of one x-ray is shown (indicated by channel 3). The energy ($\mathrm{E_{EDX}}$) and time of arrival ($\mathrm{t_{EDX}}$) of this event is calculated as following:

$$\mathrm{E_{EDX}} \propto t_{3,fall} - t_{3,rise} \tag{5.1}$$

$$\mathrm{t_{EDX}} = \frac{t_{3,fall} + t_{3,rise}}{2} \tag{5.2}$$

The TOA is chosen to be in the middle of the pulse. Other possibilities for TOA such as leading or falling edge of the pulse were investigated but this results in energy dependent TOA. This is because the time at which the processed pulse exceeds or drops below the comparator value depends on the height of the pulse, hence its energy. When taking both the rising and falling

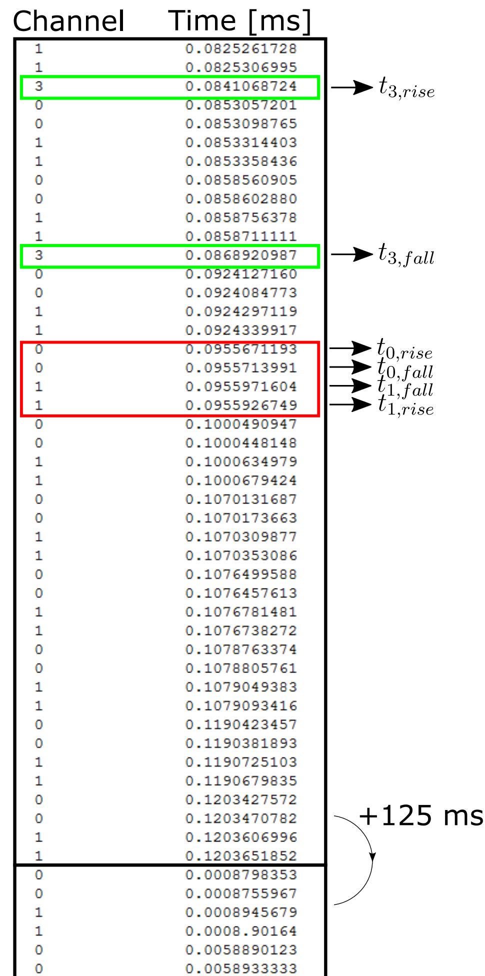

Channel	Time [ms]
1	0.0825261728
1	0.0825306995
3	0.0841068724
0	0.0853057201
0	0.0853098765
1	0.0853314403
1	0.0853358436
0	0.0858560905
0	0.0858602880
1	0.0858756378
1	0.0858711111
3	0.0868920987
0	0.0924127160
0	0.0924084773
1	0.0924297119
1	0.0924339917
0	0.0955671193
0	0.0955713991
1	0.0955971604
1	0.0955926749
0	0.1000490947
0	0.1000448148
1	0.1000634979
1	0.1000679424
0	0.1070131687
0	0.1070173663
1	0.1070309877
1	0.1070353086
0	0.1076499588
0	0.1076457613
1	0.1076781481
1	0.1076738272
0	0.1078763374
0	0.1078805761
1	0.1079049383
1	0.1079093416
0	0.1190423457
0	0.1190381893
1	0.1190725103
1	0.1190679835
0	0.1203427572
0	0.1203470782
1	0.1203606996
1	0.1203651852
0	0.0008798353
0	0.0008755967
1	0.0008945679
1	0.0008.90164
0	0.0058890123
0	0.0058933333

Figure 5.2.: A small part of the data stream measured during the experiment. In this part of the data stream one x-ray is detected (channel 3) and the rest are electrons. The internal clock has a wrap around of 125 ms as shown in the data stream.

edge into account, the energy dependence on the TOA is leveled out. The other events in Fig. 5.2 originate from the DLD detector. In this case two pulses are detected with both a leading and falling edge. The energy (E_{EELS}) and time of arrival (t_{EELS}) of the electron event are calculated as follows:

$$E_{EELS} \propto \frac{t_{1,fall} + t_{1,rise} - t_{0,fall} - t_{0,rise}}{2} \tag{5.3}$$

$$t_{EELS} = \frac{t_{1,fall} + t_{1,rise} + t_{0,fall} + t_{0,rise}}{4} \tag{5.4}$$

The processed dataset then contains the energy of the events and the TOA. This dataset and the related data treatment can be found at [208].

Using this experimental setup, the energy and arrival time is obtained and stored for every detected electron (E_e, t_e) and x-ray (E_x, t_x). In order to obtain information on the time correlation, the time differences between EELS and EDX events are important, not the absolute arrival time of the events. Therefore for every EEL event, the time difference is calculated between this EEL event and every EDX event. However, only time differences in the interval of [-20 ,20] μs are kept since any correlation is expected to occur almost instantaneous and well inside this timing interval. For every time difference, the corresponding energies of the EEL and EDX are also stored as a list consisting of EEL energy, EDX energy and time difference (Δt) between these two events (E_e, E_x, Δt).

5.2.2. Setup: Timepix3

The coincidence setup using the DLD was able to measure the time correlation between the electrons and x-rays (see *Section 5.4*). However there were some disadvantages coupled to the setup. Firstly, only two of the four x-ray detectors were used during the acquisition so the collection efficiency of the EDX setup could be doubled by using all four of them. Furthermore, the energy determination of the x-ray via the use of the comparator circuit is not the optimal method in terms of energy resolution. These issues where solved by using a DPP [209] which can output the TOA and energy of the incoming x-rays. The sampling interval of the AD converters

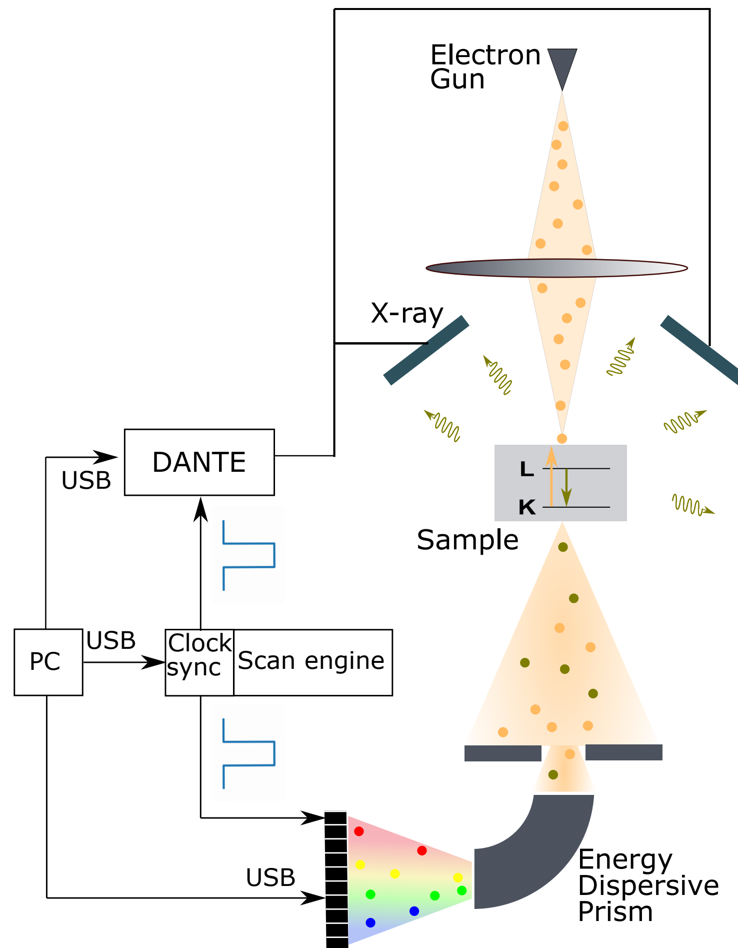

Figure 5.3.: Sketch of the implemented coincidence detection setup. The incoming electron creates a inner-shell excitation which decays, emitting an x-ray. The correlated x-rays and electrons are indicated with the same color. The electron detector used is the Timepix3. The TOA and energy of the x-rays are measured using the DANTE DPP. A synchronization signal between the detectors is send by the scan engine which also gives freedom to scan the beam over the sample to perform coincidence mapping. Python scripting was used to control the detectors and scan engine in an automated manner.

on the 8 input channels is 8 ns which forms an lower limit for the time resolution. However, as will be shown in *Section 5.4.7*, the limit on the time resolution is currently dominated by the x-ray detector response time and well above this 8 ns sampling rate. The DLD was able to detect the TOA of the electrons but it had some drawbacks where a gain reference was needed, the detector was quite susceptible to electron beam damage and the apparent number of pixels was quite limited (100 × 100). Therefore, the DLD was replaced with the Advapix Minipix TPX3 camera [173] which we selected for its size fitting the dimension of a custom-developed retractable mount sliding into the original video camera port of the GIF. Furthermore, a versatile scan engine [135] is hooked up to the microscope in order to synchronize the timing of the electron and x-ray signals with the scanning of the electron probe. To this end, the scan engine sends a trigger signal to both the electron detector and the x-ray pulse processor to start the acquisition. Since the devices use different clocks, synchronization signals are send out every 200 μs to prevent the clocks from drifting too much with respect to each other and with respect to the scan sequence. Thanks to the open Python API of both external scan engine, DPP and Minipix detector, a fully automated measurement scheme can be set up conveniently.

In this work, two different types of acquisition are used. One is the static beam where we acquire only one x-ray and EEL spectrum. The other one is the mapping configuration where we scan the beam over the sample while recording EELS and EDX spectral data as an event stream. Since the TOA of every event is stored and synchronised to the scan engine, the position of the probe for every event can be determined. Note that because of this event-based detection, the limit on scan speed is only determined by the scan engine and scan coil system response time. The methodology to recreate the EELS and EDX maps is similar to the method described in *Chapter 4* where a Timepix3 camera is used to retrieve the 4D STEM datasets at μs speeds. When the coincidence mapping is performed, multi-frame scanning is used to minimize the effects of drift by providing the ability to align the multiple scan frames in software. For every acquisition, the camera length is reduced to the minimum and the largest 3 mm GIF aperture is chosen giving an estimated collection angle of 20 mrad in an attempt to maximise the collection efficiency of the electron detection.

After the data collection, the data processing is performed in a similar manner as for the previous setup. Hence, from the individual electron and x-ray events, coincidence events are created by coupling every x-ray with the electrons which arrive within a time window of 20 μs resulting in the same list containing (E_e, E_x, Δt). When the probe is scanned over the sample during the acquisition, three more components indicating the position of the probe (x_p and y_p) and the frame number (n_f) are added to the list (E_e, E_x, Δt, x_p, y_p, n_f). During the acquisition which could take up to one hour, the sample tends to drift. This drift between the frames was estimated and corrected using open-source software which utilizes all possible combinations of image correlations [184]. The rest of the data processing is done by self-written python software. The full datasets and software are made available on Zenodo.

5.3. Theoretical Description

In order to understand the number of coincidence events, we start with the description of the detected counts for a conventional EELS and EDX setup. We assume that the inelastic electrons which fall onto the detector can be described by one core-loss edge ($N_{e,e}$) and a background signal ($N_{e,b}$) which are described in Eq. 2.16 and Eq 2.17. The number of detected electrons on the detector (N_{EEL}), when assuming an ideal detector, covering a certain energy range Δ is then given by following equation [80]:

$$N_{EEL} = N_{e,e} + N_{e,b} = (C \cdot \sigma + B_e) \cdot \epsilon_e I \cdot t \tag{5.5}$$

Note that the notation of $\sigma(\beta, \Delta)$ has been changed to σ to make the notation easier. For x-ray detection, the same reasoning can be applied to formulate the number of x-rays detected (N_{EDX}) where $N_{x,e}$ and $N_{x,b}$ are described by Eq. 2.20 and Eq 2.21 respectively giving following result :

$$N_{EDX} = N_{x,e} + N_{x,b} = (C \cdot \sigma_T \cdot \omega + B_x) \cdot \epsilon_x I \cdot t \tag{5.6}$$

The difference between σ and σ_T is that for x-rays the total cross section is used while for the electron detection not all inelastic electrons arising from a particular edge are detected

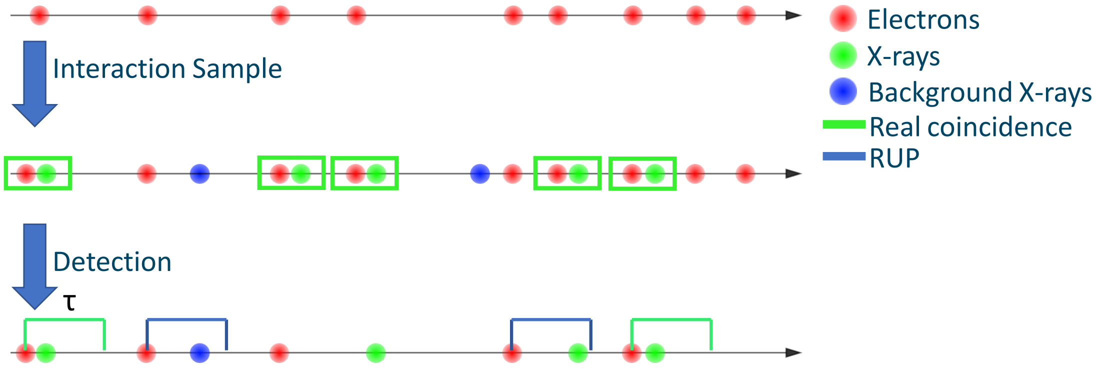

Figure 5.4.: Schematic view on the origin of the RUP where the electrons are emitted from the gun in a Poisson process. Next, the electrons interact with the specimen creating correlated electrons and x-rays (green). Moreover, there are also non-correlated x-rays created during the interaction with the incoming electrons. The last step is the detection step where due to the non-ideal collection efficiency and finite time resolution, there is a finite probability that non-correlated processes are identified as being correlated since they occur within the time coincidence window τ.

due to the limited energy field of view (Δ) and collection angle (β). A coincidence event is detected when both an electron and an x-ray is detected at the 'same' time. Hence the number of coincidence events is given by the following equation:

$$N_C = C \cdot \epsilon_x \cdot \epsilon_e \cdot \omega \cdot \sigma \cdot I \cdot t \tag{5.7}$$

Note that the background signal B_e and B_x does not take part in the coincidence detection as we assume the background to be caused by unrelated and uncorrelated events. Besides the correlated events, there are uncorrelated events which happens when an electron and an x-ray are detected within a certain time interval even though they posses no underlying correlation. In Fig. 5.4 a schematic view on the origin of the random uncorrelated process (RUP) events is shown. The number of uncorrelated events is the product between N_{EEL} and N_{EDX} which

is time invariant. These RUP have a probability to occur inside the time coincidence window (τ). This window is set by the time resolution of the experimental setup. Hence the number of uncorrelated events occurring inside the time coincidence window is given by

$$N_{RUP} = N_{EEL} \cdot N_{EDX} \cdot \tau = \Big((C \cdot \sigma + B_e) \cdot (C \cdot \sigma_T \cdot \omega + B_x) \Big) \cdot I^2 \cdot \tau \cdot \epsilon_e \epsilon_x t \tag{5.8}$$

From Eq. 5.8 it is clear that the RUP goes as I^2 whereas N_C scales linearly with I. Note also the linear dependence on the time window which is directly related to the time resolution of the event detection system (taking it smaller misses events, taking it larger adds only RUP)

The coincidence technique can also be used to determine the ratio between the areal density of the elements in a similar way is been done for EELS (*Section 2.2.3*) and EDX (*Section 2.3.2*) which results in:

$$\frac{C_A}{C_B} = \frac{\omega_B \sigma_B}{\omega_A \sigma_A} \frac{N_C(A)}{N_C(B)} \tag{5.9}$$

This equation is very similar to Eq. 2.22 where the difference is that for conventional EDX the entire cross section σ_T is used whereas for coincidence only the part of the cross section which is detected on the electron detector is used.

From Eq. 5.7 and Eq. 5.8, an SNR can be determined which describes if the coincidence events are statistically significant. Since this is fundamentally a Poisson process [1], the standard deviation of this signal is given by its square root. The SNR of the coincidence setup (SNR_C) when acquiring for exposure time t is given by following equation:

$$SNR_C = \frac{N_C \cdot \sqrt{t}}{\sqrt{N_{RUP} + N_C}} \tag{5.10}$$

$$SNR_C = \frac{C\omega\sigma \cdot \sqrt{I \cdot \epsilon_e \epsilon_x \cdot t}}{\sqrt{(C\sigma + B_e) \cdot (C\sigma_T \omega + B_x) \cdot \tau \cdot I + C\omega\sigma}} \tag{5.11}$$

[1] Multiple detected events can be triggered for a single arriving electron or X-ray, but this is dealt with in a discrimination stage in the detector, leading to a stream of pure Poisson single detection events.

where the signal of interest is the total number of detected coincidence events. Using Eq. 5.10 we can determine how the incoming current influences the SNR and if there is a optimal current to perform the coincidence experiments. Eq. 5.11 as a function of I can be reduced to:

$$SNR_C(I) = a\sqrt{\frac{I}{bI + c}} \tag{5.12}$$

where a, b and c are the multiplicative constants which makes the notation easier. Eq. 5.12 is a monotonic increasing function. Hence when performing experiments, maximizing the current maximizes the SNR which also applies for conventional EELS or EDX. However, in the limit of infinite current, the SNR converges to $a/\sqrt{b}$ which indicates that at some point, which depends on the parameters, no gain in SNR is expected by increasing the current. From Eq. 5.12 it is clear that when the aim is to maximize the SNR within a certain fixed time, increasing the current gives the best SNR, which also applies for conventional EELS and EDX. However, increasing the current is not always possible due to the occurrence of electron beam damage for some materials. So instead of maximizing the SNR in a certain time, the total amount of incoming electrons ($N = I \cdot t$) is fixed where the current is left as a free parameter. For conventional EELS and EDX, the SNR only depends on N so taking a very long acquisition with a low current or a short acquisition with a high current results in the same SNR, if the rest of the setup is ideal. On the other hand, for the coincidence experiment this current does play a role in the final SNR. This can be seen by plugging N into Eq. 5.10 and giving the following:

$$SNR_{C,N}(I) = \frac{a'}{\sqrt{bI + c}} \tag{5.13}$$

where it is observed that this function is always monotonically decreasing, hence when maximizing the SNR for a given amount of dose, the current should be as low as possible. This can be understood from the observation that at low current, the probability that two uncorrelated events will be close to each other diminishes rapidly while the correlated events will remain at the same short time interval, making it easier to discriminate between real coincidence events versus unwanted RUP signal. This however has the obvious downside of very long acquisition

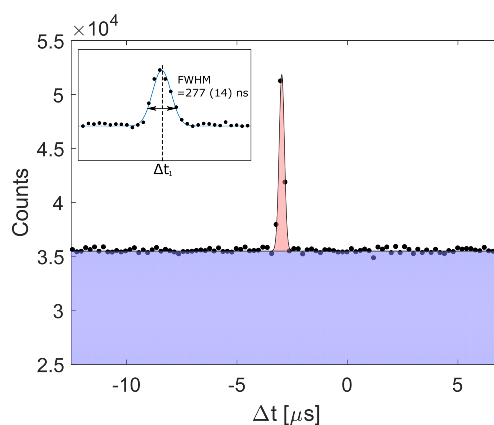

Figure 5.5.: Histogram of the time difference Δt between x-ray and inelastic electron showing a clear temporal correlation (red peak). Uncorrelated events are present as a background (blue). The width of the coincidence peak (inset), is assumed to be predominantly instrumental in nature.

times which would make the experiment more prone to sample drift.

5.4. Results

A multitude of experiments were performed on the time correlation between the electrons and x-rays. In the first section we will show the proof of principle which were obtained using the setup with the DLD and TDC. The rest of the results were obtained using the DPP and Timepix3 detector.

5.4.1. Proof of Principle

As a proof of principle, an Al – Mg – Si – Cu alloy [210] was selected since it has rich features in both EELS and EDX spectra. Furthermore, the alloy is challenging for conventional EELS quantification because of the relatively low abundance of Mg (≈ 0.62 wt%), Si (≈ 1.11 wt%) and

Cu (≈ 0.5 wt%). Additionally, there is the difficulty of detecting Cu from EDX due to multiple sample-unrelated sources of Cu in several components of the microscope and the supporting grid. We will show that both difficulties can be overcome making use of the coincidence information, allowing for improved quantification.

The events classified as (E_e,E_x,Δt) provide all the information needed for observing the time coincidences between the electrons and x-rays. The first step is to verify that at Δt = 0 there is an increase in counts as would be expected if both events are correlated. The histogram of the time difference between EEL and EDX event is given in Fig.5.5 and shows a clear coincidence peak at $\Delta t_1 \approx 3\ \mu$s, corresponding to the inelastic scattering of an electron exciting an atom followed by the decay of the same atom via an x-ray emission process. This histogram is similar to the second order correlation $g^(2)$ which is used to measure the photon bunching [211] and antibunching [212, 213]. The delay of 3 μs was unexpected since the duration of the inner-shell excitation and de-excitation by x-ray emission is expected to be in the order of femtoseconds [214]. This time delay is likely due to the analog pulse shaping process of the EDX signal and can further be ignored as an offset that does not influence the analysis. The width of the peak in Fig.5.5 is related to the time selectivity τ of the coincidence setup which is estimated here to be 277±14 ns. In *Section 5.4.7* it is shown that the uncertainty in TOA arises from the drift time in the SDD detector. In addition to the coincidence peak there is a relatively large unspecific background which originates from random uncorrelated processes (RUP) happening inside a given time interval which can be described by Eq. 5.8. We can estimate this RUP signal quite accurately by measuring all events outside the coincidence window since their count rate is independent on the time difference (Δt).

Fig. 5.6(a) and (b) shows the conventional EEL and EDX spectrum of the alloy sample respectively. In the EDX spectrum, the characteristic x-ray energy windows from different atoms (K_α(Al), K_α(Mg), L_α(Cu)) are marked. In Fig. 5.6(e-f) EEL events are represented as a function of energy loss and time difference when different energy windows of x-ray energies are selected. We observe that at Δt_1 the element specific signal increases significantly, depending on the selected x-ray energy window. This already shows the potential and selectivity of the technique

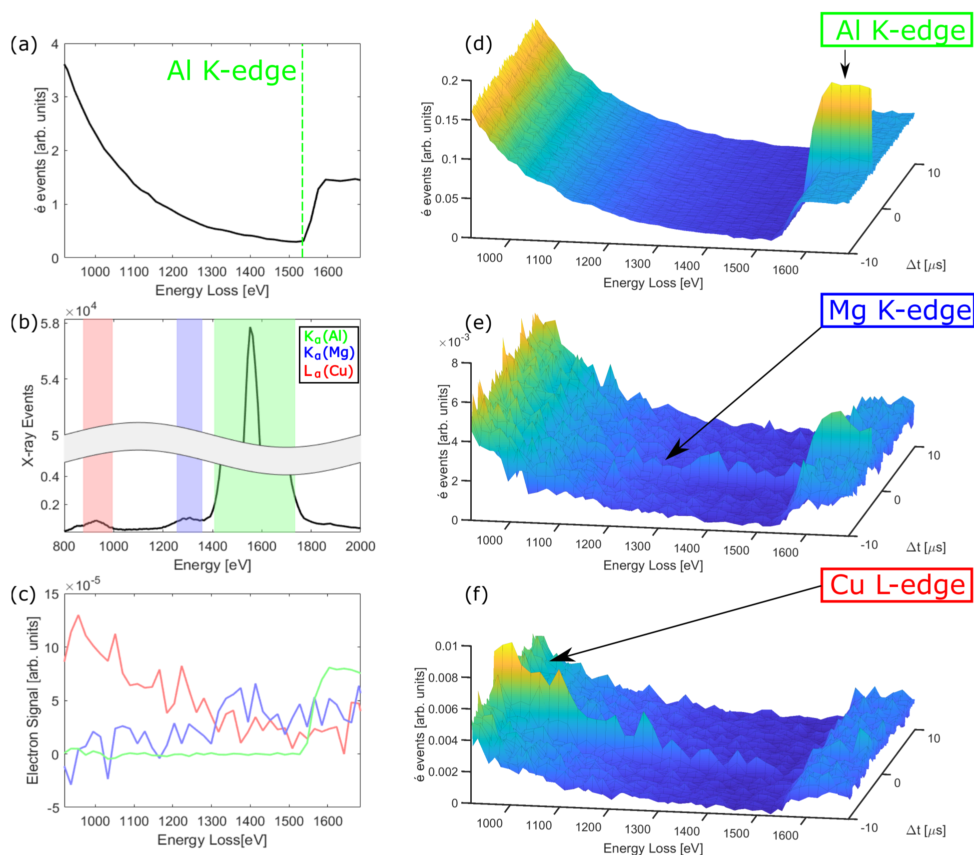

Figure 5.6.: **(a)**The EEL spectrum of the Al-Mg-Si-Cu alloy where the aluminium K-edge is indicated. **(b)** The x-ray spectrum where three X-rays originating from different atoms are marked. **(d-f)** The post selection of electron events, when different energy windows of x-ray energies are selected, as a function of the electron energy loss and time difference between the x-ray and electron event. The selected energy windows correspond to the characteristic x-ray energies of the different atoms (Al, Mg, Cu) present in the sample. It is clear that at a particular time difference there is a increase in signal. This increased signal corresponds to the core-level ionization event followed by x-ray emission with an energy inside the selected window. **(c)** The RUP subtracted coincidence EEL spectra for the different elements where the colour-code is identical as for figure (b).

as also the very weak Cu L-edge and Mg K-edge are appearing while they are totally indistinguishable from the background in Fig. 5.6(a). Furthermore, the signal outside Δt_1 is constant as a function of time difference which is expected because these RUP events have no correlation in time. This means that the signal inside the time coincidence window can be thought of as the sum between the RUP events and the true correlated events. Additionally, since the electron energy distribution of the RUP events is known accurately due to the high statistics, this signal can be scaled and subtracted from the signal inside the time coincidence window.

As a result, only the true core-level ionization events remain as demonstrated in Fig. 5.6(c) while the background signal is entirely removed. This background removal is very attractive as compared to conventional extrapolation of a power law function from a fitting region before the edge. Here we need no fitting region, no assumptions on the shape of the background and we do not suffer from extrapolation errors that can easily become larger than the edge signal for low-concentration elements.

In order to demonstrate this, we compare conventional quantification making use of such an extrapolated background with results obtained when using coincidence as described above. The conventional EELS and EDX signals are used to get quantitative results on C_{Mg}/C_{Al} and C_{Cu}/C_{Al}. The methods used for both EELS and EDX are both described in *Section 2.2.3* and *Section 2.2.3* respectively. Additionally, the coincidence method can be used to get the same ratios using Eq. 5.9 where the result of the three different methods are shown in Table 5.1. The Hartree-Slater cross sections were used in the determination of the ratios. The values for the coincidence setup have a markedly better precision and agree with the values obtained by Lipeng et al. using different methods [210]. This demonstrates that coincidence detection of EELS and EDX provides a substantial advantage over conventional EELS as it allows to selectively boost the SNR for specific excitation edges, revealing a much better detectability, especially for weak edges, while avoiding the conventional background fitting and removal step. This means that here we can even quantify the Cu L-edge although the spectrum contains no energies prior to the edge and therefore conventional quantification is entirely impossible. Compared to EDX quantification, the coincidence technique has the benefit that no unwanted fluorescence signal

Element	Coincidence	EDX	EELS
C_{Cu}/C_{Al}	2.65± 0.07	3.0±0.3	not possible
C_{Mg}/C_{Al}	0.61± 0.04	1.42±0.08	7.45±0.5

Table 5.1.: Areal density ratio of magnesium and copper in the aluminum alloy matrix obtained with coincidence detection and compared to conventional quantification of EDX and EELS.

is present as such x-ray events would not be accompanied by the required EEL event to obtain coincidence. This solves a major issue in conventional EDX quantification and is especially important for Cu here.

5.4.2. Collection efficiency EELS and EDX

The rest of the results shown in this chapter are recorded with the setup using using the DPP and Timepix detector. The coincidence setup gives the ability to get the collection efficiencies for the EELS and EDX setup. This is possible if the background signals B_e and B_x are known. For EELS knowledge on B_e is obtained via a power-law fitting such that only the electrons arising from the core-loss remain ($N_{e,e}$). For EDX, B_x is in general relatively small and consists out of overlapping characteristic x-rays and a continuum which can removed using the methods discussed in *Section 2.3.2.* When both background values can be estimated, the collection efficiency of an EELS setup can be determined by taking the ratio of Eq. 5.7 and Eq. 2.20 which gives:

$$\epsilon_e = \frac{N_C}{N_{x,e}} \frac{\sigma_T}{\sigma} \quad (5.14)$$

The ratio σ_T/σ is determined by the considered energy window of the edge and the collection angle of the EELS setup. The collection efficiency of the EDX setup is determined by taking the ratio of Eq. 5.7 and Eq. 5.5:

$$\epsilon_x = \frac{N_C}{\omega N_{e,e}} \quad (5.15)$$

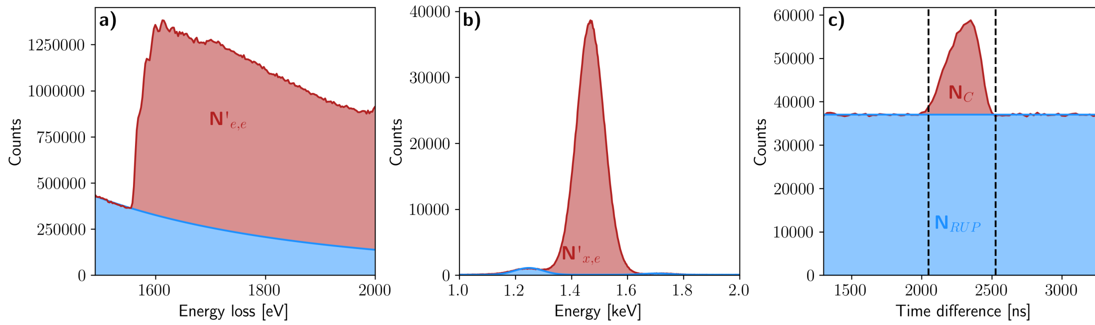

Figure 5.7.: **(a)** Conventional EEL spectrum where the K edge of aluminium is shown from an Al-Mg-SiCu alloy. The background is subtracted using power-law fit (blue area). The background is used to determine $N_{e,e}$. **(b)** The conventional EDX spectrum where the main peak is a characteristic peak of aluminium. The background value is determined by fitting the spectrum to the sum of three Gaussians and a linear slope from which one Gaussian peak is the peak of interest. **(c)** Histogram of the number of correlated events as a function of time difference between the x-rays and electrons. The number of identified coincidence events N_C is indicated on the figure.

from which the fluorescence yield should be known to determine ϵ_x.

This method was used to determine the collection efficiencies of the experimental setup used in this chapter using an Al-Mg-Si-Cu alloy as an example [210]. In Fig. 5.7(a), the conventional EEL spectrum is shown where $N_{e,e}$ is standardly determined by subtracting the background events from the signal where the background is determined by fitting a power-law before the edge onset. $N_{x,e}$ (see Fig. 5.7 (b)) is determined by fitting the EDX spectrum with the sum of three Gaussian and a linear slope where one Gaussian contains the characteristic aluminium peak. The other characteristic peaks come from low concentration copper and silicon. Finally, N_C is calculated by first determining the time coincidence interval which is indicated on Fig. 5.7(c). The next step is to determine N_{RUP} which is done by taking the average counts outside the coincidence window and multiplying this with the time coincidence window. N_C is then calculated by

subtracting the total number of events inside the time coincidence window by N_{RUP}. From using the three values shown in Fig. 5.7, the collection efficiencies can be determined. The two collection efficiencies are $\epsilon_e = 26\%$ and $\epsilon_x = 4.8\%$. For ϵ_e, a value between 20-50% is expected [80] and for ϵ_x a value of 5.2% is predicted [215]. Compared to the standard methods which are used to determine the collection efficiencies, this method has the benefit that no reference sample is required and knowledge of the beam current is not needed [20].

5.4.3. Influence of Beam Current

In order to validate Eq. 5.7 and 5.8, coincidence measurements have been performed at five different incoming beam currents I on a silicon K-edge in a silicon reference sample. The beam current is measured using the current meter which is connected to the fluorescent screen of the microscope. In Fig. 5.8 (a), the different time coincidence histograms are shown where the RUP is the constant background and the peak reveals the actual coincidence events. The acquisition time is kept constant and the incoming electron current is varied.

Using the method explained in *Section 5.4.2* we extract the N_{RUP} and N_C. In Fig. 5.8 (b,c) N_{RUP} and N_C are plotted as a function of beam current and labelled as non-corrected. By inspecting Fig. 5.8(c) some deviation from the fitted linear curve is seen. The origin of this discrepancy is that the electron detection efficiency (ϵ_e) depends on the beam current which is shown in Fig. 5.8(d). This can be explained by the fact that every individual pixel has a certain dead time during which, in which it can't detect a new event. Hence when the count rate increases, more events are lost since they arrive inside this dead time interval. The method for collection efficiency determination was used to extract ϵ_e at the different incoming beam currents. The values obtained for the efficiency are used to correct the observed N_C and N_{RUP} and in Fig. 5.8(b,c) the corrected values are shown which better approximate the expected linear and quadratic dependencies. From the information on N_C and N_{RUP}, the SNR can be calculated using Eq. 5.10 as shown in Fig. 5.8(e) which theoretically should increase with increasing current (Eq. 5.12). The non-corrected curve shows a decrease in SNR which is due to the loss of

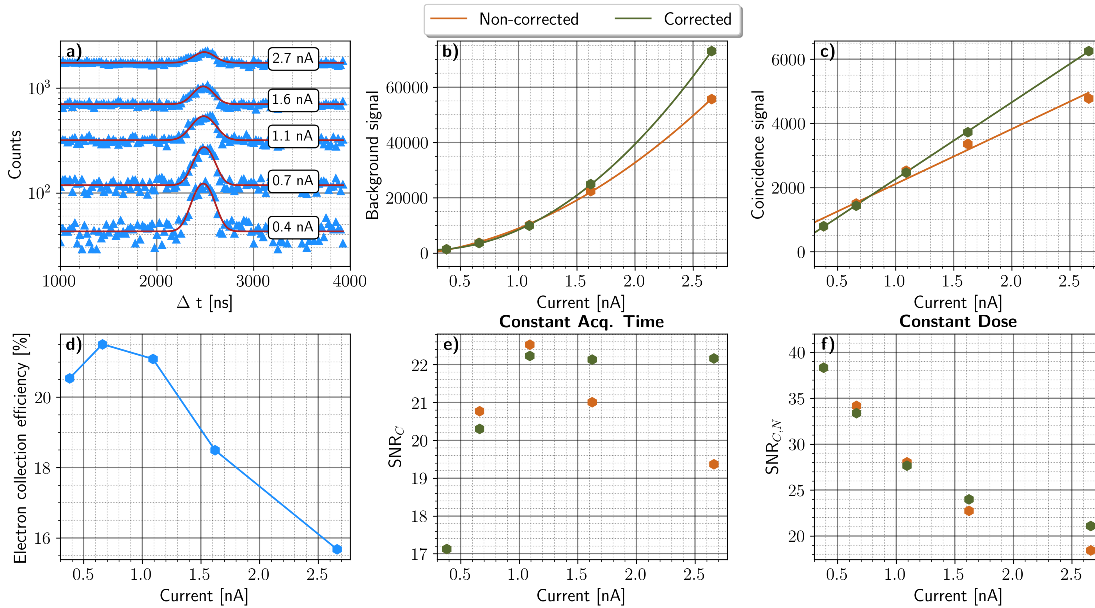

Figure 5.8.: **(a)** Coincidence histograms as a function of time delay between EELS and EDX event streams for a varying beam current at constant acquisition time (y scale logarithmic). A clear improvement of correlation signal vs. background is observed for lower beam currents **(b)** The uncorrelated background signal as a function of incoming beam current (brown)). The background scales quadratically with incoming current. (green) The corrected expected background signal which would be recorded for an ideal electron detector with constant efficiency as a function of current. **(c)** The number of coincidence events as a function of incoming current scales only linearly with incoming current. The corrected signal taking the efficiency into account is shown. Note that the corrected fit better approximates a linear function.**(d)** The measured electron efficiency with a noteable decrease for higher currents due to dead time in the detector. **(e)** The SNR of the coincidence signal as a function of incoming current when using a constant acquisition time. **(f)** The SNR of the coincidence signal as a function of incoming current when the total dose has been fixed.

ϵ_e at higher currents indicating that Eq. 5.12 only holds when the efficiency stays constant as a function of incoming current which for the electron detector used here is not the case. The validity of Eq. 5.12 can still be investigated by incorporating the measured electron efficiency into the SNR which is shown in Fig. 5.8(e) (green) where an increase with current is observed. The validation of Eq. 5.13 is performed by varying the acquisition time such that the product of time and current is constant. The resulting $\text{SNR}_{C,N}$ is shown in Fig. 5.8(f) where, as expected, a decrease of SNR is observed with increasing current implying that when having a fixed dose, the lower the current, the higher the SNR at the expense of acquisition time. Note that this is in strong contrast with conventional EELS or EDX where the SNR depends only on the total dose.

5.4.4. EELS Background subtraction

Contrary to conventional EELS, no prior knowledge on the background signal is needed since the RUP events contain all the information of the background. Indeed the N_{RUP} signal is independent of the time difference between the x-rays and electrons and hence the background signal is approximated very well using all events outside the time coincidence interval [205, 216]. In *Section 5.4.1*, a proof of principle was shown but a clear experimental validation with respect to conventional background subtraction was lacking. Therefore, eight coincidence datasets were recorded where for each set we shift the energy range of the EELS detector by 200 eV. This provides 8 experimental EEL spectra with consecutive energy windows. The incoming current and acquisition time was kept constant over all measurements. The core-loss edge measured is the K edge from Si on a crystalline Si reference sample. In Fig. 5.9 (a), the combined EEL spectrum is given, where each colour indicates a different acquisition and energy window. The black line indicates the fitted background signal which is obtained via power-law fitting where the grey area indicates the fitting region [80]. The background fitting was performed using the Hyperspy open-source software [217]. Fig. 5.9 (b) shows the coincidence EEL spectrum with considerably more noise due to the fact that only a small subset of the EELS events is retained as coincident events (~5%). The background signal (black) is obtained by taking only

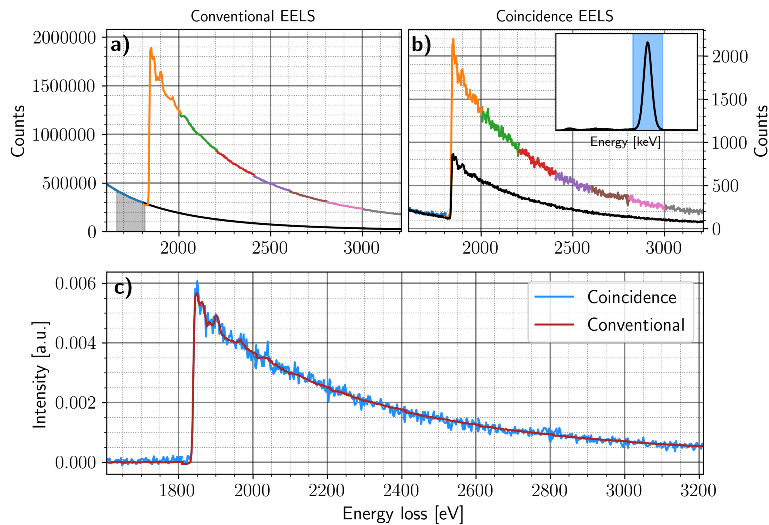

Figure 5.9.: **(a)** Conventional EEL spectrum obtained from eight separate acquisitions in consecutive energy windows. The black line indicates the fitted background using a power law where the fitted area is indicated with the grey area. **(b)** The correlated EEL spectrum when using only electrons which have an Si x-ray detected within the time correlation window. In the inset figure, the x-ray spectrum is shown where the blue area indicates the energy of the x-rays selected which correspond to the x-rays from Si. The black line is the background signal obtained from using the electron outside the time coincidence window. **(c)** The coincidence and conventional background subtracted EEL spectra from which it is seen that the background subtraction method using the correlation with x-rays is able to reproduce the same result as using the conventional power-law subtraction method albeit at the expense of a lower count rate. Note that for the correlated result, no assumptions on background shape and no pre-edge fitting region was required.

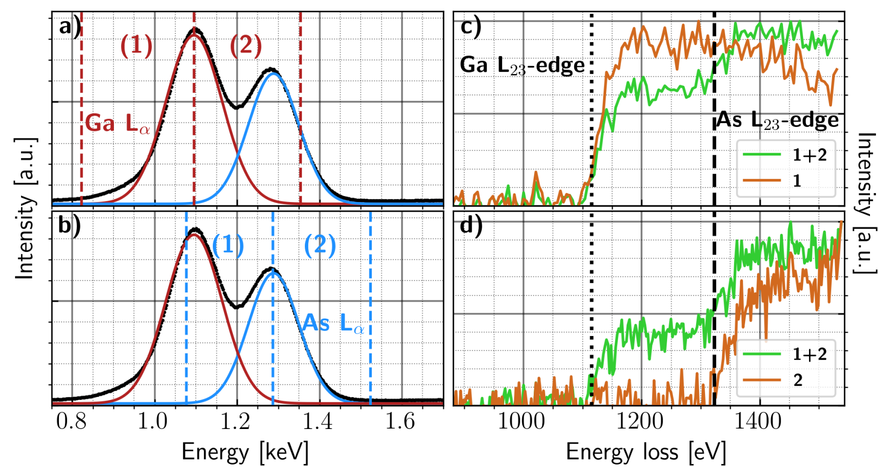

Figure 5.10.: **(a)** The EDX spectrum of GaAs where the Ga peak is fitted with a Gaussian to indicate the extent of the x-rays originating from the de-excitation of the Ga atom. The red and blue line indicates the extent of the x-ray lines in the energy spectrum. **(c)** The background-subtracted EEL spectra using the x-rays in the regions are indicated by the legend. When only using x-rays from *region 1*, it is seen that only the Ga L_{23} edge is selected without the As L_{23} edge (brown). When *regions 1+2* are selected electron from both edges are seen (green). **(c)** The same as (a) only the regions indicated out which the coincidence events are chosen have been changed. **(d)** The background-free EEL spectrum where by selecting the proper x-ray window (*region 2*), only the As L_{23} edge is selected (brown). When *region 1+2* is selected electron from both edges are seen (green).

electrons which do not have a x-ray within the time coincidence interval region ranging from 2200-2600 ns which is chosen to include all the coincidence events inside the interval. In Fig. 5.9 (c), the conventional and coincidence background subtracted EEL spectra are scaled and shown together for comparison. The coincidence method reproduces the result obtained from the standard power-law subtraction method where no significant discrepancy between the two signals is observed. The noise on the coincidence EEL spectrum is considerably larger as the number of detected coincidence events is only 0.1 % compared to the number of detected EEL electrons. This can be explained by comparing Eq. 5.5 and Eq. 5.7 where the number of coincident events is a factor of $\epsilon_x \cdot \omega$ smaller than N_{EEL} where $\epsilon_x \approx 3\%$ and $\omega \approx 5\%$ [218]. At first sight it therefore seems that coincidence background subtraction only leads to the same result with higher noise.

The advantage of the coincidence EEL spectra however, is that no pre-edge was needed in order to subtract the background . This is of fundamental importance when, e.g. core-loss energies of two elements are close to each other preventing a good background fitting region in conventional EELS [90]. This situation also occurs often in the low loss regime, but in this case correlation with cathodoluminescence photons would be required as opposed to the x-rays used here, which would form a highly attractive area for future research as well [219].

Even when x-ray lines are overlapping due to the limited energy resolution of the detectors, the EEL background signal can be correctly subtracted which is shown in Fig. 5.10. In Fig. 5.10 (a) the x-ray spectrum of GaAs semiconductor reference sample is shown, the red and blue line indicates the extent of respectively the Ga L_α line and As L_α line. It is clear that by selecting *region 1+2* in Fig. 5.10 (a) x-rays arising from both the As and Ga atoms are included when creating the background subtracted EEL signal, which is shown in Fig. 5.10 (c), an additional shoulder in the EEL spectrum is visible coming from electrons that scattered inelastically with the As L_{23} edge. In order to remove the electron from the As signal only x-rays with energy in *region 1* are chosen. The same principle can be used to remove the inelastic Ga L_{23} electrons from the As L_{23} edge. This is shown in Fig. 5.10(d) where the spectrum from *region 2* only contains As L_{23} edge electrons. The disadvantage from this method is that a sub selection within

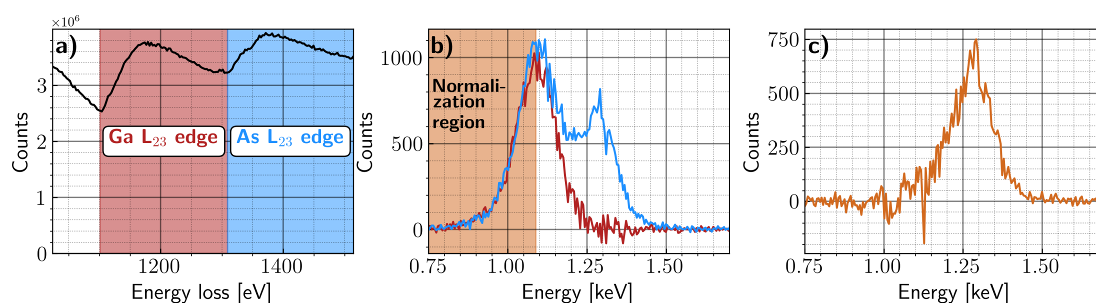

Figure 5.11.: **(a)** The conventional EEL spectrum from GaAs where the two edges are indicated. **(b)** The background-subtracted EDX spectra using only electrons from the two regions indicated in (a). The red spectrum only shows x-rays originating from Ga whereas the blue region shows both Ga and As since the core-loss edges have large tails. **(c)** The As L_α line can be disentangled from the Ga L_α line by normalizing the blue and red spectrum from (b) in the region where only Ga L_α x-rays are present (brown region). The difference between the normalized blue and red spectrum results in an x-ray spectrum containing only the As L_α x-rays.

the x-ray energy window is chosen which gives fewer events hence increasing the noise. The noise will even increase more if the x-ray lines lie closer in energy since there will only be a small window where only one x-ray line will be present.

5.4.5. EDX Background subtraction

The methodology used for background-free EELS can also be applied to EDX spectra. Although the presence of a background signal in EDX is quite limited, there is an issue when due to the poor energy resolution, different peaks start overlapping. The standard method to disentangle these peaks is to use a deconvolution method [20, 96, 97]. However with this method caution should be taken since artefacts can arise [97]. Additionally, system x-rays, such as x-rays originating from Cu being present in the column, make the quantification of these types of elements more complicated. The coincidence method gives the ability to subtract other x-ray

lines by selecting a particular EEL energy window and creating the x-ray spectrum using x-rays inside and outside the time coincidence window which removes the unwanted x-ray signal arising form other processes. In Fig. 5.11(a), the conventional EEL spectrum from a GaAs semiconductor is shown where the different edges are indicated. In Fig. 5.11(b), the background subtracted EDX spectra are shown where the electron energies are indicated on (a). The red spectrum only uses electrons arising from the Ga L_{23} edge which makes that only the x-rays originating from Ga are visible. When taking electrons with energies inside the blue region, both x-ray lines are seen. This is because the EEL edges have large tails which makes that in this energy-loss region electrons arising from both the interaction with Ga and As are located. A method to disentangle the As L_α from the Ga L_α spectrum is to normalize both spectra from Fig. 5.11 in the region where only the Ga L_α x-rays are present. Then the coincidence x-ray spectrum, with both electrons coming from Ga and As, is subtracted with the coincidence x-ray spectrum where only the Ga electrons are present resulting in an x-ray spectrum containing only x-rays from the As L_α line. This type of methodology can always be used to disentangle x-ray spectra when there is a region in the x-ray spectrum where no overlap between the two x-rays is present. Note that in the entire background subtraction procedure, no prior knowledge on the shape of the background is used and that only the coincidence detection scheme gives information on the background.

5.4.6. Low concentration detection

Theoretical study

In this section it is investigated when the coincidence method can have advantages compared to conventional EELS and EDX. This is done by comparing the SNR between coincidence and conventional EELS/EDX from which is calculated using Eq. 2.19 and Eq. 2.23. The two main parameters which define the SNR are the incoming current I and signal-to-background ratio (SBR) which for EELS is defined as $C\sigma/B_e$. Similarly for EDX, the SBR is defined as $C\sigma_T\omega/B_x$. The other parameters chosen for the calculations are shown in Table 5.2 where the value for Cσ

is approximated using Eq. 5.5 on experimental data from which ϵ_e and B_e are the values obtained from *Section 5.4.2*, I is measured from the read out of fluorescence screen and time t is acquisition time. All these values are plugged into Eq. 5.11 and Eq. 2.19 while varying I and SBR. In Fig. 5.12 (a,b) both SNR_C and SNR_{EELS} are shown where the acquisition time has been kept constant for every calculation. An increase in SNR is seen when the incoming current and SBR increases, as could be expected. To verify under which circumstances coincidence detection outperforms conventional EELS, the ratio SNR_C/SNR_{EELS} is shown in Fig. 5.12(c). This shows that there is a well defined parameter space for which coincidence detection outperforms conventional EELS, more specifically in the low current and low SBR regime. From Fig. 5.12 (c) one can conclude that also with conventional EELS we can detect low concentration species in a surrounding matrix (low SBR situation) by choosing the current high enough. In practice, beam damage and limitations on total exposure time due to drift will limit the maximum dose.

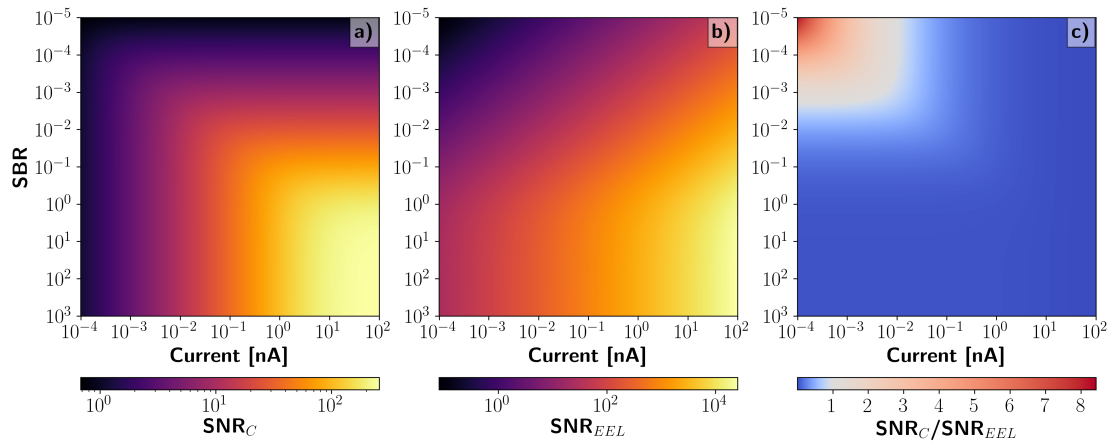

Figure 5.12.: **(a,b)** The SNR of the coincidence and conventional EELS while varying the SBR and I and keeping the exposure time constant. Note that both axes are logarithmic. The other parameters used to determine the SNR are indicated in Table 5.2. **(c)** The ratio between the SNR of coincidence and conventional EELS where a value larger than one indicates the region where coincidence outperforms conventional EELS (red colored areas).

$C\sigma$	$C\sigma_T$	ϵ_e	ϵ_x	τ [ns]	ω_{Si}	B_x
3.75e-5	3$C\sigma$	0.2	0.05	400	0.042	0.05$C\sigma$

Table 5.2.: The values for the parameters used in the calculation of comparison of SNR_C and SNR_{EELS}.

The same analysis can be applied for EDX where the main difference for the SNR is the fluorescence yield ω and collection efficiency ϵ_x (see Eq. 2.23). The result is shown in Fig. 5.13 where the values of Table 5.3 are used to obtain the results. For the comparison between EDX and the coincidence method, it is observed that at higher SBR values, the coincidence method outperforms conventional EDX, making the coincidence method very attractive when there is a lot of background signal in EDX. The reason for the worse performance of EDX, compared to EELS, is because the detected count rate is significantly lower due to the fluorescence yield and collection efficiency. In this study we varied the SBR without relating the background to any physical process where for EDX the SBR is in general higher than for EELS making it commonly accepted that EDX is preferable when it comes to trace element detection [206].

$C\sigma$	$C\sigma_T$	ϵ_e	ϵ_x	τ [ns]	ω_{Si}	B_e
3.75e-5	3$C\sigma$	0.2	0.05	400	0.042	$C\sigma$

Table 5.3.: The values for the parameters used in the calculation of comparison of SNR_C and SNR_{EDX}.

Experimental verification

To demonstrate the above prediction, a coincidence mapping on a 100 nm layer of diamond, grown on top of a germanium substrate, was performed using a $300 \times 1024 \times 1024$ scans with a dwell time of 10 μs. The sample drift per frame was calculated using the individual EELS frames since they have sufficient signal per frame to align them. The drift-corrected and summed EELS

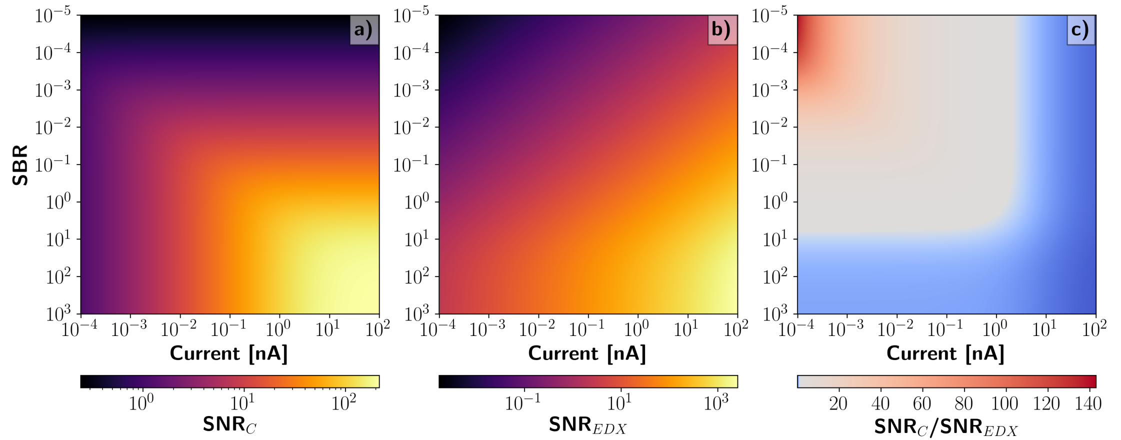

Figure 5.13.: **(a,b)** The SNR of the coincidence and conventional EDX while varying the *SBR* and *I* and keeping the exposure time constant. Note that both axes are logarithmic. The other parameters used to determine the SNR are indicated in Table 5.2. **(c)** The ratio between the SNR of coincidence and conventional EDX where a value larger than one indicates the region where coincidence outperforms conventional EDX (red colored areas).

signal is shown in Fig. 5.14 where the distortions on the left are flyback distortions since there was no flyback time in the experimental setup. For this sample, the main inquiry was to measure if there was any Ge incorporated in the diamond layer. The first step is to create an average EEL and EDX spectrum in a region of the diamond layer where the region of interest is shown in Fig. 5.14. The conventional EDX and EEL spectra are shown in Fig. 5.15(a,b). The conventional EDX spectrum shows a x-ray peak at the energy of Ge where the overlap of another x-ray peak, originating from the Cu L_α x-ray line, of the experimental sample grid [20]. Furthermore, due to the FIB sample preparation method Ga is likely incorporated into the sample which has a similar core-loss energy making it hard to distinguish between the Ge and Ga for EDX. The conventional EEL spectrum does not show any features around the Ge L_{23}-edge, or Ga L_{23}-edge. However when fitting a power-law to the background region indicated in Fig. 5.15(f), a small

gradual increase is seen starting from the Ga L_{23}-edge which does not correspond to a sharp core-loss edge. The gradual increase of the background-subtracted signal gives no clear indication on the presence of Ga or Ge. The residual spectrum seen from the background fit comes form the incapacity of the power-law to reproduce the background signal when the abundance of the element is very low. Next, the two-dimensional histogram using time difference and x-ray energy is shown in Fig. 5.15(c) where the post selection electron energy-loss window is shown in Fig. 5.15(b) (red window). An increase in signal is observed inside the time coincidence interval at a particular x-ray energy. From the two-dimensional histogram, the coincidence and background signal is calculated as discussed in *Section 5.4.1.* From this two background-free EDX spectra are calculated where the colors correspond to the EELS energy windows shown in Fig. 5.15(e) (blue and red). The blue window only corresponds to electrons undergoing the core-loss events with Ga. The red window has both Ga and Ge electrons in the coincidence signal hence both x-ray lines are excited which is similar to Fig. 5.11. This is seen in Fig. 5.15(d) where for the red spectrum, a small increase in signal is seen at higher energies indicating the presence of x-rays having a larger energy (see black ellipse) than the one arising from the Ga L_{α} line. The same method can be applied for EELS where in Fig. 5.15(d) the 2D histogram between time difference and EEL energy is shown. An increase in signal at higher electron energy loss is seen inside the time coincidence window indicating the presence of an element having a core-loss edge at these energy ranges. The background-subtracted coincidence EEL signal is shown in Fig. 5.15(f) where an onset is seen at an energy around 1100 eV which is before the Ge L_{23}-edge but could correspond to the Ga L_{23}-edge (1115eV). However, slower onset on the edge signal and the occurrence of higher x-ray energies when increasing the electron energy-loss indicates the presence of an element having a larger edge and x-ray energy hence the origin could be due to Ge. Note that the coincidence EEL spectrum is binned in order to improve the SNR of the spectrum.

This experimental data shows the advantage of the coincidence setup where in conventional EELS no presence of any core-loss edge is seen. When looking at the x-ray spectrum, a peak where Ge is expected is seen, and the Cu x-ray line also makes the background subtraction

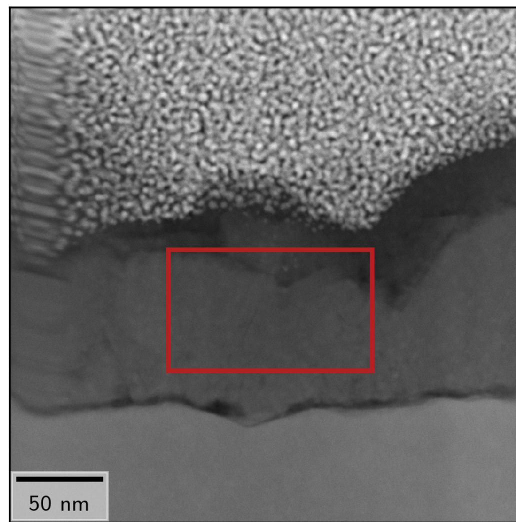

Figure 5.14.: A $300 \times 1024 \times 1024$ STEM scan at 10 μs on a diamond layer grown on top of a germanium substrate. The image shows the total number of electrons on the EELS detector at every probe position. The red window indicates the area from which the spectra are shown.

harder. Due to the limited energy resolution of EDX no clear distinction between Ge and Ga can be made, inviting interpretation errors when Ga would not be considered. The use of EELS which has a energy resolution in the order of eV adds extra information to disentangle between the two elements and gives some evidence on the presence of Ge in this specific diamond. However to clearly confirm the presence of Ge more experiments should be performed but this is outside the scope of this work where the aim is to show the potential of coincidence spectroscopy to reveal EELS edges which would remain hidden in conventional EELS.

5.4.7. Limit on the time resolution

Eq. 5.10 indicates that the SNR can be decreased via multiple routes. Firstly as shown in *Section 5.4.3* by increasing the incoming current, the SNR is improved. However it is not always

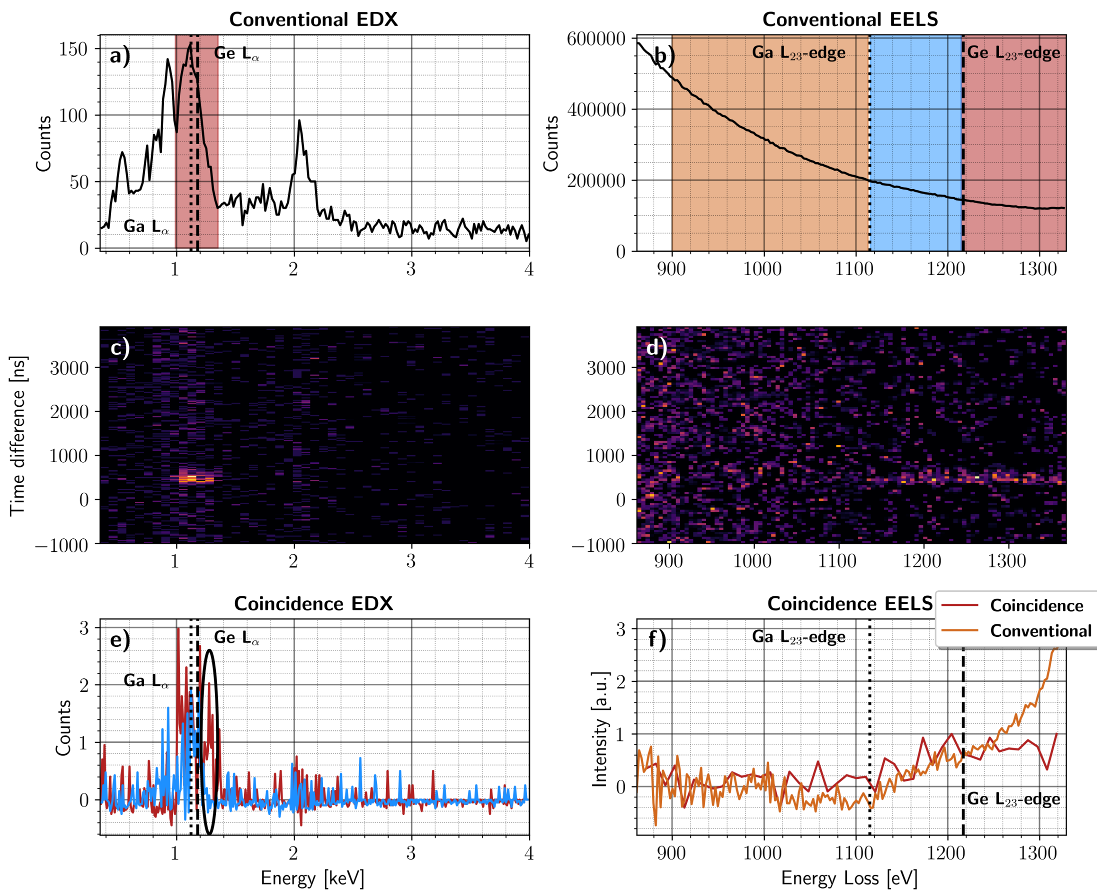

Figure 5.15.: **(a,b)** The conventional EDX and EELS signals of red region in Fig. 5.14. **(c)** Two dimensional histogram, using a post selection on electron energy losses which are shown in (b), between time difference and x-ray energy where the electron energies chosen are the ones within the red window. **(e)** The background subtracted x-ray spectrum for the two electron energy windows indicated in (a). The black ellipse indicates the region where an excess of counts are seen compared to the blue spectrum. **(d)** Similar to (c) except that one axis is now electron energy loss and the post selection is performed on the x-ray energies shown in (a). **(f)** The background-subtracted EEL spectrum where an increase of signal is observed starting from the Ga L_{23} edge indicating the presence of core-loss events. The signal is binned in order to improve the SNR of the spectrum. Additionally, the conventional background subtracted EEL spectrum is shown where the region for the power-law fit is indicated in brown (b).

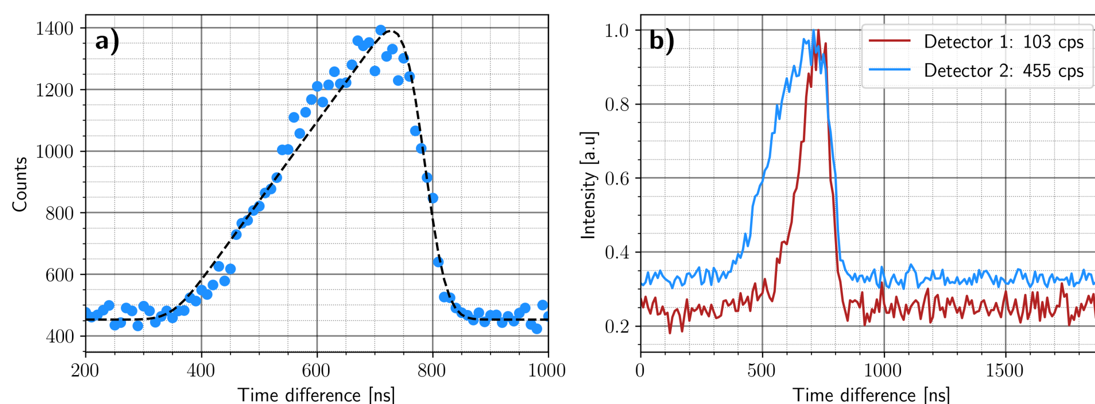

Figure 5.16.: **(a)** Zoom in on the shape of the time coincidence histogram where an asymmetric profile is seen. The dotted black line shows a Gaussian blurred saw-tooth function which would be the theoretical shape of the histogram. **(b)** The time coincidence histogram of two detectors. The sample holder is titled such that the count rate of x-rays on detector 1 is lower which is due to the shadowing of the detector. The width of the time coincidence peak is significantly lower for the shadowed detector (detector 1).

possible to increase the current due to limits of the electron gun or the specimen being radiation sensitive. Another method would be to acquire longer however this is sometimes not possible due to drift which leaves us with two other options: increasing the collection efficiency or improving the time resolution of the setup. From Fig. 5.8 (a) it is seen that the time coincidence interval has a width of approximately 400 ns which is disappointingly low in comparison to the <10 ns sampling capabilities of both EDX and EELS detector electronics. In order to improve the time resolution, the contributions from the different parts of the setup should be investigated. It is known that the relative large size of the SDD detectors influences the TOA of the x-rays. This is of no surprise since the SDD was developed as a 2D position-sensitive detector for ionizing particles where the point of impact was derived using the travel time of the signal [43, 220]. If the limiting factor on the time resolution would be the area of the detectors then this

would be visible in the shape of the time coincidence interval. The x-ray detectors used in the experiment have a circular shape, which should correspond to a sawtooth shape for the time resolution since the travel time depends linearly on the distance between x-ray impact and center but the detection area scales as r^2 meaning that on average more events will hit the outer region of the detector resulting in more weight for the longer time delays. In Fig. 5.16 (a), the time coincidence histogram is shown from which an asymmetric shape is indeed visible (blue). The black dotted line is a saw-tooth function which convolved with an extra instrumental Gaussian function having a standard deviation of 30 ns. This model shows that the shape and size of the SDD plays a dominant role in limiting the time resolution to a value much lower than what we could handle with the electronics. The extra convolution with 30 ns could be related to the finite electronic bandwidth of the preamplifier stages which would then be estimated to be in the 10 MHz range. Another time resolution limiting factor could be in the electron detector where the fast electrons interact inelastically at a stochastic depth which in combination with the finite drift velocity leads to a timing uncertainty of the electron arrival event. For a sensor thickness of 300 μm and a drift velocity in the order of 10^6 cm/s [221] this would result in a broadening of approx 30 ns [178, 222].

In order to verify our assumptions on the dominant role of the drift velocity in the SDD we tilt the sample holder in such a way that one detector receives a smaller count rate than the other one. This happens since the holder shadows a part of the detector hence a smaller area is illuminated. In Fig. 5.16 (b), both time coincidence histograms are shown from which the x-ray count rate on the detector is indicated. The width of the coincidence window for the non-shadowed detector (blue) is around twice as high as compared to the shadowed one (red) confirming that the illuminated area plays the most important role on the time resolution for the current coincidence setup.

One way to overcome this limitation could be to design new types of x-ray detectors which are similar to the pixelated electron detector with more channels, each having an integrated preamplifier stage, with a smaller active area to improve the time resolution while maintaining

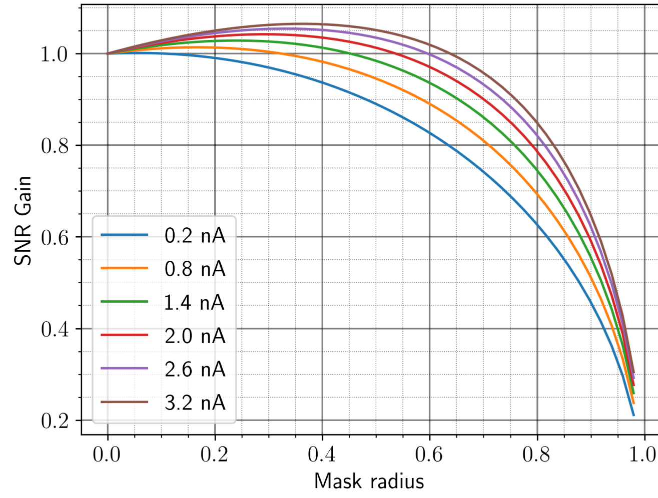

Figure 5.17.: The SNR gain as function of mask radius for different incoming currents. The SNR gain is defined as the ratio of the SNR with the SNR when the mask radius is zero.

a high solid angle. Highly integrated electronics could potentially make this a viable solution in the near future [223]. An alternative method could be to shadow some part of the detector where a smart choice on the masked area could improve the SNR. Since the detector is circular with radius R, we can choose a circular mask which is centred on the detector with a radius r between 0 and R. The efficiency (ϵ'_x) and time resolution (τ') of the new masked detector is:

$$\epsilon'_x(r) = \frac{R^2 - r^2}{R^2}\epsilon_x \tag{5.16}$$

$$\tau'(r) = \frac{R - r}{R}\tau + \Delta\tau \tag{5.17}$$

where $\Delta\tau$ is the broadening which arises from other time broadening influences in the experimental setup. By inserting the two values into Eq. 5.10 the influence on the radius of the mask on the SNR can be investigated. In order to do this, values on the other parameters should be known. Here the values are approximated from the data shown in Fig. 5.8. The parameter values

Table 5.4.: The values for the parameters used in the calculation of SNR when masking the detector.

Cσ	Cσ_T	ϵ_e	ϵ_x	τ [ns]	$\Delta\tau$ [ns]	ω_{Si}	B_e	B_x
3.75e-5	3Cσ	0.2	0.05	400	30	0.042	Cσ	0.05 Cσ_T

used for the SNR simulation in Fig. 5.17 are shown in Table 5.4. Note that some parameters values are given relatively to Cσ, for instance B$_e$ =Cσ which indicates that the number of background electrons is equal to the number of electrons in the core-loss edge. In Fig. 5.17, the SNR gain, defined as the ratio of the SNR with the SNR when the mask radius is zero, as a function of mask radius for different incoming electron currents is shown. The gain in SNR is maximal when the current is higher and has an increase of 7%. Further with higher current, the optimal mask radius increases to 0.37 for the highest current used. From these calculations it is seen that the detector masking using an annular detector can increase the SNR at the expense of detection efficiency. However, the gain provided by this trick is minor and depends on the incoming current hence making this option not very attractive.

It should be noted that improving the time resolution by a factor 10-100 should be technically feasible which would result in an equal reduction in required dose for the same SNR and hence is the single most important parameter to improve when trace element analysis is required through coincidence measurement.

5.5. Conclusions and Outlook

In this chapter, a novel setup is demonstrated which is able to record the time of arrival of individual x-rays and inelastically scattered electrons with nanosecond precision.

The advantage of this method is that it reveals correlation data while preserving the full EELS and EDX signal without compromise in speed or acquisition time. We demonstrate that the correlation information provides several important advantages on top of simply merging two

independent spectral channels. Model-free background subtraction takes away the requirement of having to fit a model background in a fitting region and is especially interesting in cases where overlapping edges occur. We show that coincidence detection provides a benefit for low-concentration elements in the presence of a high background as would occur in cases relating to doping and trace elements; typically topics which are hard or even impossible to treat with EELS despite its very favourable detection efficiency.

We identified the single most important parameter to further improve detection limits in coincidence detection between core loss EELS and EDX to be the limited time resolution due to large area SDD detectors that are commonly used in modern TEM setups. The most optimal way to make progress here would be to redesign the EDX detectors with the requirement of both high collection efficiency and good time resolution. We estimate that another factor 10-100 could be achievable which would have a similar effect as improving the electron dose by that same factor without the downside of beam damage or drift.

The novel method of detecting single events instead of the integrated signal, opens up possibilities for other types of scattering phenomena where signals are correlated with each other in time such as EELS-CL, secondary electrons-EELS and many more. The intrinsic data compression by storing only actual events, the lack of readout time and the fact that synchronisation between multiple detectors is reduced to the problem of syncing them all to a single master clock holds many benefits for implementation in TEM setups with their ever increasing amount of detectors and datarates.

6. General Conclusions and Outlook

This thesis work was devoted to developing three novel transmission electron microscopy techniques. The first chapter contains an introduction to electron scattering and detection which provides a basis to understand how electrons interact and how they are measured. The second chapter described commonly used electron microscopy techniques and introduces the motivation for the development of the three novel techniques. In all three setups, hybrid pixelated detectors are used showing how the development of these types of electron detectors has really opened up the path to new experiments.

In chapter three, the 4D STEM in SEM method is discussed where by implementing a hybrid pixelated detector inside an SEM, transmitted electrons could be detected making it effectively a STEM instrument. Furthermore, by synchronizing the electron beam with the detector, 4D STEM experiments could be performed on large fields of view while keeping the mode of operation relatively straight forward. This was shown on multiple 2D materials from which structural information, such as grain boundaries, strain, stacking sequence, *etc.* could be retrieved.

In the future, this technique can be developed into a more automatic procedure where orientation and phase mapping can be performed at higher speeds and even larger fields of view on a multitude of materials. The higher speeds can be retrieved by using other more advanced hybrid pixelated detectors which have speeds of 1000 fps which is 40 times faster than the current implementation. The larger field of view can be achieved by using a controllable stage which changes the position of the specimen with respect to the electron probe. One can even take this one step further and perform serial electron diffraction experiments. This is similar to serial x-ray diffraction which is used to retrieve unknown crystal structures. The same idea can

be implemented into the SEM where automatic acquisition of millions of diffraction patterns can help unravel the crystal structure of some materials. However to do this, one should have an automated setup after which the challenge of data treatment arises since the amount of data is very large ~TB. Also, contrary to x-ray diffraction, dynamical scattering occurs for electron adding complexity to the data analysis.

In chapter four, an event driven detector was used to perform high resolution 4D STEM experiments at high acquisition speeds and at low doses. In this work, multi-frame scanning was performed and it was shown that the measurement of the entire diffraction pattern improves the SNR compared to the conventional ADF and ABF method. Increasing the speed and multi-frame scanning is especially important for materials which are very susceptible to beam damage since the fast scanning reduces both dose and other artefacts such as drift.

This type of data acquisition can become the de-facto method in TEM if the maximum current on the detector can be increased by an order of magnitude (~50 pA). This would come with an increase in generated data and new fast methods of data processing need to be developed.

Chapter five describes how measuring the TOA between x-rays and inelastically scattered electrons at nanosecond resolution can offer advantages compared to conventional EELS and EDX. For instance, background-free EELS and EDX can be performed without needing a model of this background. Moreover, for trace elements this method can improve the SNR compared to EELS and EDX. Additionally, the method of data acquisition, where every individual event is stored, makes that the individual EELS and EDX signals are retained, so measuring the individual events adds information but does not remove anything from the conventional signals.

Further investigation on improving the time resolution of the setup can be performed since this increases the sensitivity of the method. Also, a better synchronization method where instead of sending trigger signals every 200 μs can be developed via the use of a master clock. On the software side, better and faster algorithms can be developed to retrieve the time correlation information in real time.

In the three discussed methods, multiple different hardware, such as scan engine, electron detector and pulse processors, where used to develop the experimental setups. To make these

devices communicate with each other, an API is essential. In this work, all these devices had an API in python making it relatively easy to script them and performing more automated acquisitions. Next to the API being available, proper documentation of the hardware and its API is also important which was fortunately the case for these devices. Next to the open hardware, the availability of the open-source software made it possible to build new analysis algorithms on top of existing libraries. In order to stimulate this community, I made all data relevant to the publications available on Zenodo with their data processing coda as well as contribution to Pixstem and Pyxem open source projects. I am convinced that this open attitude can push scientific development forward and the examples here show that this model is not a threat to commercial vendors but rather welcomes multiple small and median enterprise (SME) players that create new flourishing businesses based on innovation.

A. List of Abbreviations

2D	Two Dimensional
4D STEM	Four Dimensional Scanning Transmission Electron Microscopy
ABF	Annular Bright Field
API	Application Programming Interface
ASIC	Application-Specific Integrated Circuit
BLG	Bilayer Graphene
CCD	Charge Coupled Device
CMOS	Complementary Metal Oxide Semiconductor
CVD	Chemical Vapor Deposition
DLD	Delay Line Detector
DQE	Detector Quantum Efficiency
EDX	Energy Dispersive X-ray Spectroscopy
EELS	Electron Energy Loss Spectroscopy
FEG	Field Emission Gun
FET	Field Effect Transistor
FPS	Frames per Second
FOV	Field of View
GO	Graphene Oxide
GOS	Generalized Oscillator Strength
HAADF	High-Angle Annular Dark-Field
HRSTEM	High Resolution Scanning Transmission Electron Microscopy

LM	Layered Materials
MAPS	Monolithic Active Pixel Sensor
ML	Multilayer
MOCVD	Metal Organic Chemical Vapor Deposition
NBED	Nano Beam Electron Diffraction
PACBED	Position Averaged Convergent Beam Electron Diffraction
PMMA	Polymethyl Methacrylate
POA	Phase Object Approximation
PMT	Photomultiplier Tube
PSF	Point Spread Function
P-SHG	Polarization-resolved Second Harmonics Generation
RUP	Random Uncorrelated Process
SDD	Silicon Drift Detector
SEM	Scanning Electron Microscope
SHG	Second Harmonics Generation
SLG	Single Layer Graphene
STEM	Scanning Transmission Electron Microscopy
TEM	Transmission Electron Microscope
TDC	Time to Digital Converter
TMD	Transition Metal Dichalcogenides
VDF	Virtual Dark Field
WPOA	Weak Phase Object Approximation

B. Output

B.1. Publications

1. D. Jannis, K. Müller-Caspary, A. Béché, A. Oelsner, J. Verbeeck, *Spectroscopic coincidence experiments in transmission electron microscopy*. Appl. Phys. Lett. 114, 143101 (2019); DOI: 10.1063/1.5092945

2. J. Wang Y. Shin, N. Gauquelin, Y. Yang, C. Lee, D. Jannis, J. Verbeeck, J. M. Rondinelli, S. J. May, *Physical properties of epitaxial $SrMnO_{2.5}$-δ F_{γ} oxyfluoride films*, Journal of Physics: Condensed Matter (2019); DOI: 10.1088/1361-648X/ab2414

3. V. Prabhakara, D. Jannis, A. Béché, H. Bender, J. Verbeeck, *Strain measurement in semiconductor FinFET devices using a novel moiré demodulation technique*, Semiconductor Science and Technology (2020); DOI: 10.1088/1361-6641/ab5da2

4. B. Chen, N. Gauquelin, P. Reith, U. Halisdemir, D. Jannis, M. Spreitzer, M. Huijben, St. Abel, J. Fompeyrine, J. Verbeeck, H. Hilgenkamp, G. Rijnders, and G. Koster, *Thermal-strain-engineered ferromagnetism of $LaMnO_3$/$SrTiO_3$ heterostructures grown on silicon*, Physical Review Materials (2020); DOI: 10.1103/PhysRevMaterials.4.024406

5. V. Prabhakara, D. Jannis, G. Guzzianti, A. Béché, H. Bender, J. Verbeeck, *HAADF-STEM block-scanning strategy for local measurement of strain at the nanoscale*, Ultramicroscopy (2020); DOI: 10.1016/j.ultramic.2020.113099

6. B. Chen, N. Gauquelin, D. Jannis, D. M Cunha, U. Halisdemir, C. Piamonteze, J. Hong Lee, J. Belhadi, F. Eltes, S. Abel, Z. Jovanović, M. Spreitzer, J. Fompeyrine, J. Verbeeck, M. Bibes, M. Huijben, G. Rijnders, G. Koster, *Strain-Engineered Metal-to-Insulator Transition and Orbital Polarization in Nickelate Superlattices Integrated on Silicon*, Advanced Materials (2020); DOI: 10.1002/adma.202004995

7. B. Chen, N. Gauquelin, R. J. Green, J. Hong Lee, C. Piamonteze, M. Spreitzer, D. Jannis, J. Verbeeck, M. Bibes, M. Huijben, G. Rijnders, G. Koster, *Spatially Controlled Octahedral Rotations and Metal–Insulator Transitions in Nickelate Superlattices*, Nano Letters (2021); DOI: doi.org/10.1021/acs.nanolett.0c03850

8. A. Orekhov, D. Jannis, N. Gauquelin, G. Guzzinati, A. Nalin Mehta, S. Psilodimitrakopoulos, L. Mouchliadis, P. K. Sahoo, I. Paradisanos, A.C. Ferrari, G. Kioseoglou, E. Stratakis, J. Verbeeck, *Wide field of view crystal orientation mapping of layered materials*, (2021) *(Under review in ACS Applied Materials & Interfaces)*
9. S. Psilodimitrakopoulos, A. Orekhov, L. Mouchliadis, D. Jannis, G.M. Maragkakis, G. Kourmoulakis, N. Gauquelin, G. Kioseoglou, J. Verbeeck, E. Stratakis, *Optical versus electron diffraction imaging of Twist-angle in 2D transition metal dichalcogenide bilayer superlattices*, 2D Materials (2021); DOI:10.1038/s41699-021-00258-5

10. T.C. van Thiel, W. Brezezicki, C. Autieri, J.R. Hortensius, D. Afanasiev, N. Gauquelin, D. Jannis, N. Janssen, D.J. Groenendijk, J. Fatermans, S. Van Aert, J. Verbeeck, M.

Cuoco and A.D. Caviglia, *Coupling Charge and Topological Reconstructions at Polar Oxide Interfaces*, Physical Review Letters (2021); DOI:10.1103/PhysRevLett.127.127202

11. A. Velazco, D. Jannis, A. Béché, J. Verbeeck, *Reducing electron beam damage through alternative STEM scanning strategies. Part I–Experimental findings*, (2021) *(Accepted in Ultramicroscopy)*

12. D. Jannis, A. Velazco, A. Béché, J. Verbeeck, *Reducing electron beam damage through alternative STEM scanning strategies. Part II–Attempt towards an empirical model describing the damage process*, (2021) *(Under review in Ultramicroscopy)*

13. D. Jannis, C. Hofer, C. Gao, X. Xie, T.J. Pennycook, J. Verbeeck, *Event driven 4D STEM acquisition with a Timepix3 detector: microsecond dwell time and faster scans for high precision and low dose applications*, (2021) *(Under review in Ultramicroscopy)*

14. D. Jannis, K. Müller-Caspary, A. Béché, J. Verbeeck, *Coincidence detection of EELS and EDX spectral events in the electron microscope*, Applied sciences (2021); DOI:10.1038/s41699-021-00258-5

15. N. Lebedev, Y. Huang, A. Rana, D. Jannis, N. Gauquelin, J. Verbeeck, J. Aarts *On the resistance minimum in* $LaAlO_3/Eu_{1-x}La_xTiO_3/SrTiO_3$ heterostructures, (2021) *(preprint on Arxiv)*

B.2. Conferences

1. D. Jannis, K. Müller-Caspary, A. Béché, A. Oelsner and J. Verbeeck, Spectroscopic coincidence experiments in transmission electron microscopy between EELS and EDX,

DPG Spring Meeting, 31/03/19-05/04/19, Regensburg, Germany *(oral presentation)*

2. D. Jannis, K. Müller-Caspary, A. Béché, A. Oelsner and J. Verbeeck, Spectroscopic coincidence experiments in transmission electron microscopy, PICO Meeting, 6-10 May 2019, Kasteel Vaalsbroek, The Netherlands *(poster presentation)*

3. D. Jannis, K. Müller-Caspary, A. Béché and J. Verbeeck, Single Event Detection in Transmission Electron Microscopy for Spectroscopic Coincidence Experiments, eBEAM Meeting, 6 April 2021 *(oral presentation)*

4. D. Jannis, K. Müller-Caspary, A. Béché and J. Verbeeck, Single Event Detection in Transmission Electron Microscopy for Spectroscopic Coincidence Experiments, Virtual PICO Meeting, 2-6 May 2021 *(poster presentation)*

5. D. Jannis, K. Müller-Caspary, A. Béché and J. Verbeeck, Time Correlation Spectroscopy using Event-Driven Data Acquisition, MMC Virtual Congress, 6-9 July 2021 *(oral presentation)*

6. D. Jannis, K. Müller-Caspary, A. Béché and J. Verbeeck, Single Event Detection in TEM for Spectroscopic Coincidence Measurements, Metanano Virtual Conference on Metamaterials and Nanophotonics, 13-17 September 2021 *(oral presentation)*

Bibliography

[1] Y. Aharonov and D. Bohm. "Significance of Electromagnetic Potentials in the Quantum Theory". In: *Physical Review* 115.3 (Aug. 1, 1959), pp. 485–491 (cit. on p. 10).

[2] M. De Graef. *Introduction to Conventional Transmission Electron Microscopy.* Cambridge University Press, 2003 (cit. on p. 12).

[3] D. L. Misell. "A method for the solution of the phase problem in electron microscopy". In: *Journal of Physics D: Applied Physics* 6.1 (Jan. 1, 1973), pp. L6–L9 (cit. on p. 12).

[4] E. J. Kirkland. *Advanced Computing in Electron Microscopy.* Boston, MA: Springer US, 2010 (cit. on p. 12).

[5] G. Taylor. "The phase problem". In: *Acta Crystallographica Section D* 59.11 (Nov. 2003), pp. 1881–1890 (cit. on p. 12).

[6] D. Gabor. "A New Microscopic Principle". In: *Nature* 161.4098 (May 15, 1948), pp. 777–778 (cit. on p. 12).

[7] W. Coene et al. "Phase retrieval through focus variation for ultra-resolution in field-emission transmission electron microscopy". In: *Physical Review Letters* 69.26 (Dec. 28, 1992), pp. 3743–3746 (cit. on p. 12).

[8] P. Schiske. "Image reconstruction by means of focus series [1]: Image Reconstruction By Focus Series". In: *Journal of Microscopy* 207.2 (Aug. 2002), pp. 154–154 (cit. on p. 12).

[9] J. M. Cowley and A. F. Moodie. "The scattering of electrons by atoms and crystals. I. A new theoretical approach". In: *Acta Crystallographica* 10.10 (Oct. 1, 1957), pp. 609–619 (cit. on p. 13).

[10] J. H. Chen and D. Van Dyck. "Accurate multislice theory for elastic electron scattering in transmission electron microscopy". In: *Ultramicroscopy* 70.1 (Dec. 1997), pp. 29–44 (cit. on p. 13).

[11] O. L. Krivanek et al. "Vibrational spectroscopy in the electron microscope". In: *Nature* 514.7521 (Oct. 2014), pp. 209–212 (cit. on pp. 13, 44).

[12] T. Miyata et al. "Measurement of vibrational spectrum of liquid using monochromated scanning transmission electron microscopy–electron energy loss spectroscopy". In: *Microscopy* 63.5 (Oct. 2014), pp. 377–382 (cit. on p. 13).

[13] D. Pines and D. Bohm. "A Collective Description of Electron Interactions: II. Collective vs Individual Particle Aspects of the Interactions". In: *Physical Review* 85.2 (Jan. 15, 1952), pp. 338–353 (cit. on p. 13).

[14] L. Garvie et al. "Interband transitions of crystalline and amorphous SiO2: An electron energy-loss spectroscopy (EELS) study of the low-loss region". In: *Solid State Communications* 106.5 (1998), pp. 303–307 (cit. on p. 13).

[15] M. Inokuti. "Inelastic Collisions of Fast Charged Particles with Atoms and Molecules—The Bethe Theory Revisited". In: *Rev. Mod. Phys.* 43 (3 July 1971), pp. 297–347 (cit. on p. 15).

[16] R. D. Leapman, P. Rez, and D. F. Mayers. "K , L , and M shell generalized oscillator strengths and ionization cross sections for fast electron collisions". In: *The Journal of Chemical Physics* 72.2 (Jan. 15, 1980), pp. 1232–1243 (cit. on pp. 15–16).

[17] L. Reimer and H. Kohl. *Transmission electron microscopy: physics of image formation.* 5th ed. Springer series in optical sciences 36. New York, NY: Springer, 2008 (cit. on pp. 16, 20, 116).

[18] R. Egerton. "K-shell ionization cross-sections for use in microanalysis". In: *Ultramicroscopy* 4.2 (Jan. 1979), pp. 169–179 (cit. on p. 16).

[19] A. J. Garratt-Reed and D. C. Bell. *Energy-dispersive X-ray analysis in the electron microscope*. Microscopy handbooks 49. OCLC: ocm49639439. Oxford: BIOS, 2003. 141 pp. (cit. on pp. 17, 52).

[20] D. B. Williams and C. B. Carter. *Transmission electron microscopy: a textbook for materials science*. 2. ed. New York: Springer, 2009. 760 pp. (cit. on pp. 20, 53, 55, 74, 134, 140, 144).

[21] A. Faruqi et al. "Evaluation of a hybrid pixel detector for electron microscopy". In: *Ultramicroscopy* 94.3 (Apr. 2003), pp. 263–276 (cit. on pp. 20, 24).

[22] Strüder, L. et al. "The European Photon Imaging Camera on XMM-Newton: The pn-CCD camera *". In: *A&A* 365.1 (2001), pp. L18–L26 (cit. on p. 21).

[23] H. Ryll et al. "A pnCCD-based, fast direct single electron imaging camera for TEM and STEM". In: 11.04 (Apr. 2016), P04006–P04006 (cit. on p. 21).

[24] H. Keller, G. Klingelhöfer, and E. Kankeleit. "A position sensitive microchannelplate detector using a delay line readout anode". In: *Nuclear Instruments and Methods in Physics Research Section A: Accelerators, Spectrometers, Detectors and Associated Equipment* 258.2 (Aug. 1987), pp. 221–224 (cit. on p. 21).

[25] A. Oelsner et al. "Microspectroscopy and imaging using a delay line detector in time-of-flight photoemission microscopy". In: *Review of Scientific Instruments* 72.10 (Oct. 2001), pp. 3968–3974 (cit. on p. 22).

[26] D. Blavette et al. "An atom probe for three-dimensional tomography". In: *Nature* 363.6428 (June 1993), pp. 432–435 (cit. on p. 22).

[27] Z. Vager, R. Naaman, and E. P. Kanter. "Coulomb Explosion Imaging of Small Molecules". In: *Science* 244.4903 (Apr. 28, 1989), pp. 426–431 (cit. on p. 22).

[28] I. Ali et al. “Multi-hit detector system for complete momentum balance in spectroscopy in molecular fragmentation processes”. In: *Nuclear Instruments and Methods in Physics Research Section B: Beam Interactions with Materials and Atoms* 149.4 (Mar. 1999), pp. 490–500 (cit. on p. 22).

[29] K. Müller-Caspary, A. Oelsner, and P. Potapov. “Two-dimensional strain mapping in semiconductors by nano-beam electron diffraction employing a delay-line detector”. In: *Applied Physics Letters* 107.7 (Aug. 17, 2015), p. 072110 (cit. on p. 22).

[30] R. Turchetta et al. “A monolithic active pixel sensor for charged particle tracking and imaging using standard VLSI CMOS technology”. In: *Nuclear Instruments and Methods in Physics Research Section A: Accelerators, Spectrometers, Detectors and Associated Equipment* 458.3 (Feb. 2001), pp. 677–689 (cit. on p. 23).

[31] G. McMullan, R. Turchetta, and A. R. Faruqi. “Single event imaging for electron microscopy using MAPS detectors”. In: *Journal of Instrumentation* 6.04 (Apr. 2011), pp. C04001–C04001 (cit. on p. 23).

[32] G. McMullan et al. “Experimental observation of the improvement in MTF from backthinning a CMOS direct electron detector”. In: *Ultramicroscopy* 109.9 (Aug. 2009), pp. 1144–1147 (cit. on p. 23).

[33] G. McMullan et al. “Comparison of optimal performance at 300 keV of three direct electron detectors for use in low dose electron microscopy”. In: *Ultramicroscopy* 147 (Dec. 2014), pp. 156–163 (cit. on p. 23).

[34] W. Kuhlbrandt. “The Resolution Revolution”. In: *Science* 343.6178 (Mar. 28, 2014), pp. 1443–1444 (cit. on pp. 24, 94).

[35] B. E. Bammes et al. “Direct electron detection yields cryo-EM reconstructions at resolutions beyond 3/4 Nyquist frequency”. In: *Journal of Structural Biology* 177.3 (Mar. 2012), pp. 589–601 (cit. on pp. 24, 94).

[36] M. W. Tate et al. “High Dynamic Range Pixel Array Detector for Scanning Transmission Electron Microscopy”. In: *Microscopy and Microanalysis* 22.1 (Feb. 2016), pp. 237–249 (cit. on p. 24).

[37] X. Llopart et al. “Timepix, a 65k programmable pixel readout chip for arrival time, energy and/or photon counting measurements”. In: *Nuclear Instruments and Methods in Physics Research Section A: Accelerators, Spectrometers, Detectors and Associated Equipment* 581.1 (Oct. 2007), pp. 485–494 (cit. on p. 26).

[38] P. Lechner et al. “Silicon drift detectors for high resolution room temperature X-ray spectroscopy”. In: *Nuclear Instruments and Methods in Physics Research Section A: Accelerators, Spectrometers, Detectors and Associated Equipment* 377.2 (1996), pp. 346–351 (cit. on p. 27).

[39] L. Strüder et al. “Development of the Silicon Drift Detector for Electron Microscopy Applications”. In: *Microscopy Today* 28.5 (2020), pp. 46–53 (cit. on p. 27).

[40] V. Drndarevic, P. Ryge, and T. Gozani. “Digital signal processing for high rate gamma-ray spectroscopy”. In: *Nuclear Instruments and Methods in Physics Research Section A: Accelerators, Spectrometers, Detectors and Associated Equipment* 277.2 (1989), pp. 532–536 (cit. on p. 28).

[41] T. Lakatos. “Adaptive digital signal processing for X-ray spectrometry”. In: *Nuclear Instruments and Methods in Physics Research Section B: Beam Interactions with Materials and Atoms* 47.3 (1990), pp. 307–310 (cit. on p. 28).

[42] V. Jordanov and G. Knoll. “Digital pulse processor using moving average technique”. In: *IEEE Transactions on Nuclear Science* 40.4 (1993), pp. 764–769 (cit. on p. 28).

[43] G. F. Knoll. *Radiation detection and measurement.* 4th ed. OCLC: ocn612350364. Hoboken, N.J: John Wiley, 2010. 830 pp. (cit. on pp. 28, 148).

[44] J. C. Meyer et al. “Experimental analysis of charge redistribution due to chemical bonding by high-resolution transmission electron microscopy”. In: *Nature Materials* 10.3 (Mar. 2011), pp. 209–215 (cit. on p. 31).

[45] O. Krivanek, N. Dellby, and A. Lupini. “Towards sub-$\mathring{A}$ electron beams”. In: *Ultramicroscopy* 78.1 (1999), pp. 1–11 (cit. on p. 32).

[46] M. Haider et al. “Electron microscopy image enhanced”. In: *Nature* 392.6678 (Apr. 1, 1998), pp. 768–769 (cit. on p. 32).

[47] M. Haider et al. “A spherical-aberration-corrected 200 kV transmission electron microscope”. In: *Ultramicroscopy* 75.1 (1998), pp. 53–60 (cit. on p. 32).

[48] M. Nord et al. “Fast Pixelated Detectors in Scanning Transmission Electron Microscopy. Part I: Data Acquisition, Live Processing, and Storage”. In: *Microscopy and Microanalysis* 26.4 (Aug. 2020), pp. 653–666 (cit. on pp. 34, 62).

[49] D. N. Johnstone et al. *pyxem/pyxem: pyxem 0.13.3.* Version v0.13.3. July 2021 (cit. on pp. 34, 62).

[50] B. H. Savitzky et al. “py4DSTEM: A Software Package for Four-Dimensional Scanning Transmission Electron Microscopy Data Analysis”. In: *Microscopy and Microanalysis* 27.4 (2021), pp. 712–743 (cit. on pp. 34, 38).

[51] A. Clausen et al. *LiberTEM/LiberTEM: 0.7.1.* Version 0.7.1. July 2021 (cit. on p. 34).

[52] S. Somnath et al. *USID and Pycroscopy – Open frameworks for storing and analyzing spectroscopic and imaging data.* 2019. arXiv: `1903.09515 [physics.data-an]` (cit. on p. 34).

[53] M. Krajnak et al. “Pixelated detectors and improved efficiency for magnetic imaging in STEM differential phase contrast”. In: *Ultramicroscopy* 165 (2016), pp. 42–50 (cit. on p. 34).

[54] K. Müller-Caspary et al. "Electrical Polarization in AlN/GaN Nanodisks Measured by Momentum-Resolved 4D Scanning Transmission Electron Microscopy". In: *Phys. Rev. Lett.* 122 (10 Mar. 2019), p. 106102 (cit. on p. 34).

[55] A. Beyer et al. "Quantitative Characterization of Nanometer-Scale Electric Fields via Momentum-Resolved STEM". In: *Nano Letters* 21.5 (Mar. 10, 2021), pp. 2018–2025 (cit. on p. 34).

[56] K. Müller et al. "Atomic electric fields revealed by a quantum mechanical approach to electron picodiffraction". In: *Nature Communications* 5.1 (Dec. 2014), p. 5653 (cit. on p. 34).

[57] S. Fang et al. "Atomic electrostatic maps of 1D channels in 2D semiconductors using 4D scanning transmission electron microscopy". In: *Nature Communications* 10.1 (Dec. 2019), p. 1127 (cit. on p. 34).

[58] A. Béché et al. "Improved precision in strain measurement using nanobeam electron diffraction". In: *Applied Physics Letters* 95.12 (Sept. 21, 2009), p. 123114 (cit. on pp. 34–35).

[59] C. Gammer et al. "Local nanoscale strain mapping of a metallic glass during *in situ* testing". In: *Applied Physics Letters* 112.17 (Apr. 23, 2018), p. 171905 (cit. on p. 34).

[60] S. N. Bogle et al. "Size analysis of nanoscale order in amorphous materials by variable-resolution fluctuation electron microscopy". In: *Ultramicroscopy* 110.10 (2010), pp. 1273–1278 (cit. on p. 34).

[61] C. Mahr et al. "Theoretical study of precision and accuracy of strain analysis by nano-beam electron diffraction". In: *Ultramicroscopy* 158 (Nov. 2015), pp. 38–48 (cit. on pp. 35, 66).

[62] T. C. Pekin et al. "Optimizing disk registration algorithms for nanobeam electron diffraction strain mapping". In: *Ultramicroscopy* 176 (May 2017), pp. 170–176 (cit. on pp. 35, 66).

[63] R. Yuan, J. Zhang, and J.-M. Zuo. "Lattice strain mapping using circular Hough transform for electron diffraction disk detection". In: *Ultramicroscopy* 207 (Dec. 2019), p. 112837 (cit. on pp. 35, 66).

[64] T. Grieb et al. "4D-STEM at interfaces to GaN: Centre-of-mass approach & NBED-disc detection". In: *Ultramicroscopy* 228 (Sept. 2021), p. 113321 (cit. on pp. 35, 66).

[65] E. F. Rauch et al. "Automated nanocrystal orientation and phase mapping in the transmission electron microscope on the basis of precession electron diffraction". In: *Zeitschrift für Kristallographie* 225.2 (Mar. 2010), pp. 103–109 (cit. on p. 36).

[66] E. Rauch and M. Véron. "Automated crystal orientation and phase mapping in TEM". In: *Materials Characterization* 98 (Dec. 2014), pp. 1–9 (cit. on p. 36).

[67] J. Jeong et al. "Automated crystal orientation mapping by precession electron diffraction assisted four-dimensional scanning transmission electron microscopy (4D-STEM) using a scintillator based CMOS detector". In: *arXiv:2102.09711 [cond-mat, physics:physics]* (Mar. 5, 2021). arXiv: `2102.09711` (cit. on p. 36).

[68] I. Lobato and D. Van Dyck. "MULTEM: A new multislice program to perform accurate and fast electron diffraction and imaging simulations using Graphics Processing Units with CUDA". In: *Ultramicroscopy* 156 (Sept. 2015), pp. 9–17 (cit. on pp. 36, 82).

[69] I. Lobato, S. Van Aert, and J. Verbeeck. "Progress and new advances in simulating electron microscopy datasets using MULTEM". In: *Ultramicroscopy* 168 (Sept. 2016), pp. 17–27 (cit. on pp. 36, 82).

[70] L. W. HOBBS. "Application of Transmission Electron Microscopy to Radiation Damage in Ceramics". In: *Journal of the American Ceramic Society* 62.5-6 (1979), pp. 267–278. eprint: `https://ceramics.onlinelibrary.wiley.com/doi/pdf/10.1111/j.1151-2916.1979.tb09480.x` (cit. on p. 38).

[71] R. M. Glaeser. "Limitations to significant information in biological electron microscopy as a result of radiation damage". In: *Journal of Ultrastructure Research* 36.3 (1971), pp. 466–482 (cit. on p. 38).

[72] I. Lazić, E. G. Bosch, and S. Lazar. "Phase contrast STEM for thin samples: Integrated differential phase contrast". In: *Ultramicroscopy* 160 (Jan. 2016), pp. 265–280 (cit. on pp. 38, 41, 108).

[73] E. G. Bosch and I. Lazić. "Analysis of depth-sectioning STEM for thick samples and 3D imaging". In: *Ultramicroscopy* 207 (2019), p. 112831 (cit. on p. 41).

[74] K. Müller-Caspary et al. "Comparison of first moment STEM with conventional differential phase contrast and the dependence on electron dose". In: *Ultramicroscopy* 203 (2019). 75th Birthday of Christian Colliex, 85th Birthday of Archie Howie, and 75th Birthday of Hannes Lichte / PICO 2019 - Fifth Conference on Frontiers of Aberration Corrected Electron Microscopy, pp. 95–104 (cit. on p. 41).

[75] J. Rodenburg, B. McCallum, and P. Nellist. "Experimental tests on double-resolution coherent imaging via STEM". In: *Ultramicroscopy* 48.3 (Mar. 1993), pp. 304–314 (cit. on pp. 41, 43).

[76] J. M. Rodenburg and R. Bates. "The theory of super-resolution electron microscopy via Wigner-distribution deconvolution". In: *Philosophical Transactions of the Royal Society of London. Series A: Physical and Engineering Sciences* 339.1655 (June 15, 1992), pp. 521–553 (cit. on p. 41).

[77] A. M. Maiden and J. M. Rodenburg. "An improved ptychographical phase retrieval algorithm for diffractive imaging". In: *Ultramicroscopy* 109.10 (Sept. 2009), pp. 1256–1262 (cit. on p. 41).

[78] M. Humphry et al. "Ptychographic electron microscopy using high-angle dark-field scattering for sub-nanometre resolution imaging". In: *Nature Communications* 3.1 (Jan. 2012), p. 730 (cit. on p. 41).

[79] A. Maiden, D. Johnson, and P. Li. “Further improvements to the ptychographical iterative engine”. In: *Optica* 4.7 (July 2017), pp. 736–745 (cit. on p. 41).

[80] R. F. Egerton. *Electron energy-loss spectroscopy in the electron microscope.* Third edition. The language of science. New York: Springer, 2011. 491 pp. (cit. on pp. 44, 50, 55, 73, 124, 134, 136).

[81] T. Malis, S. C. Cheng, and R. F. Egerton. “EELS log-ratio technique for specimen-thickness measurement in the TEM”. In: *Journal of Electron Microscopy Technique* 8.2 (Feb. 1988), pp. 193–200 (cit. on p. 44).

[82] R. Erni and N. D. Browning. “Valence electron energy-loss spectroscopy in monochromated scanning transmission electron microscopy”. In: *Ultramicroscopy* 104.3 (Oct. 2005), pp. 176–192 (cit. on p. 44).

[83] J. Nelayah et al. “Mapping surface plasmons on a single metallic nanoparticle”. In: *Nature Physics* 3.5 (May 2007), pp. 348–353 (cit. on p. 44).

[84] Z. Wang, J. Yin, and Y. Jiang. “EELS analysis of cation valence states and oxygen vacancies in magnetic oxides”. In: *Micron* 31.5 (2000), pp. 571–580 (cit. on p. 46).

[85] H. Tan et al. “Oxidation state and chemical shift investigation in transition metal oxides by EELS”. In: *Ultramicroscopy* 116 (May 2012), pp. 24–33 (cit. on p. 46).

[86] N. K. Menon and O. L. Krivanek. “Synthesis of Electron Energy Loss Spectra for the Quantification of Detection Limits”. In: *Microscopy and Microanalysis* 8.3 (2002), pp. 203–215 (cit. on pp. 46, 51).

[87] O. L. Krivanek et al. “High-energy-resolution monochromator for aberration-corrected scanning transmission electron microscopy/electron energy-loss spectroscopy”. In: *Philosophical Transactions of the Royal Society A: Mathematical, Physical and Engineering Sciences* 367.1903 (Sept. 28, 2009), pp. 3683–3697 (cit. on p. 46).

[88] B. Plotkin-Swing et al. “Hybrid pixel direct detector for electron energy loss spectroscopy”. In: *Ultramicroscopy* 217 (Oct. 2020), p. 113067 (cit. on pp. 47, 73).

[89] J. T. Held, H. Yun, and K. A. Mkhoyan. "Simultaneous multi-region background subtraction for core-level EEL spectra". In: *Ultramicroscopy* 210 (2020), p. 112919 (cit. on p. 47).

[90] H. Tenailleau and J. M. Martin. "A new background subtraction for low-energy EELS core edges". In: *Journal of Microscopy* 166.3 (June 1992), pp. 297–306 (cit. on pp. 49, 139).

[91] R. Egerton and M. Malac. "Improved background-fitting algorithms for ionization edges in electron energy-loss spectra". In: *Ultramicroscopy* 92.2 (2002), pp. 47–56 (cit. on p. 49).

[92] J. Verbeeck and S. Van Aert. "Model based quantification of EELS spectra". In: *Ultramicroscopy* 101.2 (2004), pp. 207–224 (cit. on p. 49).

[93] G. Bertoni and J. Verbeeck. "Accuracy and precision in model based EELS quantification". In: *Ultramicroscopy* 108.8 (2008), pp. 782–790 (cit. on p. 49).

[94] P. Cueva et al. "Data Processing for Atomic Resolution Electron Energy Loss Spectroscopy". In: *Microscopy and Microanalysis* 18.4 (2012), pp. 667–675 (cit. on p. 49).

[95] X. Weng and P. Rez. "Solid state effects on core electron cross-sections used in microanalysis". In: *Ultramicroscopy* 25.4 (Jan. 1988), pp. 345–348 (cit. on p. 50).

[96] C. O. Ingamells and J. J. Fox. "Deconvolution of energy-dispersive X-ray peaks using the poisson probability function". In: *X-Ray Spectrometry* 8.2 (Apr. 1979), pp. 79–84 (cit. on pp. 53, 140).

[97] N. Brodusch, K. Zaghib, and R. Gauvin. "Improvement of the energy resolution of energy dispersive spectrometers (EDS) using Richardson–Lucy deconvolution". In: *Ultramicroscopy* 209 (Feb. 2020), p. 112886 (cit. on pp. 53, 140).

[98] S. M. Zemyan and D. B. Williams. "Standard performance criteria for analytical electron microscopy". In: *Journal of Microscopy* 174.1 (Apr. 1994), pp. 1–14 (cit. on p. 54).

[99] Z. Horita et al. "Applicability of the differential X-ray absorption method to the determinations of foil thickness and local composition in the analytical electron microscope". In: *Philosophical Magazine A* 59.5 (May 1989), pp. 939–952 (cit. on p. 54).

[100] M. Watanabe, Z. Horita, and M. Nemoto. “Absorption correction and thickness determination using the ζ factor in quantitative X-ray microanalysis”. In: *Ultramicroscopy* 65.3 (Oct. 1996), pp. 187–198 (cit. on p. 54).

[101] P. Burdet et al. “A novel 3D absorption correction method for quantitative EDX-STEM tomography”. In: *Ultramicroscopy* 160 (Jan. 2016), pp. 118–129 (cit. on p. 54).

[102] G. Cliff and G. W. Lorimer. “The quantitative analysis of thin specimens”. In: *Journal of Microscopy* 103.2 (Mar. 1975), pp. 203–207 (cit. on p. 54).

[103] S. Z. Butler et al. “Progress, Challenges, and Opportunities in Two-Dimensional Materials Beyond Graphene”. In: *ACS Nano* 7.4 (Apr. 23, 2013), pp. 2898–2926 (cit. on p. 58).

[104] R. Grantab, V. B. Shenoy, and R. S. Ruoff. “Anomalous Strength Characteristics of Tilt Grain Boundaries in Graphene”. In: *Science* 330.6006 (Nov. 12, 2010), pp. 946–948 (cit. on p. 58).

[105] G.-H. Lee et al. “High-Strength Chemical-Vapor-Deposited Graphene and Grain Boundaries”. In: *Science* 340.6136 (May 31, 2013), pp. 1073–1076 (cit. on p. 58).

[106] H. I. Rasool et al. “Measurement of the intrinsic strength of crystalline and polycrystalline graphene”. In: *Nature Communications* 4.1 (Dec. 2013), p. 2811 (cit. on p. 58).

[107] O. V. Yazyev and S. G. Louie. “Electronic transport in polycrystalline graphene”. In: *Nature Materials* 9.10 (Oct. 2010), pp. 806–809 (cit. on p. 58).

[108] A. W. Tsen et al. “Tailoring Electrical Transport Across Grain Boundaries in Polycrystalline Graphene”. In: *Science* 336.6085 (June 1, 2012), pp. 1143–1146 (cit. on p. 58).

[109] A. Bagri et al. “Thermal transport across Twin Grain Boundaries in Polycrystalline Graphene from Nonequilibrium Molecular Dynamics Simulations”. In: *Nano Letters* 11.9 (Sept. 14, 2011), pp. 3917–3921 (cit. on p. 58).

[110] P. Yasaei et al. “Bimodal Phonon Scattering in Graphene Grain Boundaries”. In: *Nano Letters* 15.7 (July 8, 2015), pp. 4532–4540 (cit. on p. 58).

[111] Y. Cao et al. "Unconventional superconductivity in magic-angle graphene superlattices". In: *Nature* 556.7699 (Apr. 2018), pp. 43–50 (cit. on p. 58).

[112] G. Gao et al. "Artificially Stacked Atomic Layers: Toward New van der Waals Solids". In: *Nano Letters* 12.7 (July 11, 2012), pp. 3518–3525 (cit. on p. 58).

[113] J. F. R. V. Silveira, R. Besse, and J. L. F. Da Silva. "Stacking Order Effects on the Electronic and Optical Properties of Graphene/Transition Metal Dichalcogenide Van der Waals Heterostructures". In: *ACS Applied Electronic Materials* 3.4 (2021), pp. 1671–1680. eprint: https://doi.org/10.1021/acsaelm.1c00009 (cit. on p. 58).

[114] S. Wang et al. "Stacking-Engineered Heterostructures in Transition Metal Dichalcogenides". In: *Advanced Materials* 33.16 (2021), p. 2005735. eprint: https://onlinelibrary.wiley.com/doi/pdf/10.1002/adma.202005735 (cit. on p. 58).

[115] T. M. G. Mohiuddin et al. "Uniaxial strain in graphene by Raman spectroscopy: G peak splitting, Grüneisen parameters, and sample orientation". In: *Physical Review B* 79.20 (May 29, 2009), p. 205433 (cit. on p. 58).

[116] M. Huang et al. "Phonon softening and crystallographic orientation of strained graphene studied by Raman spectroscopy". In: *Proceedings of the National Academy of Sciences* 106.18 (May 5, 2009), pp. 7304–7308 (cit. on p. 58).

[117] W. Fang et al. "Rapid Identification of Stacking Orientation in Isotopically Labeled Chemical-Vapor Grown Bilayer Graphene by Raman Spectroscopy". In: *Nano Letters* 13.4 (Apr. 10, 2013), pp. 1541–1548 (cit. on p. 58).

[118] P. Solís-Fernández et al. "Determining the thickness of chemically modified graphenes by scanning probe microscopy". In: *Carbon* 48.9 (Aug. 2010), pp. 2657–2660 (cit. on p. 58).

[119] A. Luican-Mayer et al. "Localized electronic states at grain boundaries on the surface of graphene and graphite". In: *2D Materials* 3.3 (Aug. 12, 2016), p. 031005 (cit. on p. 58).

[120] J. C. Meyer et al. "The structure of suspended graphene sheets". In: *Nature* 446.7131 (Mar. 2007), pp. 60–63 (cit. on p. 58).

[121] K. Kim et al. "Grain Boundary Mapping in Polycrystalline Graphene". In: *ACS Nano* 5.3 (Mar. 22, 2011), pp. 2142–2146 (cit. on p. 58).

[122] P. Y. Huang et al. "Grains and grain boundaries in single-layer graphene atomic patchwork quilts". In: *Nature* 469.7330 (Jan. 2011), pp. 389–392 (cit. on p. 58).

[123] N. R. Wilson et al. "Graphene Oxide: Structural Analysis and Application as a Highly Transparent Support for Electron Microscopy". In: *ACS Nano* 3.9 (Sept. 22, 2009), pp. 2547–2556 (cit. on pp. 58, 87).

[124] Q. Yu et al. "Control and characterization of individual grains and grain boundaries in graphene grown by chemical vapour deposition". In: *Nature Materials* 10.6 (June 2011), pp. 443–449 (cit. on p. 58).

[125] H.-J. Kim et al. "Grains in Selectively Grown MoS_2 Thin Films". In: *Small* 13.46 (Dec. 2017), p. 1702256 (cit. on p. 58).

[126] F. Lednický et al. "Low-voltage TEM imaging of polymer blends". In: *Polymer* 41.13 (June 2000), pp. 4909–4914 (cit. on p. 58).

[127] F. Lednický, Z. Pientka, and J. Hromádková. "Ultrathin Sectioning Of Polymeric Materials For Low-voltage Transmission Electron Microscopy: Relief On Ultrathin Sections". In: *Journal of Macromolecular Science, Part B* 42.5 (Jan. 9, 2003), pp. 1039–1047 (cit. on p. 58).

[128] L. F. Drummy, J. Yang, and D. C. Martin. "Low-voltage electron microscopy of polymer and organic molecular thin films". In: *Ultramicroscopy* 99.4 (June 2004), pp. 247–256 (cit. on p. 58).

[129] N. Hondow et al. "STEM mode in the SEM: A practical tool for nanotoxicology". In: *Nanotoxicology* 5.2 (June 2011), pp. 215–227 (cit. on p. 59).

[130] O. Guise, C. Strom, and N. Preschilla. "STEM-in-SEM method for morphology analysis of polymer systems". In: *Polymer* 52.5 (Mar. 2011), pp. 1278–1285 (cit. on p. 59).

[131] B. T. Jacobson et al. "Angularly sensitive detector for transmission Kikuchi diffraction in a scanning electron microscope". In: SPIE OPTO. Ed. by M. R. Douglass, P. S. King, and B. L. Lee. San Francisco, California, United States, Mar. 10, 2015, 93760K (cit. on p. 59).

[132] C. A. García-Negrete et al. "STEM-in-SEM high resolution imaging of gold nanoparticles and bivalve tissues in bioaccumulation experiments". In: *The Analyst* 140.9 (2015), pp. 3082–3089 (cit. on p. 59).

[133] T. Ogawa et al. "Graphene-supporting films and low-voltage STEM in SEM toward imaging nanobio materials without staining: Observation of insulin amyloid fibrils". In: *Micron* 96 (May 2017), pp. 65–71 (cit. on p. 59).

[134] B. W. Caplins, J. D. Holm, and R. R. Keller. "Transmission imaging with a programmable detector in a scanning electron microscope". In: *Ultramicroscopy* 196 (Jan. 2019), pp. 40–48 (cit. on p. 59).

[135] A. Zobelli et al. "Spatial and spectral dynamics in STEM hyperspectral imaging using random scan patterns". In: *Ultramicroscopy* (Nov. 2019), p. 112912 (cit. on pp. 60, 96, 123).

[136] *Graphenea.* Graphenea. URL: https://www.graphenea.com/ (visited on 02/10/2020) (cit. on p. 62).

[137] M. Bokori-Brown et al. "Cryo-EM structure of lysenin pore elucidates membrane insertion by an aerolysin family protein". In: *Nature Communications* 7.1 (Sept. 2016), p. 11293 (cit. on p. 62).

[138] D. Chiappe et al. "Layer-controlled epitaxy of 2D semiconductors: bridging nanoscale phenomena to wafer-scale uniformity". In: *Nanotechnology* 29.42 (Oct. 19, 2018), p. 425602 (cit. on p. 62).

[139] A. Nalin Mehta et al. "Grain-Boundary-Induced Strain and Distortion in Epitaxial Bilayer MoS_2 Lattice". In: *The Journal of Physical Chemistry C* 124.11 (Mar. 19, 2020), pp. 6472–6478 (cit. on p. 62).

[140] F. Bonaccorso et al. "Production and processing of graphene and 2d crystals". In: *Materials Today* 15.12 (Dec. 2012), pp. 564–589 (cit. on p. 62).

[141] P. K. Sahoo et al. "One-pot growth of two-dimensional lateral heterostructures via sequential edge-epitaxy". In: *Nature* 553.7686 (Jan. 2018), pp. 63–67 (cit. on p. 62).

[142] T. Afaneh et al. "Laser-Assisted Chemical Modification of Monolayer Transition Metal Dichalcogenides". In: *Advanced Functional Materials* 28.37 (Sept. 2018), p. 1802949 (cit. on p. 62).

[143] D. Jannis et al. "Wide field of view crystal orientation mapping of layered materials". In: (Nov. 3, 2020). Publisher: Zenodo (cit. on p. 62).

[144] P. Ge, C. Lan, and H. Wang. "An improvement of image registration based on phase correlation". In: *Optik* 125.22 (2014), pp. 6709–6712 (cit. on p. 66).

[145] R. A. McLeod et al. "Robust image alignment for cryogenic transmission electron microscopy". In: *Journal of Structural Biology* 197.3 (2017), pp. 279–293 (cit. on p. 66).

[146] J. Lee et al. "Effect of Substrate Support on Dynamic Graphene/Metal Electrical Contacts". In: *Micromachines* 9.4 (2018) (cit. on p. 68).

[147] I. Sobel and G. Feldman. "An Isotropic 3×3 image gradient". In: (1990) (cit. on p. 70).

[148] S. Beucher and F. Meyer. "The Morphological Approach to Segmentation: The Watershed Transformation". In: E. Dougherty. *Mathematical Morphology in Image Processing*. Ed. by E. R. Dougherty. 1st ed. CRC Press, Oct. 3, 2018, pp. 433–481 (cit. on p. 70).

[149] A. Nalin Mehta et al. "Unravelling stacking order in epitaxial bilayer MX_2 using 4D-STEM with unsupervised learning". In: *Nanotechnology* 31.44 (Oct. 30, 2020), p. 445702 (cit. on p. 77).

[150] P. J. Campagnola et al. "Second-harmonic imaging microscopy of living cells". In: *Journal of Biomedical Optics* 6.3 (2001), p. 277 (cit. on p. 80).

[151] S. Psilodimitrakopoulos et al. "Ultrahigh-resolution nonlinear optical imaging of the armchair orientation in 2D transition metal dichalcogenides". In: *Light: Science & Applications* 7.5 (May 2018), pp. 18005–18005 (cit. on p. 80).

[152] S. Psilodimitrakopoulos et al. "Twist Angle mapping in layered WS_2 by Polarization-Resolved Second Harmonic Generation". In: *Scientific Reports* 9.1 (Dec. 2019), p. 14285 (cit. on p. 80).

[153] A. Säynätjoki et al. "Ultra-strong nonlinear optical processes and trigonal warping in MoS_2 layers". In: *Nature Communications* 8.1 (Dec. 2017), p. 893 (cit. on p. 81).

[154] S. Psilodimitrakopoulos et al. *Optical versus electron diffraction imaging of Twist-angle in 2D transition metal dichalcogenide bilayer superlattices.* 2021. arXiv: `2104.05783 [cond-mat.mtrl-sci]` (cit. on p. 81).

[155] R. Wade. "A brief look at imaging and contrast transfer". In: *Ultramicroscopy* 46.1 (Oct. 1992), pp. 145–156 (cit. on p. 82).

[156] J. M. Cowley and A. F. Moodie. "The scattering of electrons by atoms and crystals. I. A new theoretical approach". In: *Acta Crystallographica* 10.10 (Oct. 1, 1957), pp. 609–619 (cit. on p. 82).

[157] E. Mostaani, N. D. Drummond, and V. I. Fal'ko. "Quantum Monte Carlo Calculation of the Binding Energy of Bilayer Graphene". In: *Phys. Rev. Lett.* 115 (11 Sept. 2015), p. 115501 (cit. on p. 84).

[158] J. Ping and M. S. Fuhrer. "Layer Number and Stacking Sequence Imaging of Few-Layer Graphene by Transmission Electron Microscopy". In: *Nano Letters* 12.9 (Sept. 12, 2012), pp. 4635–4641 (cit. on p. 89).

[159] C. Ophus. “Four-Dimensional Scanning Transmission Electron Microscopy (4D-STEM): From Scanning Nanodiffraction to Ptychography and Beyond”. In: *Microscopy and Microanalysis* 25.3 (June 2019), pp. 563–582 (cit. on p. 94).

[160] T. J. Pennycook et al. “High dose efficiency atomic resolution imaging via electron ptychography”. In: *Ultramicroscopy* 196 (Jan. 2019), pp. 131–135 (cit. on p. 94).

[161] K. Müller-Caspary et al. “Atomic-scale quantification of charge densities in two-dimensional materials”. In: *Physical Review B* 98.12 (Sept. 24, 2018), p. 121408 (cit. on p. 94).

[162] G. T. Martinez et al. “Direct Imaging of Charge Redistribution due to Bonding at Atomic Resolution via Electron Ptychography”. In: *arXiv:1907.12974 [cond-mat]* (July 30, 2019). arXiv: 1907.12974 (cit. on p. 94).

[163] J. Madsen, T. J. Pennycook, and T. Susi. “ab initio description of bonding for transmission electron microscopy”. In: *Ultramicroscopy* (Mar. 2021), p. 113253 (cit. on p. 94).

[164] H. Yang, T. J. Pennycook, and P. D. Nellist. “Efficient phase contrast imaging in STEM using a pixelated detector. Part II: Optimisation of imaging conditions”. In: *Ultramicroscopy* 151 (Apr. 2015), pp. 232–239 (cit. on pp. 94, 108, 111).

[165] K. Müller-Caspary et al. “Comparison of first moment STEM with conventional differential phase contrast and the dependence on electron dose”. In: *Ultramicroscopy* 203 (Aug. 2019), pp. 95–104 (cit. on pp. 94, 111).

[166] J. Mir et al. “Characterisation of the Medipix3 detector for 60 and 80 keV electrons”. In: *Ultramicroscopy* 182 (Nov. 2017), pp. 44–53 (cit. on p. 94).

[167] H. Ryll et al. “A pnCCD-based, fast direct single electron imaging camera for TEM and STEM”. In: *Journal of Instrumentation* 11.4 (Apr. 4, 2016), P04006–P04006 (cit. on p. 94).

[168] C. M. O’Leary et al. “Phase reconstruction using fast binary 4D STEM data”. In: *Applied Physics Letters* 116.12 (Mar. 23, 2020), p. 124101 (cit. on p. 94).

[169] J. Ciston et al. “The 4D Camera: Very High Speed Electron Counting for 4D-STEM”. In: *Microscopy and Microanalysis* 25 (S2 Aug. 2019), pp. 1930–1931 (cit. on p. 95).

[170] P. Ercius et al. “The 4D Camera – An 87 kHz Frame-rate Detector for Counted 4D-STEM Experiments”. In: *Microscopy and Microanalysis* 26 (S2 Aug. 2020), pp. 1896–1897 (cit. on p. 95).

[171] P. Hatfield et al. “The LUCID-Timepix spacecraft payload and the CERN@school educational programme”. In: *Journal of Instrumentation* 13.10 (Oct. 29, 2018), pp. C10004–C10004 (cit. on p. 95).

[172] R. Beacham et al. “Medipix2/Timepix detector for time resolved Transmission Electron Microscopy”. In: *Journal of Instrumentation* 6.12 (Dec. 20, 2011), pp. C12052–C12052 (cit. on p. 95).

[173] *Advacam Advapix TPX3*. URL: https://advacam.com/camera/advapix-tpx3 (visited on 02/10/2020) (cit. on pp. 96, 123).

[174] *Attolight*. Attolight. URL: https://attolight.com/ (visited on 02/10/2020) (cit. on p. 96).

[175] D. Jannis et al. “Event driven 4D STEM acquisition with a Timepix3 detector: microsecond dwelltime and faster scans for high precision and low dose applications”. In: (July 4, 2021). Publisher: Zenodo (cit. on p. 98).

[176] A. Rosenfeld, M. Silari, and M. Campbell. “The Editorial”. In: *Radiation Measurements* 139 (Dec. 2020), p. 106483 (cit. on p. 98).

[177] R. Ballabriga, M. Campbell, and X. Llopart. “Asic developments for radiation imaging applications: The medipix and timepix family”. In: *Nuclear Instruments and Methods in Physics Research Section A: Accelerators, Spectrometers, Detectors and Associated Equipment* 878 (Jan. 2018), pp. 10–23 (cit. on p. 98).

[178] J. P. van Schayck et al. “Sub-pixel electron detection using a convolutional neural network”. In: *Ultramicroscopy* 218 (Nov. 2020), p. 113091 (cit. on pp. 101, 110–111, 149).

[179] F. F. Krause et al. “Precise measurement of the electron beam current in a TEM”. In: *Ultramicroscopy* 223 (Apr. 2021), p. 113221 (cit. on p. 102).

[180] H. Guo et al. “Electron-event representation data enable efficient cryoEM file storage with full preservation of spatial and temporal resolution”. In: *IUCrJ* 7.5 (Sept. 1, 2020), pp. 860–869 (cit. on p. 107).

[181] A. Datta et al. “A data reduction and compression description for high throughput time-resolved electron microscopy”. In: *Nature Communications* 12.1 (Dec. 2021), p. 664 (cit. on p. 107).

[182] P. M. Pelz et al. “Real-time interactive 4D-STEM phase-contrast imaging from electron event representation data”. In: *arXiv:2104.06336 [cond-mat, physics:physics]* (Apr. 13, 2021). arXiv: 2104.06336 (cit. on p. 107).

[183] A. Strauch et al. “Live Processing of Momentum-Resolved STEM Data for First Moment Imaging and Ptychography”. In: *Microscopy and Microanalysis* (2021), pp. 1–15 (cit. on p. 107).

[184] B. H. Savitzky et al. “Image registration of low signal-to-noise cryo-STEM data”. In: *Ultramicroscopy* 191 (Aug. 2018), pp. 56–65 (cit. on pp. 107, 124).

[185] T. J. Pennycook et al. “Efficient phase contrast imaging in STEM using a pixelated detector. Part 1: Experimental demonstration at atomic resolution”. In: *Ultramicroscopy* 151 (Apr. 2015), pp. 160–167 (cit. on p. 108).

[186] C. M. O’Leary et al. “Contrast transfer and noise considerations in focused-probe electron ptychography”. In: *Ultramicroscopy* 221 (Feb. 2021), p. 113189 (cit. on p. 108).

[187] S. Fujiyama et al. “Entrance and diffusion pathway of CO_2 and dimethyl ether in silicalite-1 zeolite channels as determined by single-crystal XRD structural analysis”. In: *Acta Crystallographica Section B Structural Science, Crystal Engineering and Materials* 71.1 (Feb. 1, 2015), pp. 112–118 (cit. on p. 108).

[188] R. Ishikawa et al. “High spatiotemporal-resolution imaging in the scanning transmission electron microscope”. In: *Microscopy* 69.4 (July 30, 2020), pp. 240–247 (cit. on p. 110).

[189] D. J. Chang et al. "Ptychographic atomic electron tomography: Towards three-dimensional imaging of individual light atoms in materials". In: *Physical Review B* 102.17 (Nov. 2, 2020), p. 174101 (cit. on p. 113).

[190] A. Clausen et al. *LiberTEM/LiberTEM: 0.7.0.* Version 0.7.0. June 10, 2021 (cit. on p. 113).

[191] K. van Benthem et al. "Three-dimensional imaging of individual hafnium atoms inside a semiconductor device". In: *Applied Physics Letters* 87.3 (July 18, 2005), p. 034104 (cit. on p. 113).

[192] R. Ishikawa et al. "Single atom visibility in STEM optical depth sectioning". In: *Applied Physics Letters* 109.16 (Oct. 17, 2016), p. 163102 (cit. on p. 113).

[193] H. L. Xin and D. A. Muller. "Aberration-corrected ADF-STEM depth sectioning and prospects for reliable 3D imaging in S/TEM". In: *Journal of Electron Microscopy* 58.3 (June 1, 2009), pp. 157–165 (cit. on p. 113).

[194] T. J. Pennycook et al. "3D elemental mapping with nanometer scale depth resolution via electron optical sectioning". In: *Ultramicroscopy* 174 (Mar. 2017), pp. 27–34 (cit. on p. 113).

[195] H. Yang et al. "Imaging screw dislocations at atomic resolution by aberration-corrected electron optical sectioning". In: *Nature Communications* 6.1 (Nov. 2015), p. 7266 (cit. on p. 113).

[196] P. M. Pelz et al. "Reconstructing the Scattering Matrix from Scanning Electron Diffraction Measurements Alone". In: *arXiv:2008.12768 [physics]* (Aug. 28, 2020). arXiv: 2008.12768 (cit. on p. 113).

[197] A. Velazco et al. "Reducing electron beam damage through alternative STEM scanning strategies. Part I – Experimental findings". In: *arXiv:2105.01617 [cond-mat]* (Apr. 30, 2021). arXiv: 2105.01617 (cit. on p. 114).

[198] D. Nicholls et al. “Minimising damage in high resolution scanning transmission electron microscope images of nanoscale structures and processes”. In: *Nanoscale* 12.41 (2020), pp. 21248–21254 (cit. on p. 114).

[199] X. Sang et al. “Dynamic scan control in STEM: spiral scans”. In: *Advanced Structural and Chemical Imaging* 2.1 (Dec. 2016), p. 6 (cit. on p. 114).

[200] A. Velazco et al. “Evaluation of different rectangular scan strategies for STEM imaging”. In: *Ultramicroscopy* 215 (Aug. 2020), p. 113021 (cit. on p. 114).

[201] Xavier Llopart. “Timepix4 detectors”. Dec. 2, 2020 (cit. on p. 114).

[202] J. Spiegelberg et al. “Unmixing hyperspectral data by using signal subspace sampling”. In: *Ultramicroscopy* 182 (Nov. 2017), pp. 205–211 (cit. on p. 116).

[203] M. Drescher et al. “Time-resolved atomic inner-shell spectroscopy”. In: *Nature* 419.6909 (Oct. 2002), pp. 803–807 (cit. on p. 116).

[204] C. Nicolas and C. Miron. “Lifetime broadening of core-excited and -ionized states”. In: *Journal of Electron Spectroscopy and Related Phenomena* 185.8 (Sept. 2012), pp. 267–272 (cit. on p. 116).

[205] P. Kruit, H. Shuman, and A. Somlyo. “Detection of X-rays and electron energy loss events in time coincidence”. In: *Ultramicroscopy* 13.3 (Jan. 1984), pp. 205–213 (cit. on pp. 116, 136).

[206] H. Shuman and A. Somlyo. “Electron energy loss analysis of near-trace-element concentrations of calcium”. In: *Ultramicroscopy* 21.1 (Jan. 1987), pp. 23–32 (cit. on pp. 116, 143).

[207] H. S. v. Harrach et al. “An integrated multiple silicon drift detector system for transmission electron microscopes”. In: *Journal of Physics: Conference Series* 241 (July 1, 2010), p. 012015 (cit. on p. 117).

[208] D. Jannis et al. *Spectrocopic coincidence experiment in transmission electron microscopy.* Feb. 2019 (cit. on p. 121).

[209] L. Bombelli et al. "Towards on-the-fly X-ray fluorescence mapping in the soft X-ray regime". In: *X-Ray Spectrometry* 48.5 (Sept. 2019), pp. 325–329 (cit. on p. 121).

[210] L. Ding et al. "The structural and compositional evolution of precipitates in Al-Mg-Si-Cu alloy". In: *Acta Materialia* 145 (Feb. 2018), pp. 437–450 (cit. on pp. 128, 131, 133).

[211] R. H. Brown and R. Twiss. "LXXIV. A new type of interferometer for use in radio astronomy". In: *The London, Edinburgh, and Dublin Philosophical Magazine and Journal of Science* 45.366 (1954), pp. 663–682. eprint: https://doi.org/10.1080/14786440708520475 (cit. on p. 129).

[212] N. Chandra and H. Prakash. "Anticorrelation in Two-Photon Attenuated Laser Beam". In: *Phys. Rev. A* 1 (6 June 1970), pp. 1696–1698 (cit. on p. 129).

[213] H. Paul. "Photon antibunching". In: *Rev. Mod. Phys.* 54 (4 Oct. 1982), pp. 1061–1102 (cit. on p. 129).

[214] M. O. Krause and J. H. Oliver. "Natural widths of atomic K and L levels, $K\alpha$ X-ray lines and several KLL Auger lines". In: *Journal of Physical and Chemical Reference Data* 8.2 (Apr. 1979), pp. 329–338 (cit. on p. 129).

[215] J. Kraxner et al. "Quantitative EDXS: Influence of geometry on a four detector system". In: *Ultramicroscopy* 172 (Jan. 2017), pp. 30–39 (cit. on p. 134).

[216] D. Jannis et al. "Spectroscopic coincidence experiments in transmission electron microscopy". In: *Applied Physics Letters* 114.14 (Apr. 8, 2019), p. 143101 (cit. on p. 136).

[217] F. D. L. Peña et al. *hyperspy/hyperspy: HyperSpy v1.5.2.* Version v1.5.2. Sept. 6, 2019 (cit. on p. 136).

[218] J. L. Campbell et al. "Experimental K-shell fluorescence yield of silicon". In: *Journal of Physics B: Atomic, Molecular and Optical Physics* 31.21 (Nov. 14, 1998), pp. 4765–4779 (cit. on p. 139).

[219] R. J. Graham, J. Spence, and H. Alexander. "Infrared Cathodoluminescence Studies from Dislocations in Silicon in tem, a Fourier Transform Spectrometer for CL in TEM and EELS/CL Coincidence Measurements of Lifetimes in Semiconductors". In: *MRS Proceedings* 82 (1986), p. 235 (cit. on p. 139).

[220] E. Gatti and P. Rehak. "Semiconductor drift chamber — An application of a novel charge transport scheme". In: *Nuclear Instruments and Methods in Physics Research* 225.3 (Sept. 1984), pp. 608–614 (cit. on p. 148).

[221] G. Ottaviani et al. "Hole drift velocity in silicon". In: *Physical Review B* 12.8 (Oct. 15, 1975), pp. 3318–3329 (cit. on p. 149).

[222] T. Gao et al. "Characterisation of Timepix3 with 3D sensor". In: *Journal of Instrumentation* 13.12 (Dec. 18, 2018), pp. C12021–C12021 (cit. on p. 149).

[223] A. Förster, S. Brandstetter, and C. Schulze-Briese. "Transforming X-ray detection with hybrid photon counting detectors". In: *Philosophical Transactions of the Royal Society A: Mathematical, Physical and Engineering Sciences* 377.2147 (June 17, 2019), p. 20180241 (cit. on p. 150).

List of Figures

1.1. **(a)** A schematic overview of the inner-shell ionization where the incoming electron loses energy due to the ionization of the atom. After the atom is excited, it can decay via the emission of a characteristic x-ray where the emission of the K_α x-ray is indicated. **(b)** The scattering geometry of the inelastic electron scattering where the different vectors are indicated. 14

1.2. **(a)** Schematic sketch of the MCP where the incoming electron creates an electron cloud via the interaction with the MCP. **(b)** The delay line where due where the incoming electron clouds induces an electrical pulse from which the time difference between the two pulses give information on the point of impact. . 21

1.3. A schematic overview of the hybrid pixelated detector where the three main components, detection layer, bump ball connections and ASIC are indicated. . 25

1.4. Example waveform from an energy dispersive x-ray detector (blue), note the two steps indicating the presence of two x-rays arriving. The inset figure shows the filter used to create the trapezoidal signal (red) from which the energy of the x-ray can be determined. 28

2.1. Schematic overview of the 4D STEM technique where a probe is raster scanned over the specimen, in this case graphene, and at every probe position a diffraction pattern is acquired. 33

2.2. **(a,b)** The diffraction pattern of single crystalline silicon (a) and germanium (b). The peak positions which are found by the algorithm are indicated and the arrows indicate the fitted basis vectors which will be used to determine the strain in the sample 34

2.3. **(a)** The simulated unit cell of $SrTiO_3$ **(b)**The PACBED is shown where the lower halve of the different virtual detectors are indicated. The colors of the virtual detectors correspond to the title of the reconstructed images. **(c)** The bright field image coming from the blue detector configuration. **(d)** The annular bright field image coming from the green detector configuration. **(e)** The annular dark field image coming from the orange detector configuration. Note the strong effect on the contrast depending on the detector geometry chosen. 37

2.4. The x and y-component of the first moment calculated from the 4D STEM dataset. The first moment vector $\langle\vec{k}\rangle$ is shown where on the atomic positions, the magnitude of $\langle\vec{k}\rangle$ is small since no electric field is present on the atomic positions. The integrated signal, derived from the first moment using the algorithm described in Eq. 2.11, is shown where the correspondence with the projected potential is identified. 39

2.5. **(a,b)** Two maps where the calculated phase of G is plotted for two different orientations of $\vec{k_p}$. The maps arise from the simulated $SrTiO_3$ dataset which uses the multisclice method instead of the WPOA for the simulation. The three discs, two scattered and one unscattered, are indicated on the figures where in the double overlap region, the phase $\Delta\phi(\vec{k_p})$ is given which for both regions is π out of phase. In the triple overlap, the theoretical value when using the WPOA should be zero. However since the simulations were done using the multislice method, which better approximates reality, some residual signal is seen. **(c,d)** Similar to (a,b) except the amplitude of G is shown. The non homogeneities arise from the fact that the specimen does not really fulfill the WPOA. **(e)** The reconstructed phase using the SSB algorithm. 42

2.6. The different images reconstruction which are described in this section where the total number of electrons in the dataset is indicated on the left. For low doses it is clear the the iCoM and SSB reconstruction are able to better resolve the atomic structure of the $SrTiO_3$. 45

2.7. **(a)** An EEL spectrum where oxygen, nickel and neodymium are present in the specimen. The fitted background, using the power-law method, for each edge is shown. The filled area indicates the fitting region and the line shows the extrapolation of the fit. **(b-d)** The background-subtracted spectra of the different elements where the colours correspond to the used background. . . 48

2.8. The same EEL spectrum which was shown in Fig. 2.7 where the acquisition time is varied. When the acquisition time is too low, the edges are buried in the noise and not observable. At larger acquisition time, the edge signal emerge from the noise as the SNR is increasing. 49

3.1. **(a)** Schematic drawing of the experimental setup, where the sample consists out of a monolayer graphene on top of a holey carbon support grid. **(b)** Picture of the setup, the sample mount allows camera length adjustment. 60

3.2. **(a)** Magnified VDF area of MOCVD-1L-MoS_2 film. **(b)** Line profile across the hole (vacuum) in MOCVD-1L-MoS_2. The sharp edge is used to estimate the probe size. 61

3.3. **(a,b)** Two measured diffraction patterns from a different probe position from which the translation of the central beam is apparent. Due to the large current at the central beam, no intensity is measured. **(c)** The sum signal of the scan where the small holes indicate the presence of free standing graphene. **(d,e)** The x and y-component of the first moment where the linear dependence on the probe position is clearly visible. Only the diffraction patterns, where there is both graphene and amorphous carbon, are used for the fit since due to the edges of the holes, the first moment of these diffraction patterns do not represent the shift of the diffraction pattern. 63

3.4. **(a-d)** Experimental diffraction patterns of SLG and BLG where (a) is SLG on substrate, (b) free standing SLG, (c) BLG, and (f) free standing SLG at grain boundary. **(e-h)** The background-subtracted diffraction patterns using the radial median method. **(i-l)** Annular intensity profile of the second order spots for the corresponding diffraction patterns (red). The estimated background signal from the radial median is also shown. 65

3.5. **(a,d)** The background-subtracted diffraction patterns on the substrate (a) and freestanding (d) SLG. **(b,e)** The resulting phase correlation map with the template disc where the result of the blob dog peak finding algorithm is shown. **(c,f)** The resulting peaks after filtering where the fitted basis vector is shown (blue). 67

3.6. A scan of 512 × 512 probe positions with a dwell time of ~40 ms is obtained from the SLG sample on a carbon quantifoil with a periodic set of holes. **(a)** a VDF image obtained from applying a virtually defined detector area, shown as inset.**(b)** Orientation mapping showing grain boundaries and mean orientation of each grain also in the areas where the support grid is present. **(c)** $\epsilon_{u.c.}$ unit cell expansion compared to the average unit cell across the entire FOV. ~0.5% positive strain is seen in the holes, indicating an increase of unit cell area. **(d)** VDF image of central area indicated by a white rectangle in (a), calculated based on the intensity of the brightest second order spots of the background subtracted diffraction patterns (see inset) showing a mixed contrast due to grain boundaries (lower intensity lines have the same contours from (b)), wrinkles (yellow arrow) and multiple layers (white arrows). 69

3.7. **(a)** The orientation map obtained from the same 512 × 512 scan on SLG. **(b)** The boundaries of the segmented grains using the watershed algorithm. **(c)** The fitted ellipses for every grain where the principal axes of the ellipses are shown. **(d)** Schematic view of one ellipse with the two principal axes indicated. **(e)** Histogram of aspect ratios showing that the grain shape is not spherical on average. 71

3.8. **a)** Three different diffraction patterns of SLG with different amounts of dose where only Poisson noise is added. **(b)** The average and standard deviation at different doses where for each dose 500 different realizations were made. **(c)** Zoomed in on the black rectangle shown in (b). 72

3.9. Orientation mapping of a SLG over a wide range of fields of view: from mm-scale (250× magnification) to nm-scale (9000×). **(a-d)** Orientation maps at different magnifications of the same area of the sample, showing no noticeable beam damage. (a) 50000 μm^2 FOV (300× magnification). **(b)** Zoom on the 4 squares at the top left of (a) scanned with 512x512 probe positions. **(c)** Zoom on the bottom right square of (b) using a 512x512 scan raster, corresponding to a FOV 3600 μm^2. (d) High magnification scan (9000×) with a raster of 256 × 256 probe positions over 100 μm^2, corresponding to the area indicated with a white square in panel (c). **(I-III)** Three diffraction patterns from adjacent grains identified by the same indices in panel (d). 75

3.10. **(a)** 1024 × 1024 orientation mapping of commercial SLG over ~0.168 mm^2 (250× magnification). The largest grain is indicated with a white square. **(b)** Grain size distribution calculated from the segmented dataset. **(c)** Correlation between grain size and orientation, indicating a preferential orientation for larger grains. The solid lines are the fitted results to the sum of two Gaussians and an offset. **(d)** Distribution of the number of neighbors as a function of grain size showing an increase in neighbors with increasing grain size. The solid line is a smoothed line through the data points. **(e)** Analysis of the aspect ratio of grain shape as a function of the grain size. The solid line is a skew normal fit through the data points. 76

3.11. **(a)** Orientation map of MoS_2 film, showing a single orientation (the positions of the diffraction spots remain the same across the scanned area) over a ~ 2.36 mm^2 field of view. **(b-c)** Diffraction patterns from positions indicated on (a). **(d)** The second order diffraction spot intensity mapping from scan at higher magnification (250×), where bright areas are 2 and 3L MoS_2 grains. **(e)** Orientation map (with overlapped VDF (d) for visual effect) showing that most 2 and 3L are epitaxially grown on top of the first layer. 78

3.12. **(a)** The second order diffraction spot intensity mapping from scan at higher magnification (250×), where bright areas are 2 and 3L MoS_2 grains. **(b)** The annular intensity profiles of three diffraction patterns indicated on (a). The increase in intensity indicates the presence of multiple layers. The non uniformity arises from a tilt with respect to the incoming electron probe. **(c-e)** The diffraction patterns where a clear increase is seen for the second order intensity diffraction spots. 79

3.13. Comparison of 4D STEM in SEM and P-SHG data on CVD-MoS2. **(a,d)** VDF signal and integration of P-SHG data for [0°–360°] with a 2° step. Regions of interest corresponding to two flakes are indicated. **(b, e)** Orientation map (with overlapped VDF image) based on 4D STEM data and mapping of armchair orientations over a large (2300 μm^2) sample area. **(c,f)** Histograms of two flakes orientation (colors correspond to selected areas in orientation map) from 4D STEM and P-SHG, showing a qualitative match. 81

3.14. **(a-b)** Experimental diffraction patterns from SLG and BLG (shown in Fig. 3.4(a,c)) and **(h)** comparison of annular intensity profiles of second order diffraction spots. **(c-g)** Simulated diffraction patterns of different configuration where twelve spots are present in the second order diffraction spots. The twist angle between the layers are similar to the experimental data. **(i-m)** Annular intensity profiles of SLG and two twisted SLG at 35°, SLG and AA bilayer and two AA and AB stacked bilayers respectively. 83

3.15. **(a-c)** Multislice diffraction pattern simulation of SLG, BLG with AA and AB stacking. The inset is a bar plot of I_2/I_1. For SLG and AA BLG, we get I_2/I_1=0.89, for AB stacking I_2/I_1=3.17. **(d)** Intensity of second order spots with monotonic increase with N for AA and AB stacked MLG. Both PO and multislice approximation indicate kinematical behavior until N=8. 84

3.16. **(a)** VDF signal of the scan. The virtual aperture is placed at the second order spots to increase diffraction contrast. Some increase in the signal is seen where GO is positioned. An overall demise of signal is seen at the top due to the instability of the electron gun. The distortions on the image are due to sample drift during the acquisition. **(b)** An unprocessed electron diffraction pattern originating from a GO flake. **(c)** VDF of subtracted diffraction patterns. The contrast comes from the sparse diffraction intensities. The lighter dots arise from the diffraction pattern inside holes, where the diffraction intensities are larger than on the substrate, due to additional scattering of electrons with substrate. At the top left, an overall increase is seen, indicating ML-GO. **(d)** Diffraction pattern shown in (b) after background subtraction using the method explained in *Section 3.4.2* 86

3.17. **(a)** Number of peaks detected in the second order diffraction spots, indicating the number of layers (N), if the twist-angles are resolvable. For AB and AA stacking, N cannot be retrieved from the number of peaks, since no new spots arise with respect to 1L GO. The inset shows the VDF image. **(b)** Orientation map of GO sheets, where in total three flakes are seen with two (green and red) small flakes on top of the large flake (blue). In some region, the two smaller flakes also overlap creating a 3L region. **(c)** Diffraction patterns from regions where the twist angle is visible. The twist angle in 2L is indicated on the patterns. 87

3.18. **(a-b)** Experimental diffraction patterns from SLG and 1L-GO. **(c)** Comparison of annular intensity profiles of second order diffraction spots. **(d,e; f,g)** Diffraction patterns of 2L-GO and 3L-GO, respectively, and annular intensity profiles with the same diffraction spot intensity as 1L-GO. 88

3.19. **(a,e)** Diffraction pattern of SLG and BLG, corresponding to probe positions indicated in (c). **(b,f)** BLG stacking analysis using the comparison of annular intensity profiles of the first (b) and second order (f) spots. AB stacking is identified by a 2.5 times increase in the second order intensity, while no significant change of the first order intensity is observed. **(c)** VDF signal of the area mapped, as indicated in Fig. 3.6. (uppermost white arrow). **(d,g)** Average intensity map of first and second order spots. The area where the signals increase indicates MLs. **(k)** Identification of BLG stacking by taking the ratio between second and first order VDF images where the decrease of increase indicates AB stacking. 90

4.1. **(a)** The schematic setup, where a convergent electron beam is scanned across the sample and during the scan, the point of impact and TOA is measured for each incoming electron. **(b)** The data list created by the detector where for every event the point of impact and TOA is indicated. **(c)** When the probe position at each time is accurately known, a diffraction pattern belonging to the time range for a given probe position can be obtained resulting in a full 4D STEM dataset. **(d)** Custom built retractable assembly to place the Timepix3 detector in the electron microscope column. 97

4.2. The average cluster size calculated as a function of threshold for 60 and 200 kV accelerating voltages. 98

4.3. The flat field illumination of 60 kV electrons where the threshold is varied. The relative total number of detected electrons compared to 21 keV in percentage (Σ) is indicated and also the number of dead pixels (DP) is indicated in the plots. 99

4.4. The flat field illumination of 200 kV electrons where the threshold is varied. The relative total number of detected electrons compared to 21 keV in percentage (Σ) is indicated and also the number of dead pixels (DP) is indicated in the plots. 100

4.5. **(a)** The cluster size as a function of energy threshold for the two acceleration voltages 60 and 200 kV. **(b)** The detected electron current which is calculated by dividing the number of events per second on the detector by the average cluster size. The detected current is relative compared to the detected current at a energy threshold of 7 keV. 102

4.6. **(a)** A histogram of the TOA of the incoming events with a bin size of 10 μs. **(b)** The reconstructed DF signal where the dark lines correspond to the artefacts which arise when the detector does not detect signal in some time windows. 104

4.7. **(a,e)** Single and summed multi-frame HAADF images from a $3 \times 1024 \times 1024$ scan at 6 μs dwell time. The sample is a monolayer of WS_2. The HAADF signal is collected with the conventional HAADF detector. **(b,f)** Single and multi-frame ABF images reconstructed from the simultaneously acquired 4D STEM dataset. **(c,g)** The reconstructed iCoM images from the single and multi-frame scans. **(d,h)** The reconstructed SSB images from the single and multi-frame scans. The power spectrum of each image is shown in the inset. 105

4.8. **(a,e)** Single and summed multi-frame HAADF images from a 1 μs dwell time $10 \times 1024 \times 1024$ scan of a silicalite-1 zeolite sample. **(b,f)** Single and summed multi-frame ABF images reconstructed from the use of a virtual detector. **(c,g)** The reconstructed iCoM images from the single and multi-frame scans. On the left of the image the distortions due to finite response time of the scan coils are visible. **(d,h)** The reconstructed SSB images from the single and multi-frame scans. The power spectrum of each image is shown in the inset. 106

4.9. **(a,e)** The PACBED of the 4D STEM scan where, for both signals bright field (BF) and dark field (DF), the virtual detectors are shown. **(b,f)** The BF and DF signal of a 1024 × 1024 scan at 20 μs dwell time where the sample is a low magnification image of a holey carbon film. **(c,g)** The summed BF and DF image of the same scan size with a dwell time of 100 ns and 200 frames which are scanned. Clear distortions arising from the response time of the coils are visible but the detector has no significant issues with this dwell time. **(d,h)** A single BF and DF frame of the fast scan using a dwell time of 100 ns. 109

4.10. **(a)** The reconstructed iCoM image of the raw dataset from a silicalite-1 zeolite. The scan size is 1024 × 1024, the dwell time is 6 μs, and the acceleration voltage is 200 kV. In the insets the Fourier transform of the iCoM signal is shown. **(b)** The same as (a) except declustering is applied. **(c)** The difference between (a) and (b) showing the similarity between the two signals. **e-g** The raw, declustered and difference SSB reconstruction. **(d)** a set of 500 sequential events from the same dataset detected on the Timepix3 camera, in which the declustered event is clearly seen. In the inset the PACBED pattern is shown. The power spectrum of each image is shown in the inset. **(h)** The same as (d) but now with declustering applied. 111

4.11. **(a-f)** The iCOM reconstructed signal from the 1024 × 1024 scan at 6 μs on the SI-1 zeolite using 200 kV. The total dose used to reconstruct the signal is shown in the title. **(g-l)** The reconstructed SSB signal. The power spectrum of each image is shown in the inset. 112

5.1. Sketch of the implemented coincidence detection setup using the DLD. The incoming electron creates a inner-shell excitation which decays, emitting an x-ray. The correlated x-rays and electrons are indicated with the same color. Both events (electrons and x-rays) are detected and their energy and time of occurrence are determined after processing the data stream of the TDC. 118

5.2. A small part of the data stream measured during the experiment. In this part of the data stream one x-ray is detected (channel 3) and the rest are electrons. The internal clock has a wrap around of 125 ms as shown in the data stream. . . . 120

5.3. Sketch of the implemented coincidence detection setup. The incoming electron creates a inner-shell excitation which decays, emitting an x-ray. The correlated x-rays and electrons are indicated with the same color. The electron detector used is the Timepix3. The TOA and energy of the x-rays are measured using the DANTE DPP. A synchronization signal between the detectors is send by the scan engine which also gives freedom to scan the beam over the sample to perform coincidence mapping. Python scripting was used to control the detectors and scan engine in an automated manner. 122

5.4. Schematic view on the origin of the RUP where the electrons are emitted from the gun in a Poisson process. Next, the electrons interact with the specimen creating correlated electrons and x-rays (green). Moreover, there are also non-correlated x-rays created during the interaction with the incoming electrons. The last step is the detection step where due to the non-ideal collection efficiency and finite time resolution, there is a finite probability that non-correlated processes are identified as being correlated since they occur within the time coincidence window τ. 125

5.5. Histogram of the time difference Δt between x-ray and inelastic electron showing a clear temporal correlation (red peak). Uncorrelated events are present as a background (blue). The width of the coincidence peak (inset), is assumed to be predominantly instrumental in nature. 128

5.6. **(a)**The EEL spectrum of the Al-Mg-Si-Cu alloy where the aluminium K-edge is indicated. **(b)** The x-ray spectrum where three X-rays originating from different atoms are marked. **(d-f)** The post selection of electron events, when different energy windows of x-ray energies are selected, as a function of the electron energy loss and time difference between the x-ray and electron event. The selected energy windows correspond to the characteristic x-ray energies of the different atoms (Al, Mg, Cu) present in the sample. It is clear that at a particular time difference there is a increase in signal. This increased signal corresponds to the core-level ionization event followed by x-ray emission with an energy inside the selected window. **(c)** The RUP subtracted coincidence EEL spectra for the different elements where the colour-code is identical as for figure (b). . . . 130

5.7. **(a)** Conventional EEL spectrum where the K edge of aluminium is shown from an Al-Mg-SiCu alloy. The background is subtracted using power-law fit (blue area). The background is used to determine $N_{e,e}$. **(b)** The conventional EDX spectrum where the main peak is a characteristic peak of aluminium. The background value is determined by fitting the spectrum to the sum of three Gaussians and a linear slope from which one Gaussian peak is the peak of interest. **(c)** Histogram of the number of correlated events as a function of time difference between the x-rays and electrons. The number of identified coincidence events N_C is indicated on the figure. 133

5.8. **(a)** Coincidence histograms as a function of time delay between EELS and EDX event streams for a varying beam current at constant acquisition time (y scale logarithmic). A clear improvement of correlation signal vs. background is observed for lower beam currents **(b)** The uncorrelated background signal as a function of incoming beam current (brown)). The background scales quadratically with incoming current. (green) The corrected expected background signal which would be recorded for an ideal electron detector with constant efficiency as a function of current. **(c)** The number of coincidence events as a function of incoming current scales only linearly with incoming current. The corrected signal taking the efficiency into account is shown. Note that the corrected fit better approximates a linear function.**(d)** The measured electron efficiency with a noteable decrease for higher currents due to dead time in the detector. **(e)** The SNR of the coincidence signal as a function of incoming current when using a constant acquisition time. **(f)** The SNR of the coincidence signal as a function of incoming current when the total dose has been fixed. 135

5.9. **(a)** Conventional EEL spectrum obtained from eight separate acquisitions in consecutive energy windows. The black line indicates the fitted background using a power law where the fitted area is indicated with the grey area. **(b)** The correlated EEL spectrum when using only electrons which have an Si x-ray detected within the time correlation window. In the inset figure, the x-ray spectrum is shown where the blue area indicates the energy of the x-rays selected which correspond to the x-rays from Si. The black line is the background signal obtained from using the electron outside the time coincidence window. **(c)** The coincidence and conventional background subtracted EEL spectra from which it is seen that the background subtraction method using the correlation with x-rays is able to reproduce the same result as using the conventional power-law subtraction method albeit at the expense of a lower count rate. Note that for the correlated result, no assumptions on background shape and no pre-edge fitting region was required. 137

5.10. **(a)** The EDX spectrum of GaAs where the Ga peak is fitted with a Gaussian to indicate the extent of the x-rays originating from the de-excitation of the Ga atom. The red and blue line indicates the extent of the x-ray lines in the energy spectrum. **(c)** The background-subtracted EEL spectra using the x-rays in the regions are indicated by the legend. When only using x-rays from *region 1*, it is seen that only the Ga L_{23} edge is selected without the As L_{23} edge (brown). When *regions 1+2* are selected electron from both edges are seen (green). **(c)** The same as (a) only the regions indicated out which the coincidence events are chosen have been changed. **(d)** The background-free EEL spectrum where by selecting the proper x-ray window (*region 2*), only the As L_{23} edge is selected (brown). When *region 1+2* is selected electron from both edges are seen (green). 138

5.11. **(a)** The conventional EEL spectrum from GaAs where the two edges are indicated. **(b)** The background-subtracted EDX spectra using only electrons from the two regions indicated in (a). The red spectrum only shows x-rays originating from Ga whereas the blue region shows both Ga and As since the core-loss edges have large tails. **(c)** The As L_α line can be disentangled from the Ga L_α line by normalizing the blue and red spectrum from (b) in the region where only Ga L_α x-rays are present (brown region). The difference between the normalized blue and red spectrum results in an x-ray spectrum containing only the As L_α x-rays. 140

5.12. **(a,b)** The SNR of the coincidence and conventional EELS while varying the *SBR* and *I* and keeping the exposure time constant. Note that both axes are logarithmic. The other parameters used to determine the SNR are indicated in Table 5.2. **(c)** The ratio between the SNR of coincidence and conventional EELS where a value larger than one indicates the region where coincidence outperforms conventional EELS (red colored areas). 142

5.13. **(a,b)** The SNR of the coincidence and conventional EDX while varying the *SBR* and *I* and keeping the exposure time constant. Note that both axes are logarithmic. The other parameters used to determine the SNR are indicated in Table 5.2. **(c)** The ratio between the SNR of coincidence and conventional EDX where a value larger than one indicates the region where coincidence outperforms conventional EDX (red colored areas). 144

5.14. A $300 \times 1024 \times 1024$ STEM scan at 10 μs on a diamond layer grown on top of a germanium substrate. The image shows the total number of electrons on the EELS detector at every probe position. The red window indicates the area from which the spectra are shown. 146

5.15. **(a,b)** The conventional EDX and EELS signals of red region in Fig. 5.14. **(c)** Two dimensional histogram, using a post selection on electron energy losses which are shown in (b), between time difference and x-ray energy where the electron energies chosen are the ones within the red window. **(e)** The background subtracted x-ray spectrum for the two electron energy windows indicated in (a). The black ellipse indicates the region where an excess of counts are seen compared to the blue spectrum. **(d)** Similar to (c) except that one axis is now electron energy loss and the post selection is performed on the x-ray energies shown in (a). **(f)** The background-subtracted EEL spectrum where an increase of signal is observed starting from the Ga L_{23} edge indicating the presence of core-loss events. The signal is binned in order to improve the SNR of the spectrum. Additionally, the conventional background subtracted EEL spectrum is shown where the region for the power-law fit is indicated in brown (b). . . . 147

5.16. **(a)** Zoom in on the shape of the time coincidence histogram where an asymmetric profile is seen. The dotted black line shows a Gaussian blurred saw-tooth function which would be the theoretical shape of the histogram. **(b)** The time coincidence histogram of two detectors. The sample holder is titled such that the count rate of x-rays on detector 1 is lower which is due to the shadowing of the detector. The width of the time coincidence peak is significantly lower for the shadowed detector (detector 1). 148

5.17. The SNR gain as function of mask radius for different incoming currents. The SNR gain is defined as the ratio of the SNR with the SNR when the mask radius is zero. 150

List of Tables

5.1. Areal density ratio of magnesium and copper in the aluminum alloy matrix obtained with coincidence detection and compared to conventional quantification of EDX and EELS. 132
5.2. The values for the parameters used in the calculation of comparison of SNR_C and SNR_{EELS}. 143
5.3. The values for the parameters used in the calculation of comparison of SNR_C and SNR_{EDX}. 143
5.4. The values for the parameters used in the calculation of SNR when masking the detector. 151

Dankwoord

Ongeveer vier jaren geleden begon mijn avontuur als onderzoeker. Toen ik hieraan begon kon ik de omvang en impact op mijn leven hiervan niet omvatten. Nu ik terug kan kijken op deze vier jaar kan ik concluderen dat het werk beschreven in deze thesis niet gelukt zou zijn zonder vele verschillende personen en deze zou ik graag willen bedanken!

Allereerst zou ik mijn promotor **Jo** willen bedanken om mij te kans te geven om een doctoraat na te streven in het veld van elektronen microscopie. Hij is een vat vol ideeën dat aanstekelijk werkt waardoor ikzelf veel heb opgestoken. Daarnaast was hij ook altijd bereikbaar om te helpen waar nodig.

I wish to thank the members of my doctoral committee; **Prof. Dr. Wim Wenseleer**, **Prof. Dr. Bart Partoens**, **Prof. Dr. Nick van Remortel**, **Prof. Dr. Knut Müller-Caspary**, **Prof. Dr. Jom Luiten** and **Dr. Luiz Tizei** for taking the time to carefully read my thesis. I very much enjoyed the discussions during my pre-defense, and your feedback aided in shaping my thesis into its final form. Moreover, I would like to thank **Knut** for his collaboration and his good insights into designing experiments.

Many thanks to **all** the co-workers at EMAT for their help, support and nice conversations we had throughout the years. I would like to thank **Giulio** for guiding me in my first years of my phd and always making time whenever I had any question. **Armand** for sharing his great knowledge on how to operate and understand the microscopes. **Nico** for always having a tremendous amount of unexplored unprocessed data and giving good guidance on how to treat

this data. **Andrey** for showing me the ability to find an ”easy” solution for a complex problem. **Abner** and **Vivek** who started around the same time and with whom I have worked together on a couple of fruitful projects.

Ik zou graag mijn familie willen bedanken voor hun steun en voornamelijk mijn ouders, zij hebben me alle kansen gegeven en zijn altijd supporter geweest vanop de eerste rij. Ik wil ook al mijn vrienden bedanken die tot op zekere hoogte interesse hebben getoond en daarboven op zorgden zij voor de nodige ontspanning tijdens deze vier jaren.
In het bijzonder zou ik ook **Ben S.** willen bedanken voor interesse te nemen in mijn thesis en mij te duiden op ”enkele” grammaticale fouten in dit manuscript.
Een kleine eervolle vermelding mag ook uitgaan naar mijn twee katten die tijdens de eenzamere thuiswerkende periode er altijd voor gezorgd hebben dat ik mij niet als een kluizenaar heb gevoeld.
Als laatste wil ik mijn vrouw **Meike** bedanken om haar steun en er altijd te zijn in de goed en vooral slechte, norse tijden. Na het afsluiten van dit hoofdstuk kan ik samen met haar beginnen aan ons volgende hoofdstuk waarin de ervaring die ik de voorbije vier jaar heb opgedaan minder van pas zal komen...